8-2012

Flow Field Measurements for a Cross Flow Turbine

Matthew Cameron

FLOW FIELD MEASUREMENTS FOR A CROSS FLOW TURBINE

By

Matthew Cameron

B.S. University of Maine, 2009

A THESIS

Submitted in Partial Fulfillment of the

Requirements for the Degree of

Master of Science

(in Mechanical Engineering)

The Graduate School

The University of Maine

August 2012

Advisory Committee:

Michael L. Peterson, Professor of Mechanical Engineering, Advisor

Huijie Xue, Professor of Marine Sciences

Richard Kimball, Professor, of Maine Maritime Academy

THESIS ACCEPTANCE STATEMENT

On behalf of the Graduate Committee for Matthew Cameron I affirm that this manuscript is the final and accepted the thesis. Signatures of all committee members are on file with the Graduate School at the University of Maine, 42 Stodder Hall, Orono, Maine.

Chair's Name, & Title Date

LIBRARY RIGHTS STATEMENT

In presenting this thesis in partial fulfillment of the requirements for an advanced degree at The University of Maine, I agree that the Library shall make it freely available for inspection. I further agree that permission for "fair use" copying of this thesis for scholarly purposes may be granted by the Librarian. It is understood that any copying or publication of this thesis for financial gain shall not be allowed without my written permission.

Signature:

Date:

FLOW FIELD MEASUREMENTS FOR A CROSS FLOW TURBINE

By Matthew Cameron

Thesis Advisor: Dr. Michael L. Peterson

An Abstract of the Thesis Presented
in Partial Fulfillment of the Requirements for the
Degree of Master of Science
(in Mechanical Engineering)
August 2012

Understanding the flow pattern around hydrokinetic devices is important for the development of tidal energy technology. The objective of the research is to provide the wake characteristics from laboratory measurements, including wake structure, and flow recovery in the near and far fields of a cross-flow turbine. The data can be used to assist in optimization of an array of turbines by providing experimental results for numerical models validation and industrial developers of tidal energy. Another critical use of this data will be to provide a basis for parameterization of energy extraction in coastal ocean models in resource assessment. The experimental flow field measurements presented were obtained in a tow tank. Measurements were performed with an Acoustic Doppler Velocity meter on a scale model of a cross-flow turbine. The turbine was operated near the predicted optimum efficiency with varying solidity and tip speed ratios. The shape and recovery of the wake were seen in the near field and the decay of the induced turbulence was observed to continue into the far field. This work represents a step toward the full characterization of the flow patterns induced by the cross-flow turbine with near and far field effects.

ACKNOWLEDGMENTS

This author sincerely thanks Dr. Huijie Xue and Dr. Michael L. Peterson for the opportunity to do the research as well as patients and technical leadership throughout this research. Thanks to Dr. Richard Kimball for the useful technical discussions. Thanks to the faculty of the mechanical engineering department and fellow graduate students for the many interesting discussions regarding the experimental aspects of this research. This research was supported by the Department of Energy through a research grant (DE-DD0000298) to the University of Maine.

TABLE OF CONTENTS

LIST OF TABLES

LIST OF FIGURE

1. INTRODUCTION

The present need for renewable energy has led researchers to investigate the development of wind, wave, and tidal energy sources. This international surge in demand for renewable energy resources and the subsequent investment in research have produced a wide range of hydrokinetic technology for tidal developers to consider for implementation. Two major challenges faced by the tidal industry are locating favorable sites and understanding the amount of the energy that can be extracted from the sites. Less favorable sites are more abundant, but are prone to flow instability and other issues resulting impede recovery of significant amounts of power. As a whole, developing the technology for the available sites provides engineering challenges that will determine the success of the growing industry. Fortunately, lessons learned from past developments in wind energy have resulted in a number of different turbine types, which can be explored in order to exploit an assortment of technologies of various designs and concepts.

The two main types of turbines are lift- and drag-dependent devices, respectively. An example of a drag-dependent device is a savonius turbine, which produces power by the change in fluid inertia. Lift-dependent devices include axial-flow turbines and cross-flow turbines; and the latter is the focus of this study. Lift-dependent devices produce power depending on blade shape and angle of attack to produce a pressure difference resulting in lift. Each type of turbine, and their respective power production, has different advantages. The savonius and cross-flow turbines are mechanically simple and unaffected by changes in inflow direction normal to the axis of rotation. A distinct advantage of a drag-dependent device is that its operational performance is unaffected by turbulence. In comparison, lift-dependent devices are affected by turbulence. The axial-flow out performs the cross-flow and savonius in efficiency, but has structural and mechanical disadvantages. The ability of different turbines to convert inflow velocity into mechanical energy has been shown analytically, in which the ideal turbine has efficiency of

~59%, with an ideal drag device converting ~20% of the energy (Hau, 2006). The cross-flow turbine typically performs at a efficiency that is between the axial-flow and savonius turbines; however, these numbers are for a single turbine operating in a steady and uniform flow. A single turbine in uniform flow is not how the turbine is used in practical applications. While understanding the amount of power to be extracted from a single turbine is a critical part of the engineering design, a larger question remains regarding to how much power can be produced economically from any tidal energy site.

To extract appreciable amounts of power, an array of turbines will need to be deployed at a given site. Since favorable sites are limited in number and often cover a small region, developers must consider the turbine array power density. A high-density turbine array both increases the amount of energy that can be extracted and minimizes cost by reducing the amount of underwater cabling and potentially reducing foundation costs. However, the turbine wake can cause the array power density to be lower compared to an array of turbines chosen for optimum array output. In fact, the maximization of turbine power density may be more important to the overall performance of an installation than the efficiency of a single turbine. One demonstration of the importance of this design parameter is the recent work on the cross-flow wind turbines, which suggests that higher density arrays can be used with this type of turbines **(***Dabiri J.,* 2010**)**. To address the knowledge gap in tidal power development, we have obtained and analyzed the wake data from a cross-flow turbine in a steady and uniform flow. We have focused on two flow characteristics: the mean flow recovering behind the turbine and the behavior of turbulence. This study is the first step to understand the impacts of turbines on tidal flows, which will lead to enhanced understanding of optimization of turbine array design and the potential size of this renewable energy resource.

2. OBJECTIVES

The objective of the study is to understand the flow field around a cross-flow turbine using a scaled experimental turbine and a single point three-dimensional Acoustic Doppler Velocimeter (ADV). The research explores the concept of turbine spacing by examining a single turbine's effect on a uniform flow. A cross-flow turbine belongs to a class of turbines that depends on lift to produce power. Power production depends on the inflow velocity of the fluid as well as the amount of turbulence present in the inflow. The subjects of interest are the flow recovery and the magnitude of induced turbulence as a function of distance from the turbine. To acquire the experimental results, experimental methods were developed to gather repeatable velocity measurements relative to the turbine. This method produces a composite flow fluid using multiple positions of ADV, which measures the turbine approach and departure in a quasi-two dimensional flow field. In addition to measuring the turbine's influence on the flow, operational coefficients that describe the forces are associated with the three degrees of freedom related to the turbine flow field.

The experimental method presented provides the ability to measure the recovery of the flow, particularly the collapse of the entrained region immediately behind the turbine as well as the full flow recover in the far field. For the analysis, the Reynolds time averaging concept is used as a turbulence model to classify and describe turbulent flow. From the turbulence model, other relevant variables can be computed to describe different characteristics of the wake. For example, the Reynolds averaging separates the measurement into the mean and turbulent components, from which one can calculate the quantity and the transfer of the turbulent energy through turbulent shear and turbulent kinetic energy. To further examine different attributes of the velocity measurements, a wavelet analysis was preformed providing both frequency and location information relative to the turbine.

3. EXPERIMENT SET-UPS

3.1 Tow Tank and Testing Facilities

The University of Maine tow tank (Figure 3.1) is maintained and operated by the Mechanical Engineering Department. The tank is used for a variety of projects, most of which are currently related to turbine testing. The dimensions of the tow tank are given in Table 3.1.

Figure 3.1 The University of Maine's tow

30m (Length)	2.4m (Width)	1.1m (Max Water Depth)

Table 3.1 Dimensions of the tow tank

The tow tank also has a wave making capabilities and was used in the past for research related to aquaculture. The system includes a wire pulled carriage, a wave maker, an artificial shore, and wave dampening structures. The artificial shore and wave damping structure is a valuable asset for the flow study by reducing the wave reflection allowing for long test durations and increasing the quality of both turbine and ADV data.

The carriage is the only utility available to push or pull different devices including turbines, floating and submersible structures. The wire-pull is coiled around a drive drum. The drive drum is connected to a gearbox and a motor that pulls the carriage in both directions. The carriage suspension and wheel arrangement provides a platform for hydrodynamic tests. The carriage can accelerate up to 1.5 ms^{-1}. An encoder is used to measure the position as the carriage travels down the tank. The encoder is attached to an axle, which has a rubber wheel that rides on the rail. With the recently improved suspension and a spring-loaded hinge providing downward force, the encoder wheel maintains consistent contact with the rail when the carriage travels in either direction.

3.2 Turbine

The test turbine is a cross-flow turbine in which the entire blade is parallel to the center of rotation as opposed to an axial flow turbine where blades span the radius normal to the axis of rotation. The turbine's distinctive operational characteristics of the turbine are its cylindrical shape and the direction of the inflow necessary to maintain optimal performance. The two features contribute to practical advantages in the field. The shape of the turbine facilitates a rectangular active area and better utilizes the space in the flaw channel by stacking individual turbines together. The inflow only needs to be normal to the axis of rotation, which eliminates the need to realign the turbine with the flow. Both of these characteristics reduce the turbine's overall complexity of construction and hardware.

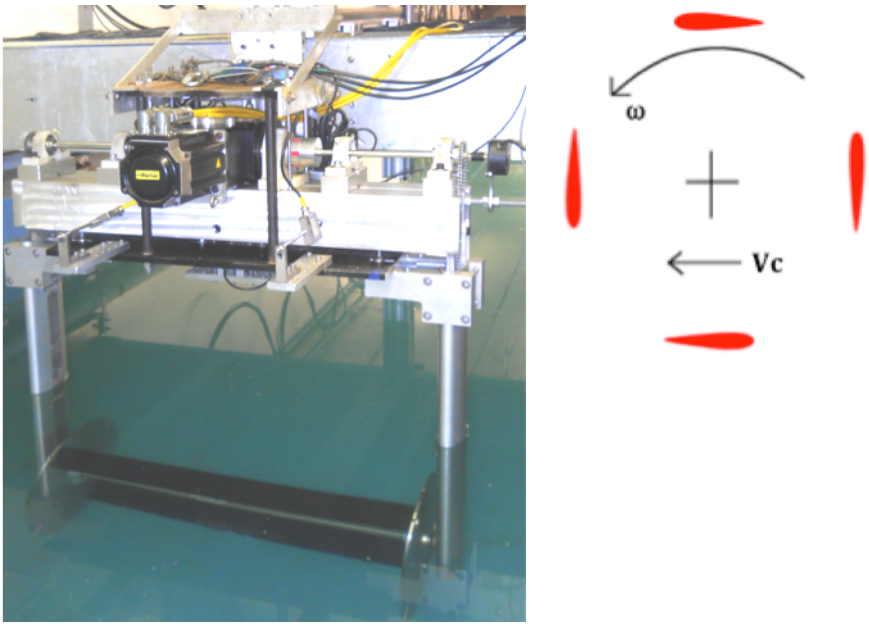

Figure 3.2 Test Turbine on carriage and side illustration of cross flow turbine

A cross-flow turbine is designed to produce maximum torque because the entire lifting surface is at the outer radius thus fully utilizing the distance between the lifting surface to the center of rotation. Figure 3.2 shows the drawing of the cross section and a picture of the test turbine in the tow tank. The torque curve can be altered by using either straight or helical blades. Straight blades produce lift and stall intermittently along the span of a blade causing the torque curve to fluctuate with position, while a section of helical blade always produces lift resulting in a steadier torque curve. Practical cross-flow turbines usually use helical blades, providing more constant torque output, as well as the ability to self-start. The blades used in this testing are straight not helical. While straight blades do not match a practical turbine, this is not a major discrepancy because the method used to measure the flow field is performed in a two-dimensional plane. The ADV sample volume measures the three-dimensional velocity within the plane depicted in Figure 3.2.

3.2.1 Non-Dimensional Variables of the Turbine

Three forces torque, drag, and heave provide the sum of all the forces acting on the turbine. The coefficients use force, fluid density, inflow velocity, and swept area to define the configuration for a turbine's mechanical characteristics. Independent of specific design factors as blade type or rotational speed. The coefficients are determined by measuring the force acting on the turbine and relating it to the available energy or power.

Performance Coefficient $$C_P = \frac{\omega T}{\frac{1}{2} \rho A V_C^3} \quad (1)$$

Drag Coefficient $$C_D = \frac{F_H}{\frac{1}{2} \rho A V_C^2} \quad (2)$$

Heave Coefficient $$C_H = \frac{F_V}{\frac{1}{2} \rho A V_C^2} \quad (3)$$

Tip Speed Ratio: Tip speed ratio (TSR) is a non-dimensional variable used to define the rotational speed of a turbine in relation to the free stream velocity. TSR strongly affects the performance of a turbine, and is the only variable easily altered once the turbine is set up.

$$\mathrm{TSR} = \frac{\omega R}{V_C} \quad (4)$$

Solidity: Solidity is a non-dimensional variable describing the ratio of blade cord length to the circumference of the turbine. A basic and useful property of the solidity is its effect on the TSR. A lower solidity turbine requires a higher TSR to maintain near-optimal performance, and conversely, a higher solidity turbine requires a lower TSR.

$$\text{Solidity} = \frac{\text{N c}}{2\,\pi\,\text{R}} \tag{5}$$

Data Set	Blade Number	Solidity
A	2	0.16
B	4	0.32

Table 3.2 List of different turbines solidity tested

Reynolds Number The magnitude of the Reynolds number influences the turbine's performance by affecting its behavior. However, the Reynolds number is complex calculations due to blades that are constantly changing their direction relative to the incoming flow. This results in a large periodic oscillation. To add to the complexity of the problem, the blade can travel back through its own wake. As the solidity number decreases, the range of angles of attack narrows and enters a region where the lift and drag characteristics are well understood, stabilizing the Reynolds number. However, a steady Reynolds number does not translate to a practical cross-flow turbine that often has a solidity and TSR chosen for high efficiency and low environmental impact. Due to the complicated blade-fluid interaction, there is no absolute value for Reynolds number. Therefore, the components; inflow and rotation as well as maximum values, are shown in Table 3.3. Other variables, such as the angle of the blades and the chord to diameter ratio, are not significant to this study, but are relevant in operation and performance of the turbine.

Data Set	Reynolds Number		
	Inflow	Rotation	Max
	$\frac{c\,V_C}{\nu}$	$\frac{\omega\,R\,c}{\nu}$	$\frac{c\,(\omega\,R + V_C)}{\nu}$
A	47,000	105,000	152,000
B	58,000	82,000	140,000

Table 3.3 Reynolds number numerical values for different effects and max for data sets

3.2.2 Turbine and Dynamometer

One purpose of the test turbine is to measure torque, vertical and horizontal forces on the turbine over a range of inflow speed, TSR, blade angle, blade shape, or blade profile. The dynamometer data is used to calculate turbine efficiency in converting inflow velocity to mechanical energy and to determine the drag and heave coefficients. The three coefficients, measuring relative magnitude of torque, drag, and heave, can be used to quantify the amount of energy removed from the fluid with respect to the amount of available energy (Hau, 2006). The forces seen by a cross-flow turbine with straight blade are uneven and dependent on blade position. The forces are measured as a function of blade position providing information on the specific response of the foils fluid interactions.

The three forces of entrance drag, heave, and torque are labeled below in Figure 3.4. The three forces are measured by load cells, located in positions on the turbine where the force of interest is isolated.

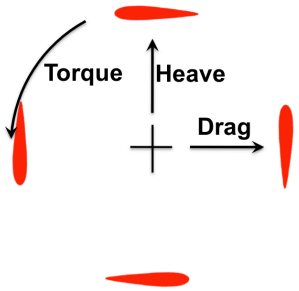

Figure 3.4 Three-dimensional forces assassinated with the turbines dynamo

The upper assembly supports the motor, drive train, and turbine. The purpose of the upper assembly is to isolate the three turbine forces through slender strut to load cells to measure only relevant forces. The motor is connected to a gearbox with dual output shafts containing a bearing that is bolted to the inner beam. A link with a load cell from the inner beam to the motor provides the motor with the resistance to rotations and provides a direct torque measurement. Due to fluctuations with the carriage's speed near the frequency range of the torque oscillation, the motor was mounted horizontally to shield the torque measurements from the carriage's oscillation. Mounting the motor horizontally exposed the load cell to the high frequency rolling noise, which was removed by a digital filtering of the data.

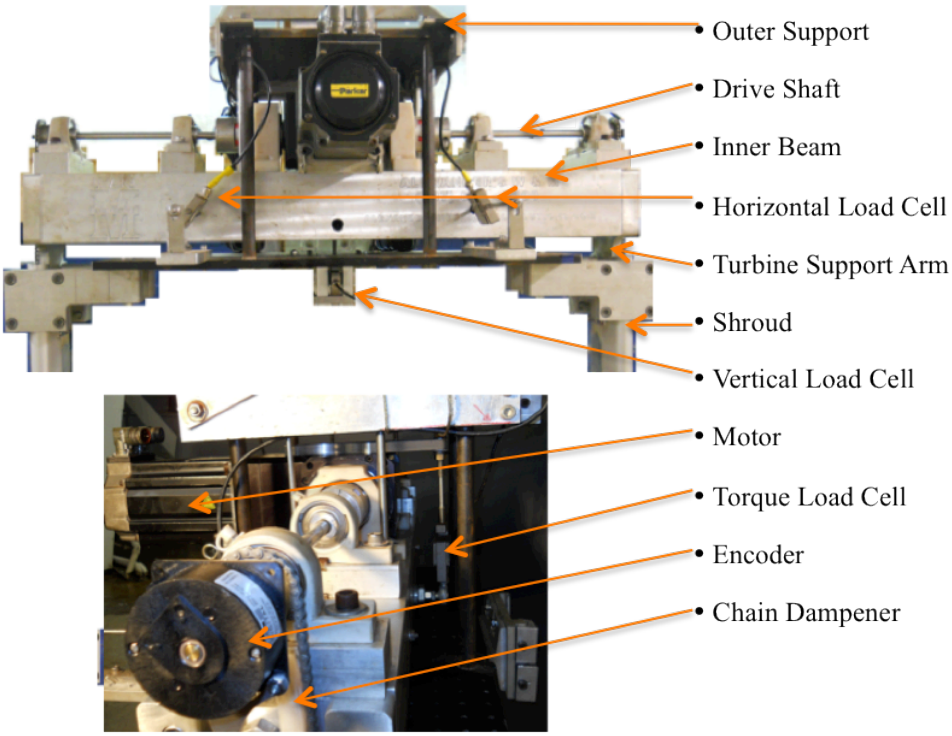

Figure 3.4 Two view of the test turbines upper assembly

The lower assembly consists of the mounting plates, the submerged portion of the drive train, and the removable blades. The turbine is supported on either side by two sleeve bearings that are bolted to the inner support arms. The inner arms are shielded from the water flow by

faired shrouds. The shrouds serve to reduce the effect of the arms on the flow field and because they are independently mounted, they prevent the drag of the arms from being included in the drag measurement. As a result, the drag measurements only measure the forces from the blades and mounting plates.

The design of the blade profile and angle of attack used for this research were selected to maximize the coefficient of performance from the test turbine based on available data. The blade shape is a NACA 63-0018, a symmetric profile developed by the National Advisory Committee for Aeronautics (Lokocz, 2010). The blade is 7.6cm in length and 76.2cm long and is constructed from carbon fiber, which produces a blade able to resist deformation under load. The rigidity of the blade and angle of attack at +5 degrees were the factors, which caused this blades' performance output to be superior to other blade types. The optimum setting does not change with different solidity ratios, thus, all tests were done using the same type of blade and angle of attack.

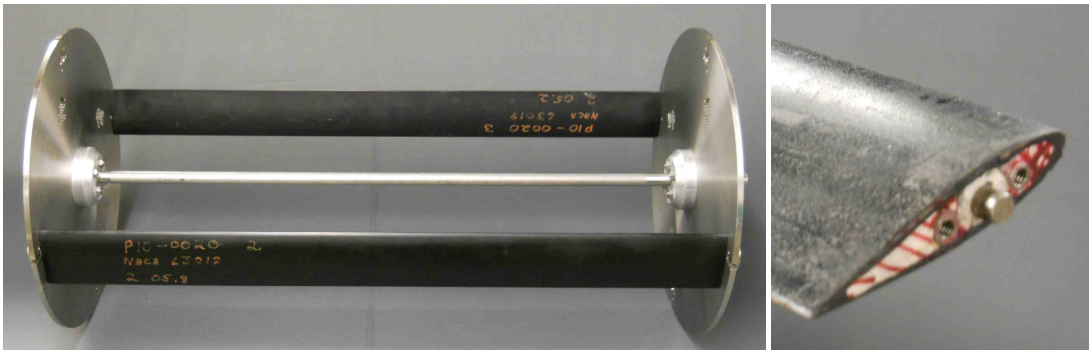

Figure 3.5 Test turbines lower assembly with two blades and NACA 63018 blade profile.

The maximum performance coefficient from the test turbine is small compared to that of the large-scale turbines used by renewable energy developers. This discrepancy in performance is due in part to the nature of scaled testing, in which the Reynolds number and drag coefficient do not scale equally. The drag on individual blades of small-scale turbines is proportionally higher than large-scale turbines, leading to reduce overall performance.

3.2.3 Confirmation of Measurements

Initial trials of the test turbine where conducted with the objective of determining the accuracy and repeatability of the measurements. Shake down testing revealed significant vibration present in the drive train that could potentially mask the torque measurement. To confirm that the measured forces reflect the forces acting on the turbine, a series of tests were performed to determine the frequency response of the drive train and support structure. The same load cells used for normal testing were used in this frequency analysis. The drive train was disconnected incrementally from the turbine blades to the motor bearings to determine each component's effect on the measured forces. The motor was run at test speeds during the test to measure the drive noise. Further trials included an impact excitation test that measured the drive train's response to a sudden impulse typical of straight blades testing. From the data gathered, the amplitude and fundamental frequency from rolling noise was determined for each component in the drive train. These results were used to dampen the largest contributors.

The largest source of noise, which was also the easiest to eliminate, was the chain connecting the upper and lower drive trains. Chain oscillations were being amplified when the motor switched from braking to driving. The noise was removed by developing an improved a chain pretension technique and adding a chain dampener. The chain dampener consists of plastic wedges to stops oscillations from propagating through the chain to the upper drive train. Upon completion of the drive train evaluation, a number of other smaller issues were identified and the effects on the drive train addressed. For example, the alignment of the blades and plates was addressed by introducing improved alignment techniques as well as refashioning the blades to tighter dimensions and improving the end connection.

The refined drive train performance improved of the results the harmonic analysis of the torque measurements as a function of motor speed. The improved consistency is shown in Figure 3.7. Results are for the entire drive train with all components used during a test connected. In

Figure 3.7, the first three harmonics dominate the torque measurement with the magnitude of the response, seen in the z-axis, within allowable limits. Identification of noise sources was aided by a linear response to motor operational speed. The linear response of the noise confirmed the result from the incremental test, which concluded that the majority of the remaining noise was from inside the motor and gearbox. The linear progressions match the output shaft rotation, shown by the red line, and the internal rotations of the motor. The motor uses a three to one gear ratio, shown by the green line. The harmonic analysis also provided information necessary for post-processing the force measurement. The most useful information acquired from the analysis was the cut-off frequency for the digital filter used to determine the force coefficients. The vibrations of the structure had a higher fundamental frequency response, than the data of interest so that a low pass filter could be used to prevent any adverse issues.

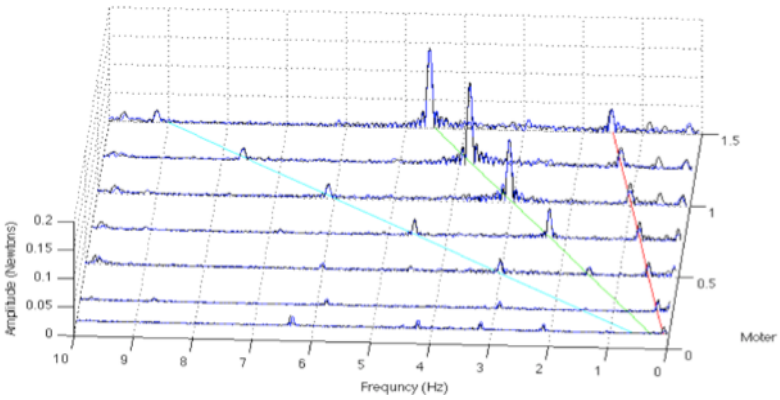

Figure 3.6 Multiple fourier transform for increasing motor rotational speed show the torque response of a freely rotating turbine.

3.2.4. Turbine Measurement

Two different turbine setups with resulting operational characteristics are shown in Table 3.4. The results are within five percent of other measurements which were primarily focused on determining the efficiency of the turbine (Debree, 2012).

(Hz

Turbine Coefficients NACA 63018, α=+5°					
	Solidity	**TSR**	**Cp**	**Ct**	**Ch**
Set A	0.16	**2.25**	**0.26 ±0.006** (Reverse & Forward)	**0.30 ±0.012** (Reverse & Forward)	**0.16 ±0.02** (Forward) **0.02 ±0.02** (Reverse)
Set B	0.32	**0.9**	**0.12 ±0.006**	**0.29±0.012**	**NA**
		1.4	**0.24 ±0.006**	**0.32±0.012**	
		1.9	**0.15 ±0.006**	**0.34±0.012**	

Table 3.4 Force coefficients form dynamo results form the two data with different solidity

The drag data showed a linear correlation with the TSR. However, the data set was insufficient to draw broad conclusions. The effects of the floor and the free surface were presumed to be the cause for the two different heave results. The carriage runs both forward and backward, while the turbine rotates the same direction, which reverses the turbine's operational orientation relative to the surface and floor. During the forward run the power side is closer to the floor, and during a reverse run the power side is closest to the surface.

The low solidity dynamometer results are shown as a function of blade position in Figure 3.8. The low solidity turbine used two blades, which resulted in each force having a period of one half of a rotation. Figure 3.8 also includes two independent tests of the same configuration to display the repeatability of the measurements. The figure shows that the drag forces are the most consistent, with the highest drag force occurring when the blades are perpendicular to the flow. The torque curve varies slightly in shape, but it integrates to approximately the power coefficient.

The shape difference between the two directions can be correlated to the standard wave patterns: the solid line is similar to the square wave, and the dotted line resembles the triangle wave. The graph shows a different shape for the heave measurements in each direction and from the table 3.4 shows the integration does not converge to one value. The differences in the torque measurement between forward and reverse runs are unexpected however, possible cause is from the change in boundary conditions with the floor and surface relative to the turbine.

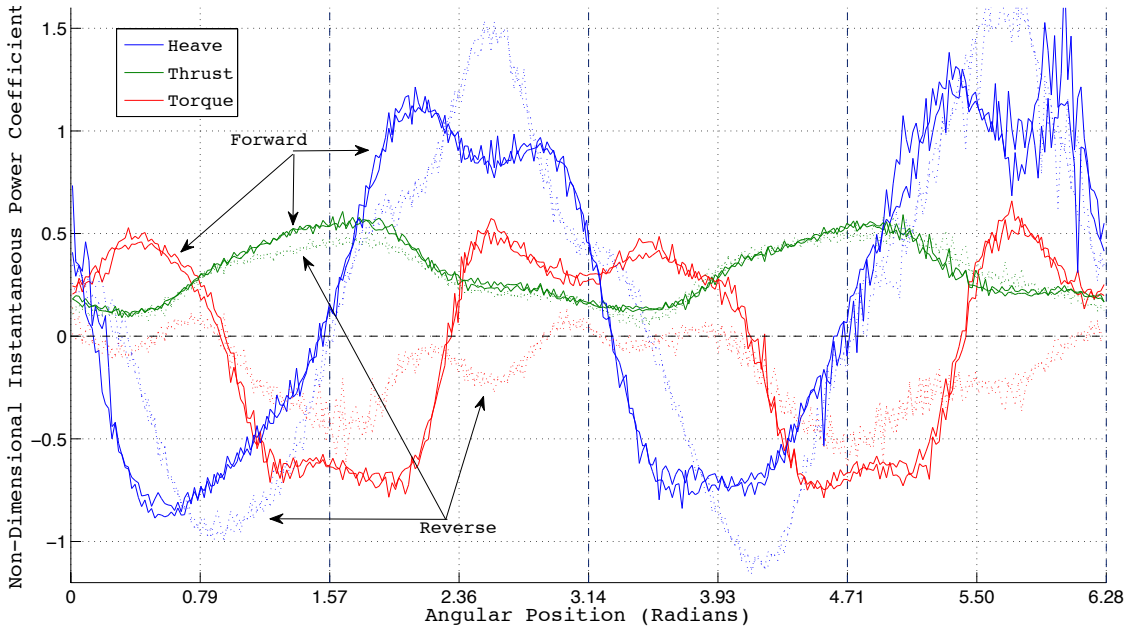

Figure 3.7 Dynamometer results as a function of blade position for low solidity with different inflow directions

The significance of the force measurement for this wake study is to show the force acting on the fluid in all test configurations. To illustrate the complexity of analyzing the wake, tests were performed over a range of inflow speeds and TSR. This behavior illustrates how the coefficients change with different inflow speeds and TSR. Variation in TSR and the effect on performance is a well-known characteristic of any hydrokinetic device, and is not within the scope of this paper. However, the turbine's method of interaction with the fluid is subject of this study. Figure 3.9 shows how the instantaneous non-dimensional form of torque and drag change with blade position and TSR. The torque demonstrates a phase shift as the TSR increases from 1

to 3 units. There are no measurements significantly distant from the optimum TSR of 2.25. The lines above the optimum performance show a growing trend in which more power is needed to maintain the rotational rate compared to low TSR. The forces do not exhibit any change in terms of the drag coefficient. All line in Figure 3.9 has a corresponding black dashed line with a height of zero along its TSR value to aid visibility.

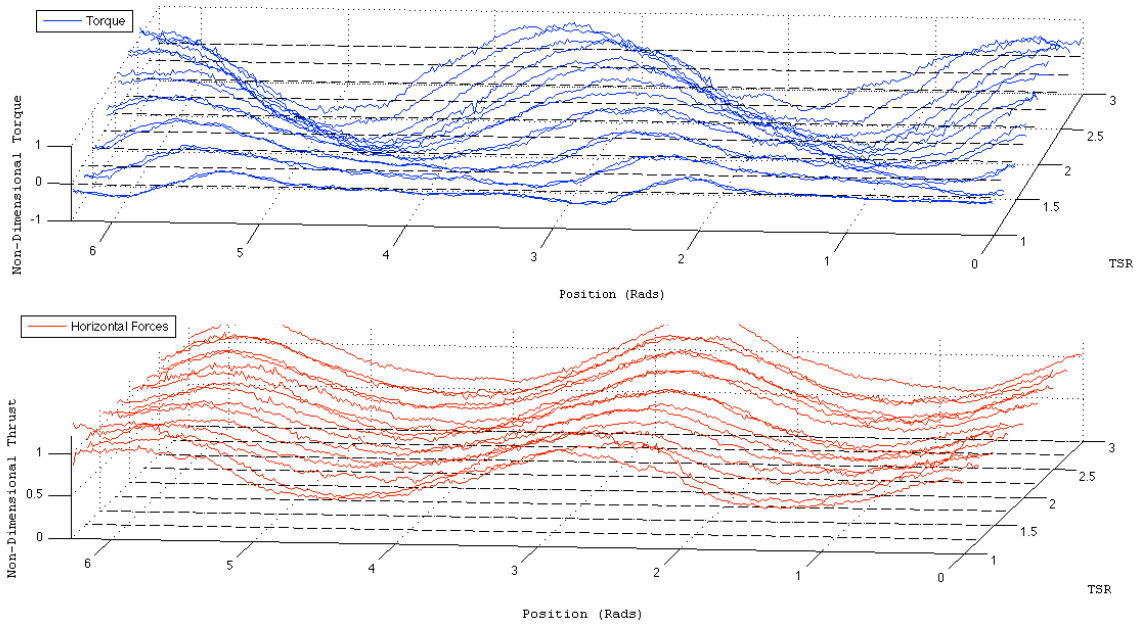

Figure 3.8 Torque and drag force coefficients as a function of blade position and tip speed ratio (TSR)

To further investigate how the turbines' interaction changes, TSR is maintained at the optimum level and the inflow speed is varied. The dependent variable from the previous test becomes the independent variable in order to evaluate these two turbine variables. The results for the varied inflow speed, seen in Figure 3.10, exhibited a different response compared to the result obtained by varying the TSR. These results show decay in the drag coefficient as the speed increased. The shape and amplitude of the curves remained constant; the only effect is on the offset. The torque curve remained constant if the maximum and minimum inflow speeds are

ignored. The blockage effect might have caused the discrepancy at the highest speed in the Figure 3.10. The blockage effect is discussed in the discussion section.

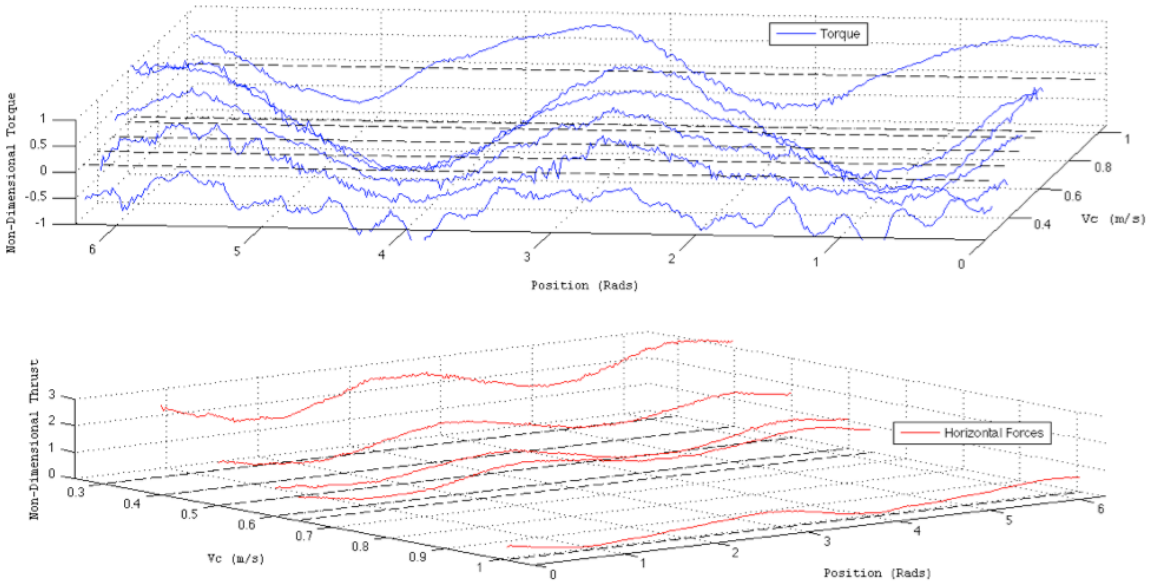

Figure 3.9 Torque and drag force coefficients as a function of blade position and inflow speed (V_C)

3.3. Acoustic Doppler Velocity meter (ADV)

The ADV used in this study is the Nortek Vector Velocity Meter (NortekUSA, Vector Field Velocimeter, Boston) (Figure 3.11). The device has been proven effective in measuring fluid velocity in a wide range of environments when deployed appropriately. The functionality and the accuracy of the device has been addressed elsewhere (Lohrmann, 1994; Rusello, 2006; Blanckaert, 2006). The ADV measures three-dimensional flow while providing minimal flow unobstructed at a reasonable high sampling rate, and are commonly used to study velocity fluctuations, turbulent shear, and other disturbances.

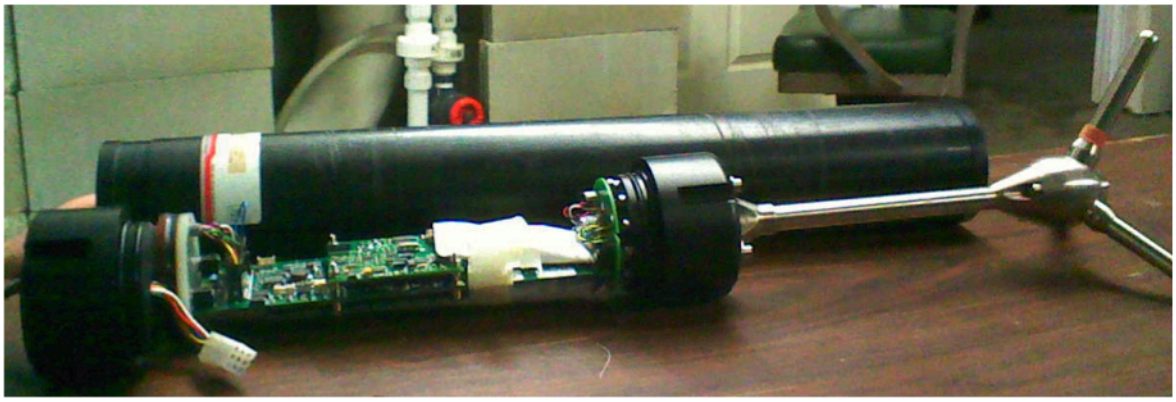

Figure 3.10 The acoustic doppler velocity meter ADV. The Nortek Vector Current Meter with its circuit board exposed.

In the field, ADVs can be operated in both salt- and freshwater environments and are typically deployed in the bottom boundary layer using a tripod or hanging from a moored buoy. This type of deployment provides a rugged structure to support the device in a harsh environment. In the lab setting, the ADV can be operated in a similar fashion, with the option of including an additional communication connection to allow for real-time monitoring and reprogramming.

The signal repletion rate for the ADV is higher then the rate at which data is stored to the memory. The ADV internal software is used to average the data and/or eliminate readings that are classified as irregular based phase-space algorithm. The velocity measurements are stored at a rate of 64 samples per second and the ping rate varies with the expected flow velocity. The ADV measures the three-dimensional velocity from acoustic Doppler shift in a region, referred to as the sample volume, ~15.7 mm in front of the ADV. The shape and size of the sample volume can be approximated by a cylinder with dimensions that can be changed with the internal setting of the ADV. Each reflection is measured by three acoustic receivers located around the sample volume (Figure 3.12). The velocity along the beam to each receiver is determined by comparing the source beam to its respective beam reflection. Using the position and orientation of the three receivers, the three-beam velocity can be converted to velocities in a Cartesian coordinate system, with the axes relative to the acoustic head (see Figure 3.12). The geometry of the three beams'

angles yields a greater resolution and range of velocity measurements in the z-direction compared to the x and y directions shown in Figure 3.12. The asymmetrical velocity resolution was considered in experimental setup to capture the higher velocity and higher fluctuations with the more sensitive direction.

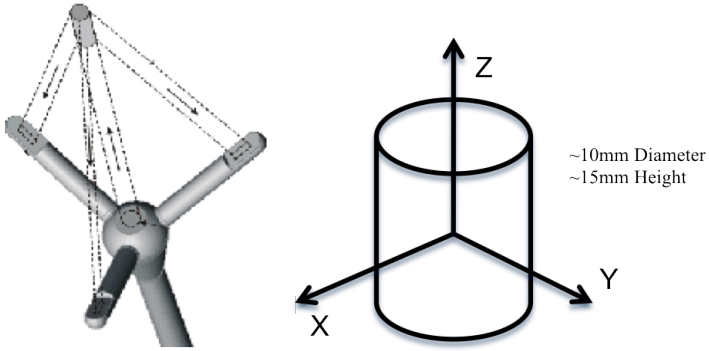

Figure 3.11 ADV's acoustic Head and sample volume with detail drawing of the acoustic head and sample volume with coordinate system

The quality of data depended on the acoustic properties of the measured fluid. For quality data, the water needs to have suspended particulates with high acoustic reflectance. The strength of the return signal is measured as the signal to noise ratio (SNR). The SNR is a non-dimensional number that compares the returning signal strength to the background noise. An arbitrary signal to noise ratio was determined through testing experience to be greater then 20.

$$\mathrm{SNR} = 20\ \mathrm{Log}\left(\frac{\mathrm{A_{Signal}}}{\mathrm{A_{Background}}}\right) \tag{6}$$

In order to obtain the required signal to noise ratio in the field lipids in plankton and other suspended matters provide the necessary reflection for acceptable signal strength. However, the tow tank water did not have a significant amount of biomass or suspended particles. To obtain high SNR, the water in the tow tank was seeded with neutrally buoyant hollow glass spheres. The spheres are provid strong acoustic reflections in the water. The addition of glass spheres enhanced the signal strength to acceptable levels. However, the SNR declined over time and had to be monitored.

The velocity data from the ADV is the average velocity of a sample volume over a period of time. The sample volume is cylindrical, 10 mm in diameter and 15 mm in height (see Figure 3.12). The height of the sample volume is related to the amount of time the receiver is active: the longer the receivers are active, the stronger the signal becomes. The ADV is very accurate in measuring creep flows with little velocity fluctuation, such as the laminar boundary layer found near river or sea bottom. On the other hand, with a change to the ADV settings, the ADV is capable of measuring velocities up to 7 m sec^{-1}. The precision of the measurements suffers in this high velocity range. The experiments in the tow tank covered a wide range of velocities and large accelerations, so an additional step was implemented in post-processing that will be discussed in section 4.1.4.

Several modifications to the ADV were needed in order to position the device in the tow tank and synchronize the ADV data acquisition with the turbine data acquisition system. The size of the ADV with the large battery bank was problematic in the tow tank. The ADV's original configuration consists of a waterproof cylindrical tube attached to an acoustic probe. The tube section is 0.55 m long and has an outside diameter of 7,5 cm. The tube cavity houses the circuit board and the large battery needed for long deployment. With the addition of the acoustic probe, the overall length of the ADV is 0.85 m. A shorter tube used to reduce the ADV's size in the tow tank. While this approach addressed the size issue, however created challenges for the communication.

There are three options for communication to the shore powered ADV. The options are 20-meter RS-422, a 6-meter RS-232 with auxiliary inputs, and a modified RS 232, which was ultimately used. The RS-422 cable uses two wires transmit the serial communication and the third powers the ADV from shore. The ability of this channel to power the ADV from shore makes it possible to remove the large battery and use the shorter tube. However, the RS-422

cable does not provide analog channels, leaving the ASCII mode as the only means for communication apart from the proprietary software. However, the ASCII mode has proven unreliable in synchronization. An alternative for communication was explored by connecting the RS-422 cable to a second computer independent of turbine and carriage system, which led to a new problem when synchronizing the ADV measurements with carriage and turbine data. The computers were synchronized to a single clock across a network connection. However, after several attempts to synchronize the ADV's internal clock with the computer it become clear it lack sufficient accuracy.

The second option was to use a 6-meter-long RS-232 cable with three auxiliary input/output analog channels, providing the means to easily synchronize multiple systems. Two major disadvantages to this method: are the RS-232 cable does not provide the option of powering from the shore, so the ADV has to use the internal battery. This causes the length of the device to be cumbersome in the confined space of the tow tank. Second, the short cable length of the RS-232 cable limits the distance between the ADV and the carriage, placing the equipment at risk during testing.

Ultimately, the RS-232 cable was selected with a modification to the ADV's internal wire harness and the function of the communication wire. The modification enabled the ADV to be powered from shore removing the battery and shortening the ADV's length. Three lines were used to carry an analog signal to the surface. This modification combines the best features, shore power and analog channels, from both options.

3.4. Pressure transducer

In addition to velocity measurements, the surface elevation was also measured to characterize the hydraulic jump caused by the turbine. The equipment used to measure elevation was a pressure transducer mounted to the ADV tripod under the ADV sample volume. The

pressure transducer must be sensitive enough to resolve millimeters of change in surface height (1 mm water height is equal to 9.8 Pa) while operating in less than 1.2 m of water (11.7 kPa). The selected hardware for this study was a pressure transducer PX409-2.5GI (Omega Engineering inc., Stamford CT.)with a full-scale pressure of 17.2 Pa and an accuracy of 0.05%, providing a resolution better than one millimeter. A flow shroud, an aluminum pipe with a series of relief holes and a sealed bottom, was utilized to prevent erroneous surface elevation measurement associated with the Bernoulli's effect. The shroud and pressure transducer can be seen in Figure 3.13 with the pressure transducer. Sequences of tests were performed to check the effectiveness of the flow shroud by exposing it to a water jet. The results revealed that the shroud was effective at nearly all angles, with the only exception when the jet was pointed into the pipe. We estimated this effect to be negligible since a strong downward jet of fluid rarely occurred near the floor of the tow tank during the tests. The pressure signal needed to reach the data acquisition system located on the moving carriage through an 8 m long wire. The wire connection to the carriage limited the carriage travel to 15m. The output from the sensor was 4-20mA to prevent noise effect.

Figure 3.12 Pressure transducer and flow shroud configuration to measure the surface elevation on the floor of the tow tank.

3.5. Test configurations

The ADV was initially fixed underneath the carriage with the acoustic head pointed downward, partially submerging the lower half. The addition of a two-dimensional traverse was added to allow the ADV to move behind the turbine during and in-between tests. The traverse

consisted of two actuators that moved the ADV horizontally and vertically. During a test, the vertical actuator would be triggered automatically and slide downward until the end of the test. This configuration allowed the measurements of velocity profiles in the wake at short distances behind the turbine. Figure 3.15 shows a data sample with three-dimensional velocities from six traverses at different horizontal distances from the turbine. The vertical velocity is represented by the color of the dot located at the ADV's point of origin, which represent velocity magnitude. Due to the space limitation underneath the carriage and the length of the ADV, the bottom half of the wake could not be measured. The data shows a section behind the turbine where a large mass of water was entrained vertically through the water column.

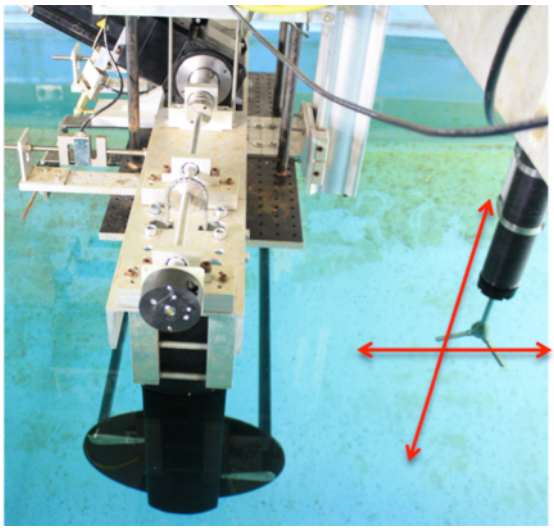

Figure 3.13 ADV's carriage mount setup with two degrees of freedom. ADV was capable of moving in two dimensions in a plane normal to the turbine axis of rotation.

Carriage vibrations, coupled with the flexibility of the ADV mount, which led to uncertainties in the velocity data. Accelerometers were attached to the carriage to address determined the severity of the vibration. The accelerometer results were processed by a discreet Fourier transforms to convert the acceleration measurements to the frequency demand. The strongest amplitudes were in the measured in the vertical direction with the dominant frequencies between 1.5 to 2 kHz. The acceleration results where high enough to potentially contaminate ADV recordings, therefore, this mounting method was abandoned.

One alternative to mounting the ADV to the carriage is an overpass method, in which the ADV is mounted on a tripod and placed on the floor of the tow tank (Figure 3.15). Having the ADV stationary on the concrete floor alleviated the problem of data contamination by carriage vibration. As mentioned above in Section 3.3.1, the velocity component in the direction emanating from the acoustic source to the sample volume (z-axis in Figure 3.12) is more robust and reliable. Given this characteristic, the ADV was placed in the x-z plane, pointing the direction down the length of the tank (x-axis in Figure 3.16). The ADV also created the smallest flow obstruction in this configuration. Due to the confined space of the tow tank, the ADV had to be mounted at an angle from the floor to clear the turbine overpass. The angle of the ADV in the stand could be changed to vary the distance between the ADV's sample volume and the center of the turbine. The pressure transducer was mounted on the same stand as the ADV, and was situated underneath the acoustic sample volume Figure 3.13. Given the sample volume location relative to the ADV acoustic head, it was possible to measure the velocity a few centimeters into the turbine-swept area. This configuration became the favored method for this study because it also measured the entire wake at a constant height, as well as the flow field as the turbines approached the ADV. A full outline of the deployment procedure is given in Appendix A.

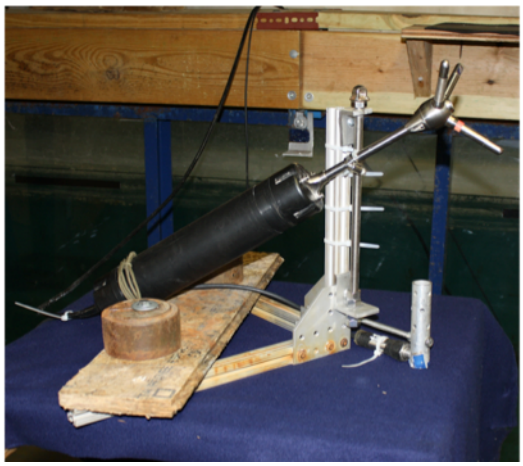

Figure 3.14 ADV and pressure transducer with flow shroud mounted to the adjustable floor tripod.

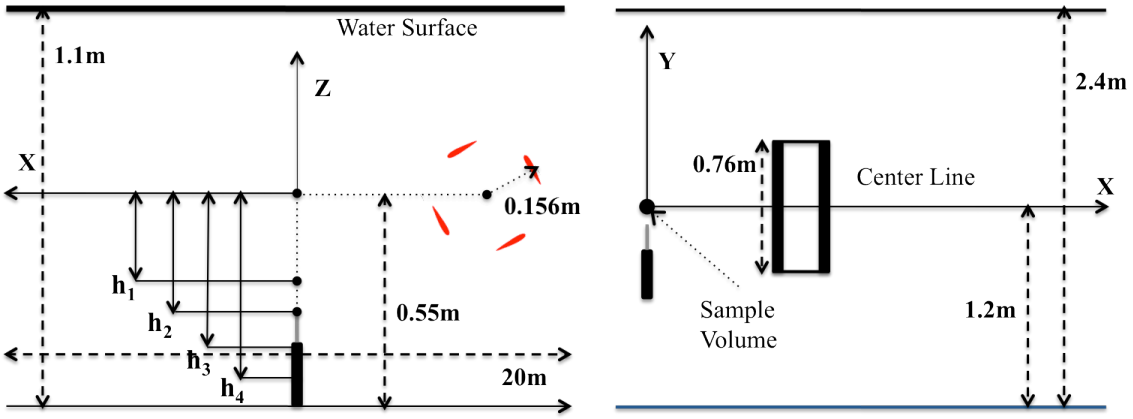

Figure 3.15 Illustration of side and top view of experimental configuration. Two view drawing of experimental setup . X-Y Plane (Left) and X-Z plane (Right).

The mounting fixture used in the overpass configuration was a weighted tripod. The function of this tripod was to provide a rigid stand for the ADV and to provide the ability to change the ADV angle easily while the ADV was on the bottom of the tank (Figure 3.13). Being able to change the sample volume height without needing to remove the entire apparatus simplified the calculation of the relative position of the ADV to the turbine during data processing. The series of vertical positions of the sample volume were measured outside of the tank and were cataloged for post-processing. Changing the height enabled the construction of flow field in a two-dimensional x-z plane. The three-dimensional velocities were measured with the ADB converted from the reference coordinate of the sample volume (see Figure 3.12) to the reference coordinate chosen for the tow tank (see Figure 3.16) later in post possessing. The archive data included three or four different heights. These heights, coupled with the ability to run the carriage backward, made it possible to create a data set both above and below the centerline of the turbine. The final data arrangement, seen in Figure 3.17, shows the two different carriage directions combined to produce the upper and lower portion of the wake. Note that the composite image may distort the actual characteristics of the upper portion of the wake because of the different condition for a free surface and the floor. This will be discussed further in subsequent chapters.

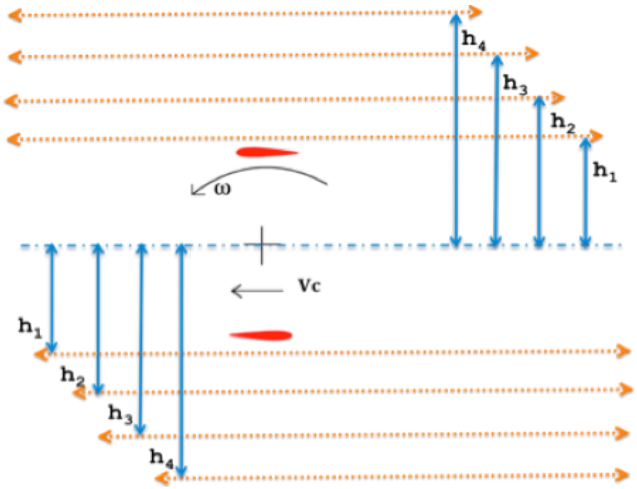

Figure 3.16 Approximation of flow field drawing of different ADV sample volume height with respect to turbine

A large number of tests were necessary in order to obtain meaningful results. We considered a number of variables, including ADV velocity range, the carriage direction, the sample volume height, the horizontal distance from the turbine center to the sample volume, and the blade position over the sample volume. All of the variables except the blade position were easily controlled and monitored. The objective of the repeatable blade position was to have the turbine blade positioned at a particular angle (±5 degrees) when the turbine passed over the ADV sample volume. Three methods were attempted, with different degrees of success. The first method returned the blade to its original angular position before the turbine and carriage were accelerated to their test speeds. This method yielded a repeatability of 20 to 40 degrees and was not significantly better than a random blade position test performed without constraining the initial angular position. The next iteration used a feedback control loop in addition to the initial controlled blade. The control algorithm monitored the distance traveled by the blades and turbine and provided feedback to the motor control array. This second method did not produce any significant improvements in blade angle repeatability. The limit to the feedback control was diagnosed from process programming: the time when the carriage and turbine were accelerating was a period of high speed and was the major cause of variation in the repeatability. To mitigate

variation, a feedback controller was utilized to develop the final experimental design. The turbine remains at rest until the carriage traveled a certain distance from the starting point. This final method resulted in a repeatability of ±3.5 degrees.

3.6. Programmable Controller and Data Acquisition

A programmable real-time controller was used to control, record, and integrate the carriage, turbine, and ADV operation and data collection. The hardware consisted of a controller (NI cRIO 9073) from National Instruments (Austin Texas) that was connected to its host computer, which ran the NI LabView software. The cRIO was an independent controller with one processing unit and memory designed to run input and output (I/O) utilities. For simplicity and reliability, all I/O signals connected to the cRIO were analog. The digital encoder used was connected to analog converters then to cRIO.

Programs for the cRIO and host computer, and the architecture of the hardware were designed to meet three specific criteria: high sampling rate, continuous test time, and the ability to update graphical output in real time. These criteria were met by splitting the tasks between the host computer and cRIO through a shared memory network, which allowed data to be steamed without interruption and at high throughput. The cRIO was programmed to run the I/O utilities by updating the outputs while writing the inputs to the shared memory. The host computer updated the graphics for users and removed data from the shared memory to stay within memory limits. While the test was running, the host computer wrote the data to a binary file on the host hard-drive and converted the binary file to a text-file once the test ended. The cRIO memory size was a limiting feature of the device with 250 KB overall and 20 KB free space after programs and drivers were installed. With the limited memory, and a high sampling rate, long test times, and ten input channels, the cRIO was not capable of independently handling data storage alone.

The host computer was monitored by an operator, who input test parameters. The host computer generated the acceleration curves to be used by the cRIO during the ramp-up and ramp-down stage. The acceleration curves were sent to the cRIO, which supplied the turbine and carriage output channels with an analog signal to a variable frequency drive. Once a test was initiated, the cRIO began to record data from six channels from carriage-turbine system, and four channels from the ADV. The primary objective at this stage was to accelerate the turbine and carriage to the target speed. During the acceleration stage, the cRIO was run at a lower rate to reduce the size of the control curves. In the ramp down stage of testing, the data acquisition was stopped, and the same curve from the acceleration was used but read in the opposite direction.

The acceleration stage was followed by the constant speed test period where data aqusition was perform at high sample rate. The sample rate for the cRIO was raised to 2 kHz during this period, and since the ADV had a significantly lower rate of 64Hz a second independent data stream was added for the ADV. The high sample rate for the pressure transducer, turbine, and carriage became unnecessary once the shakedown tests were finished and the system dynamics were well understood. The two streams of data were sent to their independent memory buffers. To avoid both computers accessing the same memory at the same time, the cRIO signaled the host computer when to clear the memory. The host removed the data and sent it to a binary file, and updated the user screen for a near real time display for the operator to watch and confirm the data quality. Figure 3.18 shows the bidirectional flow of data from the carriage computer to the three systems.

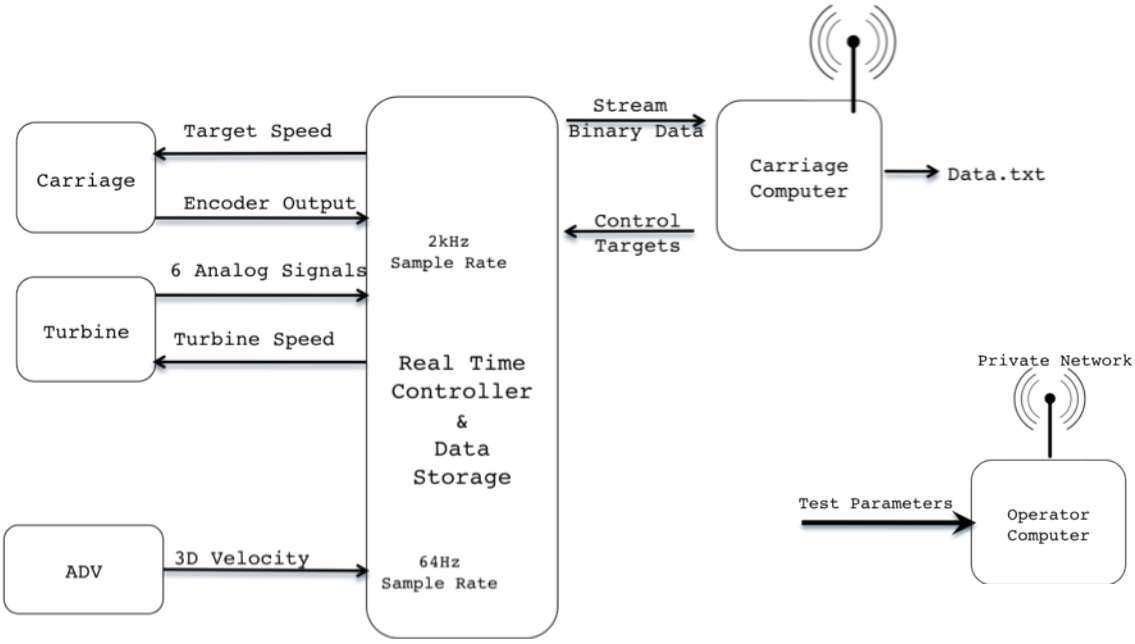

Figure 3.17 Flow diagram of controller and data acquisition. Flow chart of operator inputs and I/O data through the automation system

3.7. Synchronization

Multiple methods were tried to synchronize the systems, which resulted in a final method that is simple, reliable and accurate but requires a large amount of post processing. The final method linked the systems together by connecting carriage computer to the ADV located on the floor of the tow tank. A tether carried the command from the operator as well as data communications to the DAQ. The DAQ recorded both the turbine and ADV data in different files and were synched by a shared time array. However, by comparing both internal and analog data the analog signals did not match the internal files thus the analog signal was only used to synchronize the internal ADV data to the DAQ's clock.

Post processing of the signals used Matlab (Math Works 2009b) to handle the data unpacking, sorting, and data saving from the two Labview files and ADV internal file. The first step in the process is to unpack the data, performs basic conversions of the analog signals to physical units, and performs filtering on the load cell data. In the first synchronization step, the two velocity files were plotted next to each other and a corresponding point was identified in both

files. At this point, the process of matching the Labview and ADV internal files has not been done with automation. Each file was identified at an indicial point using the MATLAB's graphical tool and combined to form a synchronize date. This data is then synched with the turbine to identical data stored in the ADV internal memory. Each file was thus marked with a data stamp that corresponded to the data mark. Once all the files were marked, the second m-file was used to repack all the ADV internal files and associate each ADV with the corresponding turbine file.

With the turbine and ADV files linked, the instantaneous position of the blade can be calculated from three degrees of freedom with respect to ADV's sample volume. The three degrees of freedom consist of the vertical position of the ADV, the horizontal position of the carriage, and the angular position of the turbine (see Figure 3.19).

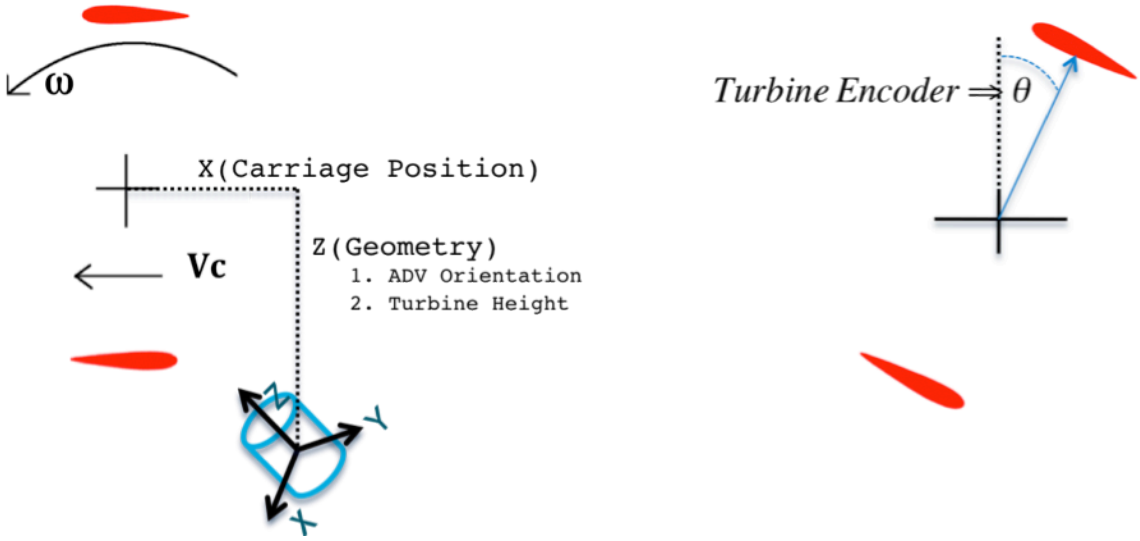

Figure 3.18 The three variables needed to determine position of the sample volume relative to each blade.

In order to determine and incorporate the relative position of the ADV into the synchronization of the data, a constant starting position for the carriage was used. For each carriage direction, a separate calibration run was conducted. Unlike normal runs, the system was controlled manually during the calibration run and the turbine was fixed at a predetermined

angular position. The carriage was moved until the lower blade intersected with the sample volume, causing a drop in the ADV's signal-to-noise ratio. At the point of intersection, the carriage was stopped and the carriage encoder data was integrated to find the horizontal distance from the starting point to the ADV sample volume. The angular position of the turbine was held constant at a predetermined angle, allowing the leading edge of the blade, located at the center, to maintain the measured distance from the sample volume to the turbine center.

To find the relative vertical distance from the sample volume to the turbine center two measurements were taken. The vertical position of the sample volume was measured outside the tank, while the vertical position of the turbine centerline was measured in the tank, and the difference was the relative vertical distance. The measured valued were logged and retrieved later during data processing.

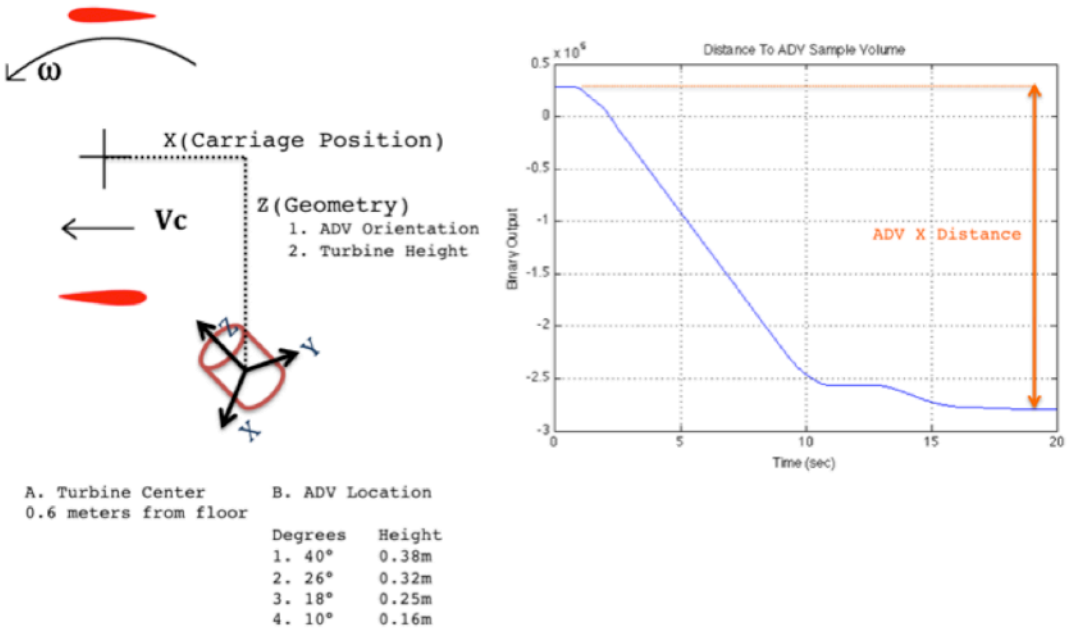

Figure 3.19 Calibration data used to measure position of turbine relative to the ADV sample volume.

The angular position of the blade was recorded by the cRIO and then converted to radians. The value was then used to calculate its instantaneous position in the chosen reference frame. The position of each blade was converted in to x and z components, with the center of the turbine

at the origin. The addition of the carriage position to the x-component yielded the relative position of each blade to the sample volume. As seen in Figure 3.21 below, the two-blade path was represented with two lines as it passed the sample volume located at zero distance.

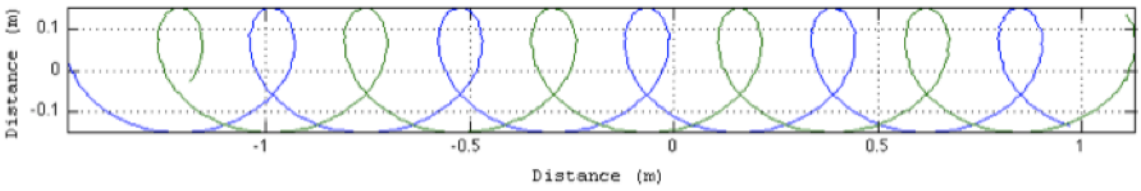

Figure 3.20 Tracking Blades with respect to ADV'S sample volume. Path of two-blade over the ADV's sample volume where x-axis represents the blade's horizontal distance to the ADV sample volume and the y-axis distance relative to the center of turbine

The blade path was repeatable over many tests, maintaining an accuracy of ±3.5 degrees over the sample volume. The method used to calculate the blade path is described in Section 3.3.2. The blade path is not relevant in the analysis; only the instantaneous position of the blades over the sample volume is needed.

4. DATA ACQUISITION AND POST PROCESSING

4.1 Analog I/O

To develop a means of tracking the individual blades during a test the measurements of the angular position of the turbine and movement of the carriage along the track were required. An absolute encoder was installed on the upper assembly and attached to one of the two drive shafts located on the upper assembly. The upper-drive train was geared one-to-one with the turbine. As a result, one rotation of the absolute encoder corresponds to one rotation of the turbine. The signal from the absolute encoder is a linear signal from zero to five volts, which corresponds to a position between 0 to 2π radians. Hence, the encoder curve consisted of a saw-tooth signal (Figure 4.1), and only a calibration constant was required to convert analog signal to the angular position.

To standardize the blade position for all tests a procedure of alignment the turbine encoder to a blade position was established. The turbine and encoder were placed at the zero position by manually rotating the turbine until one blade was located at the top dead center. Then, the encoder was spun until its output was reading zero volts, putting the blades and encoder at a known position. With the turbine and encoder synced this way, the blade location could be determined at any time during a test.

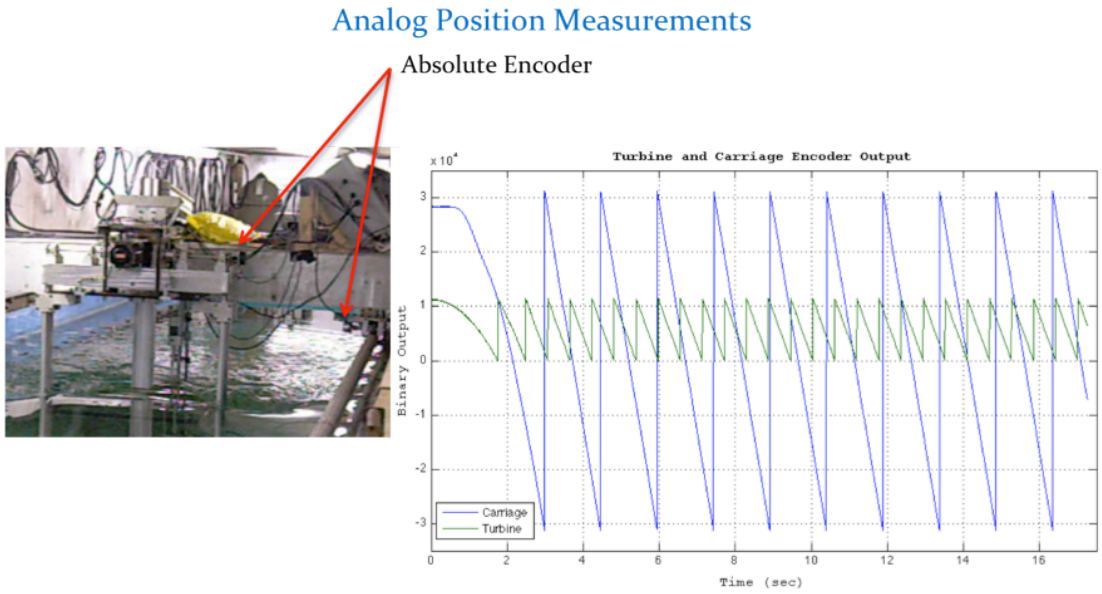

Figure 4.1 Encoder curves from turbine and carriage from a test starting at rest.

The method used to measure the carriage position was similar, to the blade posision measurements. However, the method needed to be refined due to the distance and the required accuracy of tracking the carriage position within millimeters. Unlike the turbine encoder, which measures the position directly, it was impractical to measure the carriage position directly because of the long distance traveled. A series of solution were implemented by using a digital encoder augmented with a digital-to-analog converter. The convertor maintained a data acquisition system that used only analog signals as well as providing a reliable and adaptable signal to best fit the experiment objectives. The result from the encoder and converter was an analog signal of a saw-tooth wave similar to a rotary potentiometer. The saw-tooth wave ranged from -10 to 10 volts (Figure 4.1), with one tooth equal to 8.3 revolutions of the carriage encoder. This broadens signal range made it possible to obtain the carriage position measurements accurate to within ±2 mm.

A numerical processing procedure was needed to convert the saw-tooth signal into a curve that represents the actual carriage position with respect to time. The saw-tooth signal had

discontinuities where the value jumped from 10 to -10, which needed to be removed to reconstruct the actual position. To find the discontinuity the derivative of the signal was evaluated. If an exceptionally large change or sudden change of sign occurred, the derivative was replaced with the mean value. The new continuous signal was then passed through a zero phase shift digital filter with a cutoff frequency of 40Hz to remove any electrical noise. The steps of converting the encoder data to the carriage position are shown in Figure 4.2. The filter did not affect the carriage position measurements since its velocity oscillations are was much lower, ranging from 0.1 to 20 Hz. At this stage, the filtered data had the unit of volts per unit time.

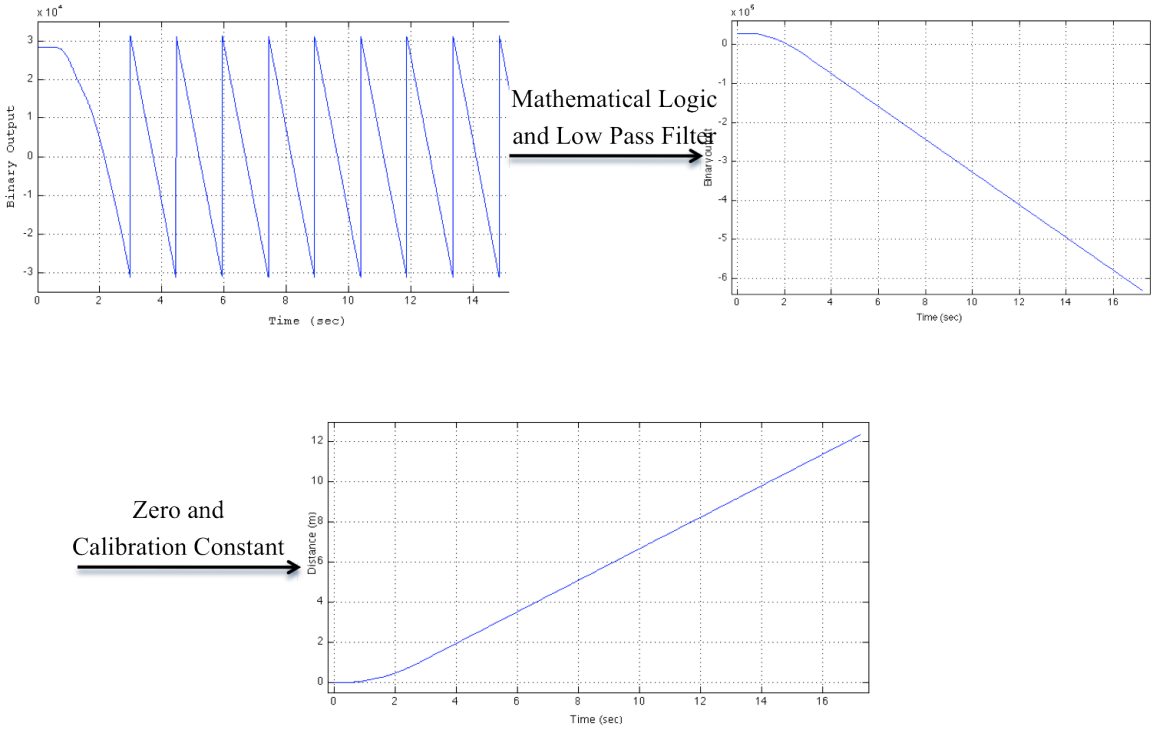

Figure 4.2 Steps for processing the carriage encoder signal. Raw data (upper left), steps removed (upper right), and final instantaneous position curve (bottom).

The filtered derivative term from the position was used to reconstruct the carriage velocity. The carriage and turbine speeds are shown in Figure 4.4. The calculated carriage speed was not directly used in the wake analysis, but it provided to better understanding of the system speed control. For example, certain combinations of carriage and turbine speeds for a low solidity turbine would produce an unstable speeds for both the turbine and carriage. The fluctuations

could reach as much as 20% of the target speeds. Fortunately, the unstable oscillation became more prevalent far from the peak performance and was thus of little immediate interests.

4.2 ADV measurements

The ADV data were saved in two ways. The simplest and most reliable method to obtain acceptable velocity was to save the data internally to the ADV. However, the internal data was not synchronized with other systems, leaving the ADV data isolated from with the turbine and carriage data. The ADV memory files consisted of 12 columns of data, four of which were relevant including the signal to noise ratio (SNR) and three velocity columns. The ADV internal timer was not accurate enough to be useful in synchronization. To overcome this synchronization problem, a second data stream was sent from the ADV to the cRIO via the three analog channels contained in the RS-232 communication cable. The analog output contained the same data, which was not only saved internally in the ADV but also saved synchronously with the turbine and carriage data. To maintain high quality velocity measurement the SNR and the velocities were checked before saving. With the system synchronized, it was then possible to determine the turbine and blade positions relative to the ADV.

The raw data taken from a given experiment consists of three files: two files from the LabView program (the analog output of the turbine and ADV), and one from the ADV internal memory. The ADV internal memory was downloaded later, after subsets of test were completed. The LabView files pertaining to individual experiments contained only approximately 10 seconds of data. In contrast, the ADV's internal memory was used repeatedly over many experiments and became large, often containing 30 to 60 minutes worth of data. Figure 4.4. shows a segment of the raw velocity data from the ADV internal memory.

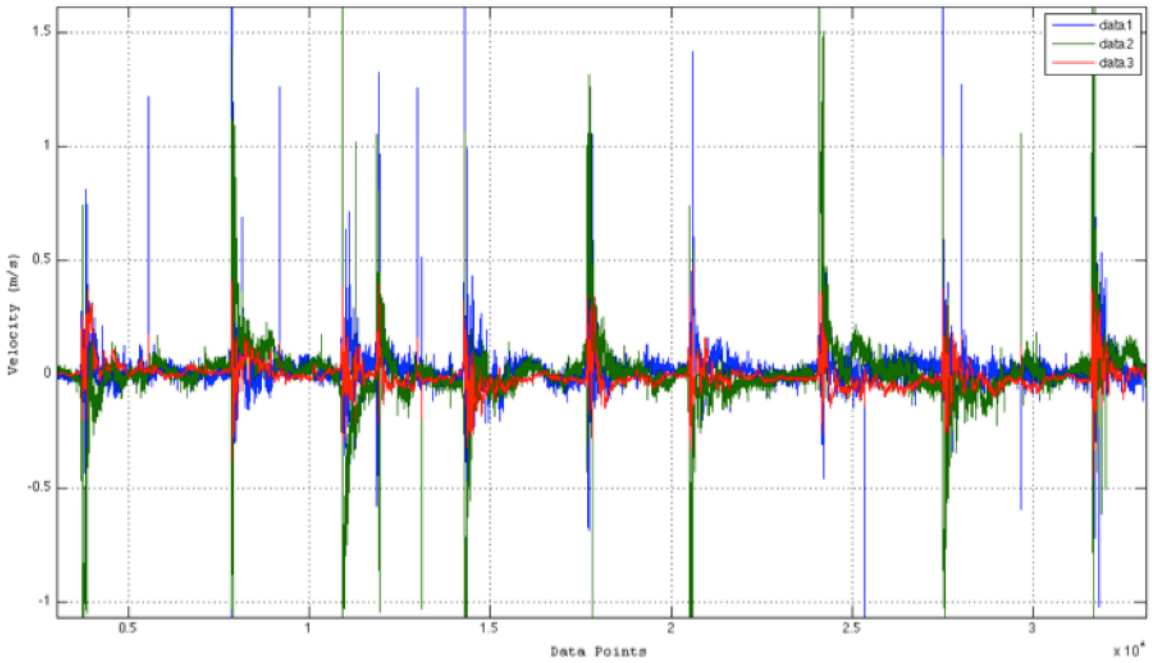

Figure 4.3 The raw three-dimensional velocity data from the ADV's internal memory

Tests were done in increments, such as a single ADV height or a single velocity range. Once a single ADV height and velocity range was complete, the data was downloaded and checked for any unobserved problem as a precaution. LabView and ADV internal files were both accounted for and checked for quality and missing data before moving forward to the next subset of data. The velocity measurements were checked to confirm that the velocity range and the SNR were acceptable. The two velocity files, one from the ADV internal files and one from LabView, were then compared to each other. It was found that the analog output of the ADV did not always match the data in the internal memory of the ADV. The ADV files from LabView were determined to be less precise than the ADV internal files, and were therefore not used for the final analysis. Consequently, the LabView ADV files were only used as a reference to synchronize the timing from the ADV internal memory files with the turbine data.

To validate velocity measurements from the ADV and the carriage encoder, a series of tests were performed in order to compare the two devices to an independent estimate, based on the time required for the carriage to travel a known distance. To perform this test, the ADV was

mounted to the carriage to measure the undisturbed flow and a 15-m section of rail was measured and marked. The tests series were done over a range of speeds. Figure 4.5 shows an example of the result that captures the carriage's initial speed oscillations as it gradually approached the target speed of 0.8 m s^{-1}. The clock time began only after the carriage reached a stable speed so the acceleration and oscillation period was not included in the time measurement. The figure does show how well the carriage encoder system worked and that the two independent measurements co-varied with time.

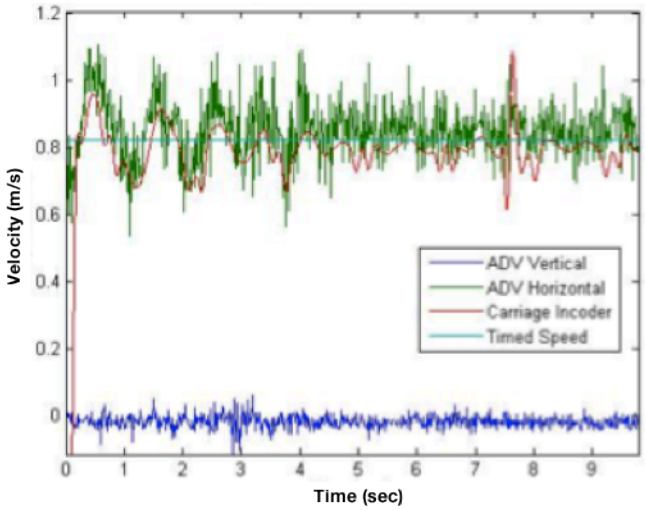

Figure 4.4 Validation of speed measurements using three different methods. Comparison of three independent speed measurements from the ADV, carriage encoder, and stopwatch during an unsteady acceleration.

4.3 Test Matrix

Measurements were obtained for different values of several key variables, including solidity, carriage speed, TSR, and blade positions. Table 4.1 shows the operating varibles, corresponding performance coefficient (Cp), and the measured variables.

Set	Solidity	Carriage Speed (m/s)	TSR	Performance (C_P)	Wake Variable	Blade Position
A	0.32	1.0	1.4	Optimal	Surface Elevation & ADV	Random
B	0.32	1.0	0.9	Off Optimal	Surface Elevation & ADV	Random
C	0.32	1.0	1.9	Off Optimal	Surface Elevation & ADV	Random
D	0.16	0.8	2.25	Optimal	ADV	Three Different Blade Positions
E	0.16	0.25-1.0	0.75-3.0	All Points	Surface Elevation	Random

Table 4.1 List of test preformed with turbine and measurement variables

4.4 Post-Processing

A post-processing procedure to analyze the velocity data was developed to transform these data into a usable form. This procedure included three steps: 1) rotating the ADV measurements to align with the reference coordinate of the tow tank (see Figure 3.16); 2) combining data from multiple runs of identical tests in order to produce a complete wake; and 3) running weighted windows to obtain statistical quantities with which to characterize the wake.

4.4.1 Coordinate rotation

In the first step, the three-dimensional velocity data had to be rotated from the sample volume reference coordinate (see Figure 3.12) to align with the reference coordinate of the tow tank (see Figure 3.16). As discussed above, the ADV angle changed with the orientation and vertical distance from the turbine center. There are two rotation matrices $R_i(f)$ because the ADV had two different orientations with different axie parallel to the reference coordinates. With one of the ADV direction symmetric with the reference coordinates the angle at which the ADV is

resting in the tripod was predetermined out side the tow tank. The angle (f) for each vertical distance is recorded and used in the post processing.

Rotation Matrixes

$$R_x = \begin{bmatrix} 1 & 0 & 0 \\ 0 & \cos(\phi) & -\sin(\phi) \\ 0 & \sin(\phi) & \cos(\phi) \end{bmatrix}$$

$$R_y = \begin{bmatrix} \cos(\phi) & 0 & \sin(\phi) \\ 0 & 1 & 0 \\ -\sin(\phi) & 0 & \cos(\phi) \end{bmatrix}$$

$$\begin{Bmatrix} u \\ v \\ w \end{Bmatrix}_{Ref} = R_i \begin{Bmatrix} u \\ v \\ w \end{Bmatrix}_{ADV} \quad (7)$$

The ADV was used in two different orientations, which is why there are two rotation matrixes seen above. Only two coordinates need to by adjusted for each case. In set A, the ADV was oriented to measured the true velocity in the x direction, so the R_X matrix was used. Similarly, set B measured the true velocity in the Y direction so that the matrix R_Y was used. With all the velocity data transformed to a common reference frame, data from multiple runs were compiled to form a composite two-dimensional wake field.

4.4.2 Velocity measurement range

The second step compiled measurements using different ADV measuring ranges that were obtained from multiple (usually two) runs of the same test set up. Two measurement ranges were needed because the lower measurement range was more sensitive to small velocity fluctuations but could not capture the highest velocities measured during testing. The low setting was able to measure a maximum velocity of 0.3 m s^{-1} with an accuracy of ±5 mm s^{-1}. As a result, the lower measurement range was used to capture the flow during the approach of the turbine and the dissipation in the far field. The higher measurement range sacrificed accuracy at low velocities, but performed well in the high velocity range when the turbine was close by, where the lower

measurement range was not usable. The high velocity range allowed a maximum of 1.0 m s^{-1} with an accuracy of ±10 mm s^{-1}. Therefore, the two measurement ranges were necessary to produce one composite set of data that represent accurately the full range of velocities during a testing.

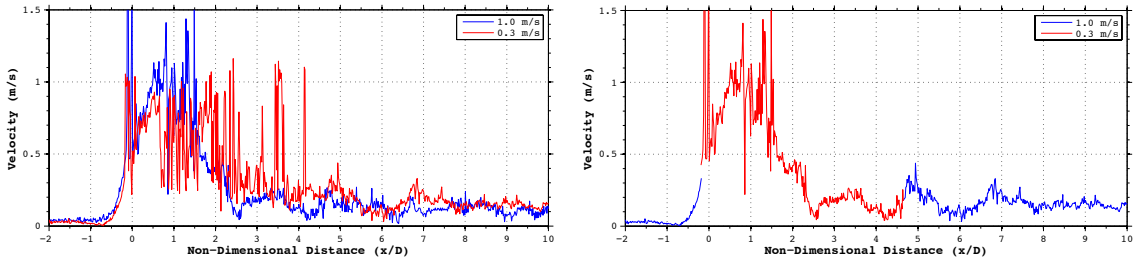

Figure 4.5 Combination of two data sets to form a composite wake. (Left) Two curves show the velocity measurements based on identical tests but using different ADV ranges. (Right) The composite wake

The procedure for producing a composite wake was similar to the process used to synchronize the ADV data file with the turbine data file. The two velocity ranges in the file pair were plotted together and the points that required a change in velocity range were marked. The two files were then patched together to produce one complete measurement of the wake. The differences between the two time series of different measurement ranges, however, complicated the merging process. Differences were partly due to random positions of the blade as the turbine passed the ADV, which caused poor correlations between the velocity magnitude and the distance to the turbine. Moreover, abnormal readings could result from a number of things occurring when the turbine was near the sample volume. One common cause for an abnormal reading occurred when the blades passing through the sample volume resulted in the signal-to-noise ratio going to zero and led to an unrealistic spike in velocity. Another cause for a corrupted point was the fact that velocity near the blade was out of range of the ADV. Figure 4.6 illustrates the process from the file pair to the result.

The repeatability of velocity measurement as well as the measurement with respect to four test variables (velocity range, blade position, ADV height, and carriage position) was validated by

comparing identical tests. The velocity measurements were compared and found to demonstrate strong repeatability over multiple tests with identical variables. The data set was shown not only to match the velocity magnitudes, but also to repeat small fluctuations at the same carriage and blade positions. Figure 4.7 shows the result from the blade controlled directly over the ADV as well as strong repeatability between a high and a low velocity range verses carriage position.

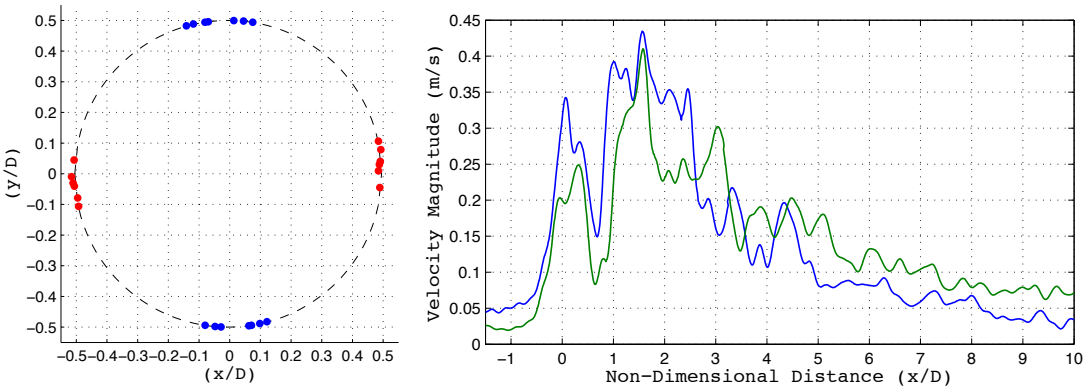

Figure 4.6. Results from the repeatability study concerning blade position and fluid velocity. (a) Results of blade position directly over the ADV, where each dot represents a blade position at x=0 (b) Velocity magnitudes of two independent tests showing strong repeatability from controlled blade position

5. WAKE CHARACTERISTICS

A numerical procedure was developed to process the raw data into four variables that describe the wake characteristics. The procedure utilizes the Reynolds turbulence model, in which the velocity measurements were converted into two time-dependent components, known as the mean and fluctuation terms. From the Reynolds concept other important variables and by acquired to determine the quantity, location and dispersion of turbulent energy in the wake.

5.1. Reynolds' Time Averaging Concept

Reynolds decomposition is a mathematical tool used to derive a fluctuation and mean term from single point velocity observations. The mean $\bar{U}$ and fluctuation $\grave{U}$ terms are two components that differentiate between steady and turbulent flow. The velocity was decomposed into the following form:

$$U_{measured} = \bar{U} + U` \tag{8}$$

The mean was calculated as a moving average over time (the averaging period will be defined in Section 5.2) and the fluctuation term was the difference between the measured value and the calculated mean. The need for the second equation is that the turbulence intensity (TI) analysis requires a modification to the standard Reynolds decomposition to avoid a mean nearing zero, in which case the mean is replaced by the root mean squared (RMS) to avoid singular points. The decomposition yielded four Reynolds terms for each of u, v, and w components and the magnitude U. The individual terms were used in the analysis and shown in the next chapter.

5.2. Turbulence Kinetic Energy (TKE)

The calculation of turbulence kinetic energy used the fluctuation term from the Reynolds decomposition to quantify the amount of kinetic energy per unit mass associated with the turbulent flow. The TKE is equal to the sum of the squares of the three-dimensional velocity fluctuations from the Reynolds time averaging concept:

$$\mathrm{TKE} = \frac{1}{2}(\mathrm{u`}^2 + \mathrm{v`}^2 + \mathrm{w`}^2) \tag{9}$$

In addition to describing the amount of turbulence present in the water, the distribution of TKE also shows where the turbulence occurs with respect to the turbine and where dissipation occurs behind the turbine.

5.3. Reynolds Stress

Velocity fluctuations can also be used to determine the rate of momentum transfer across a boundary. Momentum transfer is equivalent to the application of stress (see equation 5.3), which also shows the transfer of energy through the flow field. Together with the turbulent kinetic energy and Reynolds stress show the amount of the turbulence energy and is direction of transfer. The Reynolds stress is shown below as Equation 10. The equations are simplified by introducing two statements that result in three relevant terms. The laminar shear was calculated for a few random samples and was shown to be consistently smaller in magnitude than the turbulent contribution.

$$\tau_{RS} = \begin{Bmatrix} u` w` \\ u` v` \\ w` v` \end{Bmatrix} \tag{10}$$

All the stress variables have units of force per unit area, and dimensions of $ML^{-1}T^{-2}$. The correlation between two orthogonal velocity components leads is defined as the Reynolds stress. A three-by-three matrix representing the three-dimensional velocity measurements is usually used to depict the Reynolds stress. However, due to the large amount of data, the stress was represented by the magnitude of the traction vector, the last expression in equation 5.6.

5.4. Numerical Processing

To obtain the wake characteristics, the following numerical procedure was developed. The objective of this process was to decompose the observed velocity data into mean and fluctuations while maintaining a level of resolution as well as a degree of dynamic range in conjunction with applying a running window to a segment of single point data.

5.4.1. Running window

The running window is a statistical operator that evaluates a segment of data within a much larger sample array. The numerical tool calculates the mean and fluctuation components from the raw data based on the Reynolds time averaging concept. This is achieved by using a significantly smaller number of data points to produce a single value assigned to the middle point in the window. The window then runs through the entire sample array to result in a new processed array. Figure 5.1 illustrates the running window for a single data point.

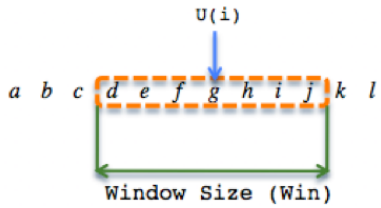

Figure 5.1. Functionality of running window

The running window is a type of low-pass filter, or more precisely, a finite impulse response filter, in which the cut-off frequency relates to the size of the running window. The numerical operation used to convert the measured velocity to its time-averaged components resulted in unintended effects of reduced Nyquist frequency. Since one of the objectives of this research is to study the fluctuation in the flow caused by the turbine, a low Nyquist frequency could threaten the relevancy of the research. For example, if the windows were wide and constant (i.e., box-car), the moving operation would produce filtered data for which the Nyquist frequencies were significantly lower than the original. Additional numerical techniques were explored and implemented to reduce the effect on the cut-off frequency and are discussed in section 5.5.2 and 5.5.3.

5.4.2. Weight Function

A weight function is a mathematical operation used during convolution in order to give specific elements more influence on the result over less relevant elements in the same segment of

data. Constant weight functions are characterized with a low dynamic range, as a result a poor choice for turbulence analysis, which requires a high dynamic range. Conversely, a weight function that is designed to handle the presence of fluctuations in frequency and amplitude suffers from low resolution and a high sensitivity to random noise. Spectral analysis shows the tradeoff between resulting signals' strength with comparable frequencies, and resolving dissimilar strength of signals with dissimilar frequencies. The Hamming function, seen in Figure 5.2 below, is a compromise of these two extremes that provided a favorable frequency response. How to choose the size of the window will be addressed below.

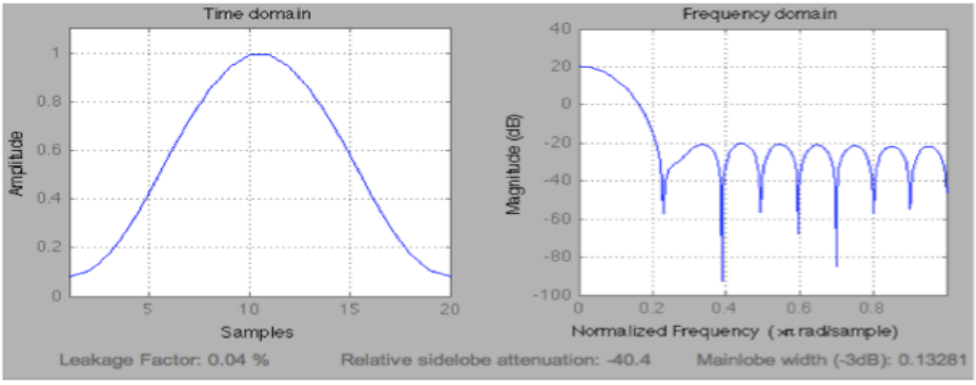

Figure 5.2. The Hamming weighting functions and their effects on the frequency domain

The advantage of the Hamming window is low aliasing, and the tradeoff is the decrease in resolution through lowering and widening the main lobe. For the Hamming window shown in Figure 5.2, the effective Nyquist frequency was lowered to 10 Hz from 32 Hz after the application of the weighted running window. If the weighting function were constant, the resulting cut-off frequency would have been drastically smaller, at approximately 1 Hz. All the calculations were done by producing a signal of know frequencies and amplitude and looking at the frequency response of the running weighted window.

5.4.3. Window Size

The size of the weighted running window had a significant effect on the results. Figure 5.3 shows the magnitude of the velocity converted into the Reynolds time-averaged mean ($\bar{u}$) and fluctuations ($\acute{u}$), in which the window size was incrementally increased from 4 to 64 data points. Figure 5.3 depicts the strong variability of the results, indicating the importance of finding the ideal window size. Two methods were utilized in order to determine the best size of the window: using the experimental results and assuming certain physical attributes.

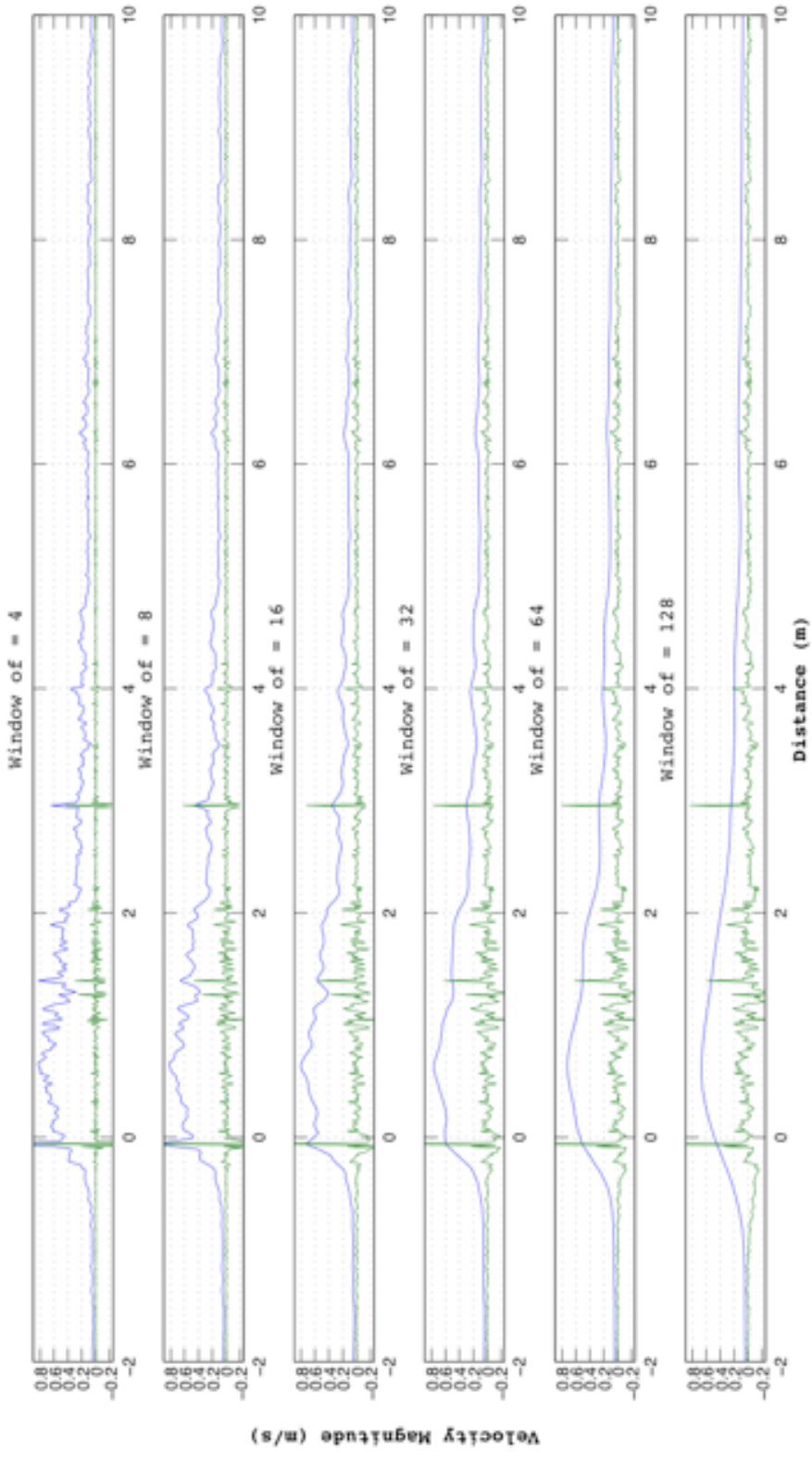

Figure 5.3. Mean and Fluctuation results of Reynolds decomposition for different window sizes

The first method examined the effect of a changing window size on the Reynolds components. The window size was incrementally reduced over a segment of measurements of a creep flow. The results from the algorithm produced average fluctuations and mean values for one window size through the entire segment. Figure 5.3 shows the change in the mean and fluctuations quantities as a function of window sizes. The result yield a region of stability with a point of inflection and constant height at a window size between 15 to 25 which suggested a range to set the window size. Other assumption can be applied to further understand the effect of a changing window size to determine the optimal size.

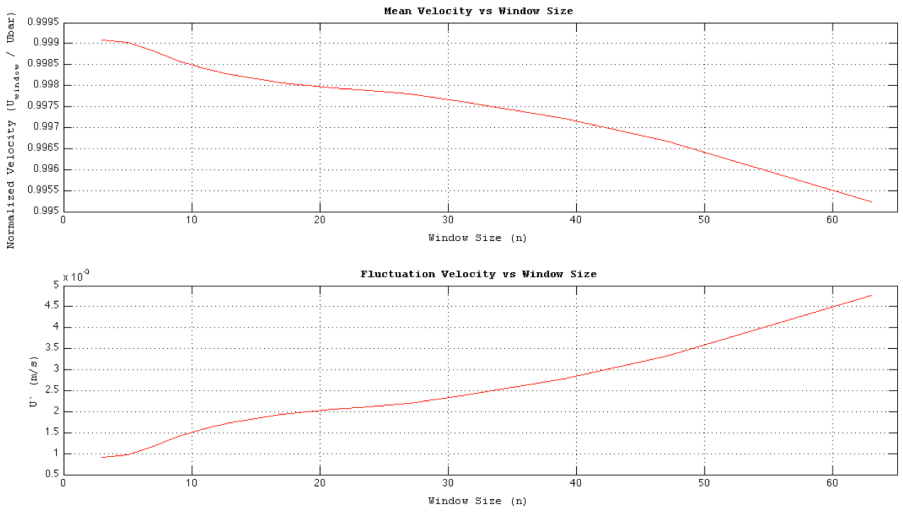

Figure 5.4 Results of Reynolds decomposition for different window sizes

The second method used to determine an optimal window size focused on the energetic and turbulent period behind the turbine. The second method assumed that the velocity in the y-direction are only the fluctuations (v') components. In a process similar to the first method, window size was varied and v' and $\overline{v}$ were studied, where the objective was to return $\overline{v}$ to zero. The variation of the window size from 4 to 128 significantly reduced $\overline{v}$ with the largest effect seen below 40, however, $\overline{v}$ only approached zero resulting in a horizontal asymptote as a function of window size. With the results from both methods and the effect of the Nyquist frequency calculated from the weighted running window, the window size of 25 data points was chosen as the ideal size for this study.

5.5 Wavelet transforms

An additional numerical tool used for analysis was a discrete wavelet transforms use to capture both frequency and time information associated with flow field. Other experimental fluid studies have used similar time-frequency spectrum methods to examine turbulent behavior (Rinoshika 2007, LI 1999). The analysis was used to capture both frequency and time/distance information associated with the flow field. The time-frequency spectrum has additional advantage of temporal/spatial evolution over the traditional Fourier transform, which is needed for highly time-dependent structure of a wake. The frequency range of the spectrum, from 0.03 Hz at the base to 32 Hz at the top, was determined by the experimental method and equipment. The analysis was done on the velocity magnitude, $(u^2+v^2+w^2)^{1/2}$, from all sampling heights

5.6 Visualization techniques

The results are presented in a non-dimensional format to provide a unified representation of the data, independent of the physical shape and operation settings of the experiments. Segments of data were presented as a distance between the turbine and the velocity of the fluid, and were measured in length and velocity units. In order to utilize a non-dimensional format distance, the unit of length was converted to length per turbine diameter. As a result, the horizontal and vertical distances are depicted in terms of turbine diameters. Similarly, the fluid velocities are presented in a non-dimensional format normalized by the carriage speed.

The velocity measurements are presented to generate a flow field in two forms. The simplest is the vector plots to better understand both the near-field and far-field characteristics. Each vector was calculated from a mean of four individual unprocessed three dimensional velocity points. A reference circle is used in to represent the turbine in all the figures and blade position is marked for the low solidity turbine. The aspect ratio, which can be inferred from the shape of the circle, was used to maintain the correct representation of the data.

6. RESULTS

The differences in the flow field over two different solidity ratios as well as additional measurements on the effect of TSR and blade position were acquired to examine the dynamic flow behaviors of a cross flow turbine. The two different turbine solidity and their arrangements are defined in the turbine Section 3.2 as well as the results from the dynamometer for the different turbines are shown in Table 3.4. For the two different turbine configurations, one variable was altered at a time to examine different effects of the controlled variable on the flow field, and the variables are listed in the test matrix in Table 4.1.

6.1. Composite Flow Fields

The results for the flow field are illustrated as a vector plot showing the magnitude and direction of the two velocity components as the turbine approaches and departs. The flow field is shown in the x-z plane where the third velocity component (v) is not represented in the vector plot. The flow fields are shown twice to highlight different stages in the wake showing the two regions referred to as the near field and the far field. The far field displays the flow decay down steam while the near field shows two stages of the wake in the region close to the turbine.

Overall, the responses were the strongest near the turbine depth and decreased with the distance away from the turbine centerline. Furthermore, the responses were almost symmetric about the centerline before the turbine passed overhead the ADV ($x/D = 0.5$), but the symmetry gradually disappeared downstream. The entire flow fields can be divided into three stages. The first stage is the turbine approach when the u-velocity gradually increased while w-velocity was upward above the centerline (ACL) and downward below the centerline (BCL), indicating the water being pushed away as the turbine approaches. The second stage shows the entrained flow. During this stage, the u-velocity near the turbine heights accelerated quickly to a peak speed about the speed of the carriage, which then decelerated between 1 and 3 turbine diameters. Away from the turbine ($z/D \geq 0.75$), the u-velocity was opposite to the carriage moving direction in the

beginning of this stage, but the direction reversed as the entrainment spreading towards the surface and the bottom to reach the depths. The w-velocity during the second stage first decreased at all depths followed by a small collapse towards the centerline then even stronger expansion towards the surface and the bottom. After the collapse of the entrained flow the third and final stage is the wake tail that consisted of small fluctuations. These fluctuations decayed rather slowly over a large distance, and their magnitude could still be 10 percent of Vc at x/D = 14.

6.1.1 High Solidity Turbine

The high solidity turbine used a four-blade configuration and measurements where obtained over three different TSR values. The optimal TSR of 1.4 was the focus of the high solidity data set with velocity measurements at three different distances from the turbine center to the sample volume: 0.43, 1.0 and 1.3 diameters. A high solidity turbine, with a value above 0.2, has been shown in this and other studies (Shiono 2000) to be less efficient than a low solidity turbine, by as much as ten percent on comparison with a similar turbine setup. As a result, a raised solidity requires a lower TSR to achieve its optimum performance. The lower TSR reduces fish strikes, resulting in conservational incentives for turbine developers to use a higher solidity turbine (Polagye 2011).

The experimental work for the four-blade turbine was performed before the repeatability of the blade position was addressed. As a result, the blade position in test set A was random, i.e., the blade position was recorded, but not controlled. However, the data demonstrated a strong degree of repeatability and correlation between different runs of identical tests when the two-velocity ranges were combined to form a composite wake profile. The correlation between different runs only matched the velocity magnitude and direction. Small variations existed with the mean components between matching velocity range, thus, the tests were concluded to be first-order repeatable. The repeatability across runs suggested that the blade position was not a large

factor on the flow field for the high solidity turbine. From the correlation across equivalent wake results, the wake appeared to be stable in size and intensity. This hypothesis was further supported by the turbine forces through a rotation having an amplitude and frequency associated with each force, however the high solidity and most notably the high number of blades produce small amplitudes in all the forces. The mean of the osculating forces are the coefficients seen in table 3.4. The force frequency is four time higher then the rotational frequency.

The results seen in Figure 6.1 and 6.2 show the different stages of the wake, approach, entrained flow, and flow recovery with respect to the turbine. The level of symmetry between the opposite sides of the turbine, suggests that the blade position and the turbine rotation were not strong factors in the wake and the turbine acted similarly to a cylinder in a uniform flow.

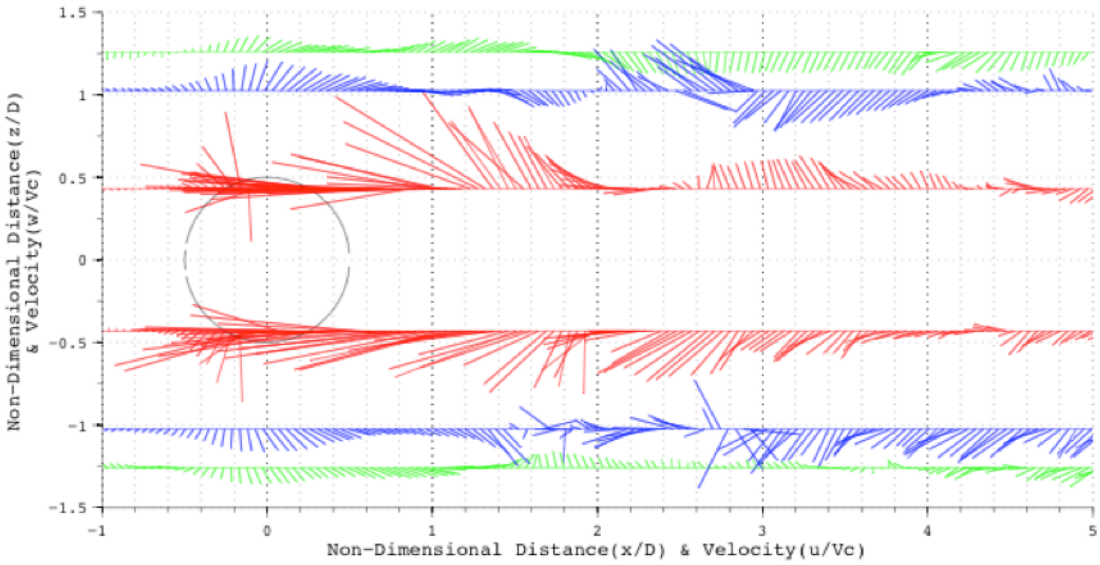

Figure 6.1 Near flow field for high solidity turbine operating on design

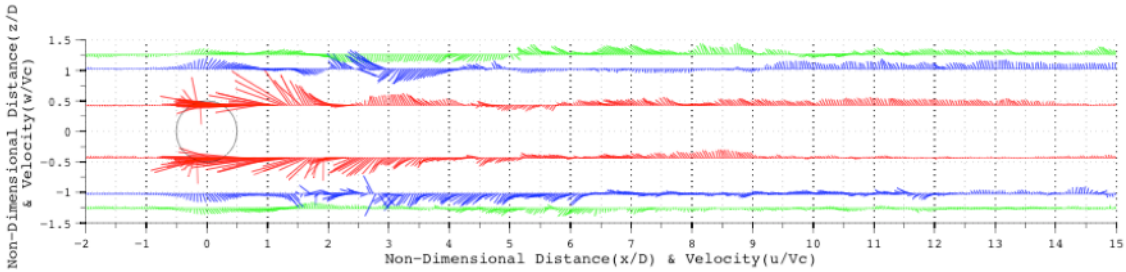

Figure 6.2 Far flow Field for high solidity turbine operating on design

In addition to the optimum TSR at 1.4, two off design TSR were tested with the four-blade turbine and the results for the off design turbine are shown in Appendix B. The results for the off design show similar traits such as the bypass flow entrained flow and flow recovery.

6.1.2 Low Solidity Turbine

The low solidity turbine wake data includes three different blade positions for a carriage speed at 0.8 m/s and the optimal TSR of 2.25 for maximum C_P. The low solidity turbine used only two blades that reduces the solidity by half compared to the high solidity arrangement. The reduction in the number of blades caused significant differences in the flow pattern through the 180° rotations, which led to the control of blade positions over the ADV instead of random blade

position in the high solidity data set. The data set includes three-blade position at 45° intervals, as well as the four different locations for the ADV's sample volume to the turbine center: 0.51, 0.77, 1.1, and 1.5 diameters.

In all cases shown in Figure 6.3, the different stages of the wake were noticeable: the first was the gradual diversion in front of the turbine, beginning at about 0.5 diameter in front of the turbine. The second stage was the entrained region behind the turbine that traveled in the direction of the carriage at speeds close to that of the carriage. With the final stage, the dispersion and decay of the wake.

In all cases of different blade position for the low solidity turbine show an asymmetrical structure between upper and lower sections in Figure 6.3. The asymmetry of the wake was not observed with the high solidity turbine (see Figure 6.1 and 6.2). During the turbine approach, the wake below the centerline (BCL) showed more flow activities in comparison to above the centerline (ACL), resulting in a higher bypass flow BLC. Additionally, the ACL area experienced a stronger response in flow magnitude and variability, emphasized by an upwelling through all levels. The blade travels with or against the inflow; depending on which side of the centerline the blade is located. Since the TSR is equal to 2.25, the blades at top will travel into the flow with a maximum speed at top dead center of 3.25 times faster than the inflow. As for the lower blade located at bottom dead center the flow passes from the leading edge to the trailing edge at a speed of 1.25 times the inflow.

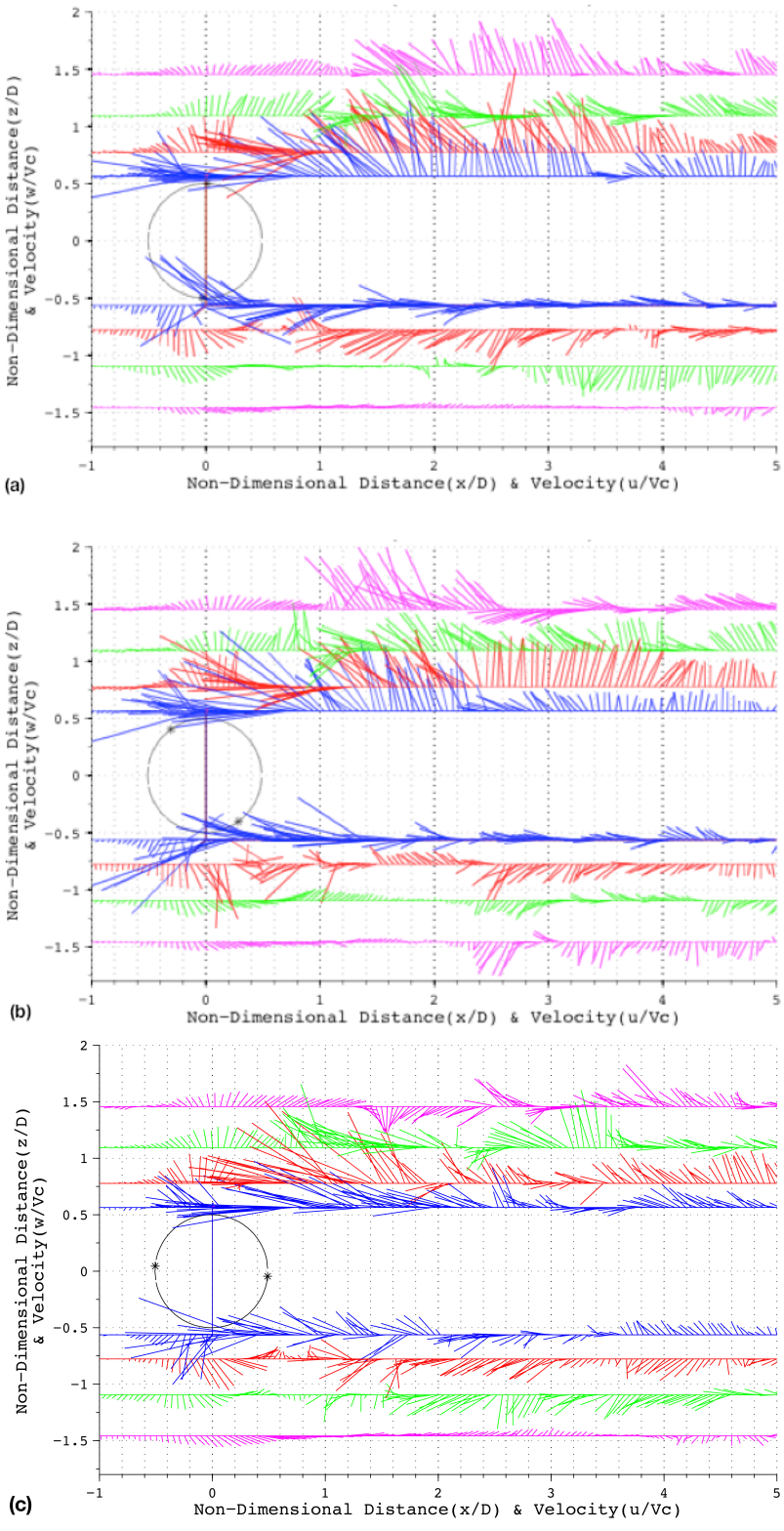

Figure 6.3 Near flow fields for low solidity turbine over three-blade position.
(a) Position 1 (b) Position 2 (c) Position 3

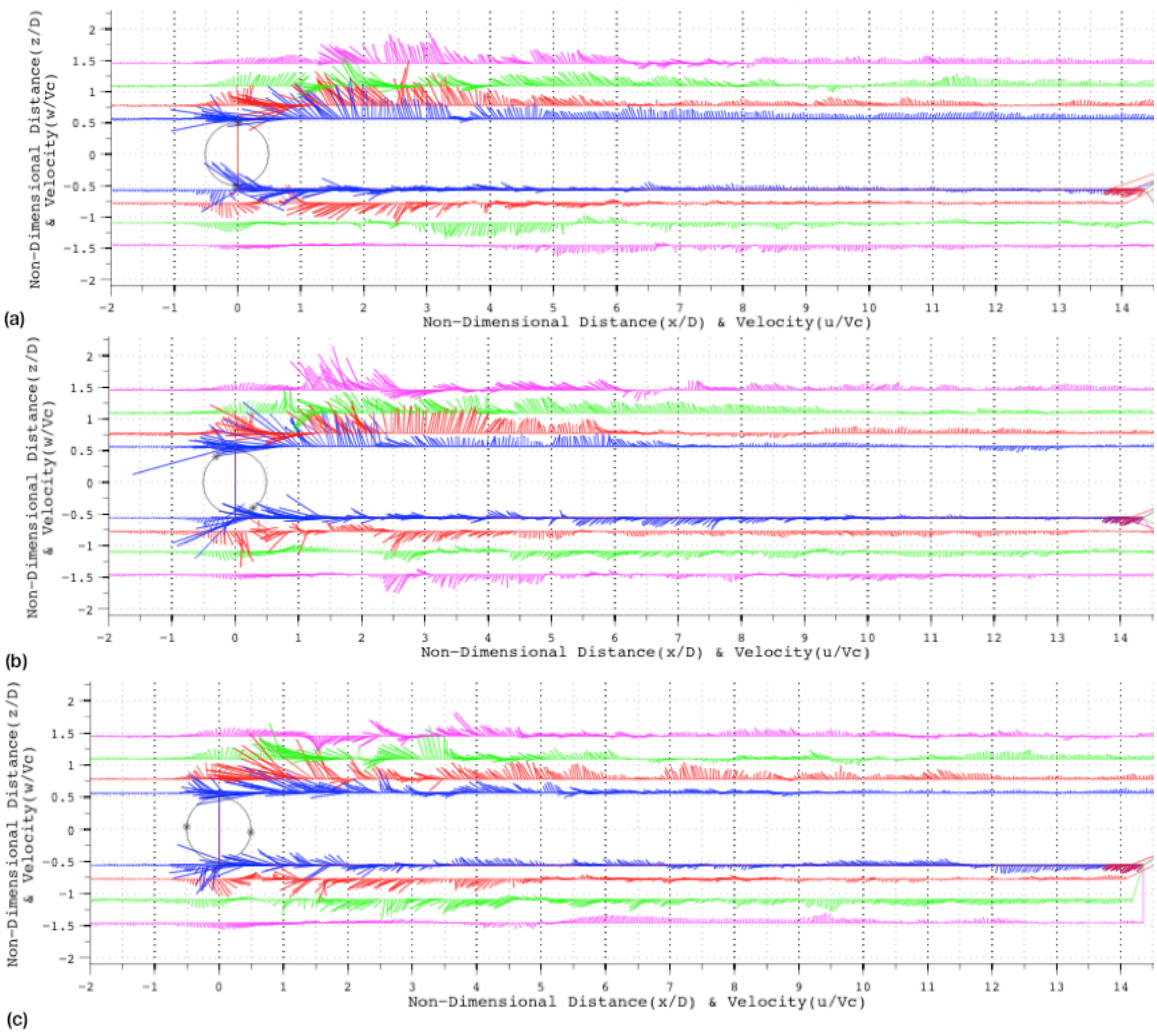

Figure 6.4 Far flow fields for low solidity turbine over three-blade position.
(a) Position 1 (b) Position 2 (c) Position 3

6.2 Reynolds Time Averaging

To further examine the wake, the data has been separated into the mean and the fluctuation components. The separation of the two components made it possible to examine the connection between the mean and fluctuation terms, with respect to the distance from the turbine. The connections between the mean and fluctuation terms are examined in more detail in section 7.1. The velocity measurements for the high solidity turbine are shown in Figure 6.5 and 6.6. The two figures together show the structure and behavior of the flow field with the velocity magnitude shown in Figure 6.5 and the three-dimensional components in Figure 6.6. The

velocity magnitude demonstrates the average influence of the turbine over the quasi two-dimensional field where the separation of three velocity components shows how the flow translates through a three-dimensional space. The individual velocity components display a phase relationship between the u, w, and v, especially during the flow accelerations. The phase relationship was measured throughout all layers as the momentum disperses outward, affecting the outer layers to a lesser extent. The figures shown include only the near field in order to illustrate the behavior of flow recovery as the momentum transfers out from the x-direction and into all other directions. To see the details of the interior wake measurements, additional figures for each velocity component are provided in Appendix B.

Small oscillations still exist in the case of high solidity turbines but are lower in amplitude and higher in frequency due to the large number of blades. Therefore, the velocity fluctuations in general are considered relatively stable. With the fluid interaction being steady, the wake should have steady size and shape. The steady wake structure was further supported during the process of making a composite wake, in which different files of the same test demonstrated a repeatable pattern in the mean flow.

Other physical properties such as the bypass flow, the shear front, and the blockage effect can be seen in Figure 6.5 and 6.6.

- As the turbine approached a steady flow around the turbine is observed w components with the largest velocity outward at approximately -0.2 diameters in front of the turbine. Followed an abrupt change in direction. The velocities upstream are predominantly in the w but after the abrupt change, w goes to near zero and velocity in the u dominates.
- Through the different heights, two different fronts are observed as the wake propagates outward and dissipates. The first is the steady flow as the turbine approaches dominated by u and w velocity components with diminishing strength in the outer layers occurring simultaneously throughout the layers. The second is the turbulent front dispersing

outward by oscillating w and v components, that are apparent in the time-frequency spectra analysis where.

- A feature of the blockage effect can be noted in the outer layers where the u-mean velocity is travels in the opposite direction of the entrained flow.

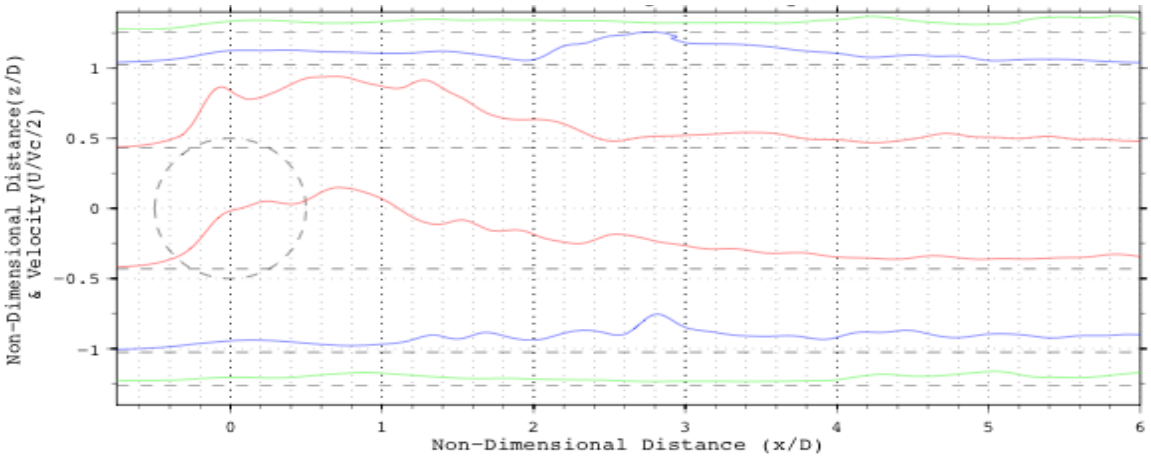

Figures 6.5. The velocity magnitude mean from the Reynolds decomposition for the high solidity turbine.

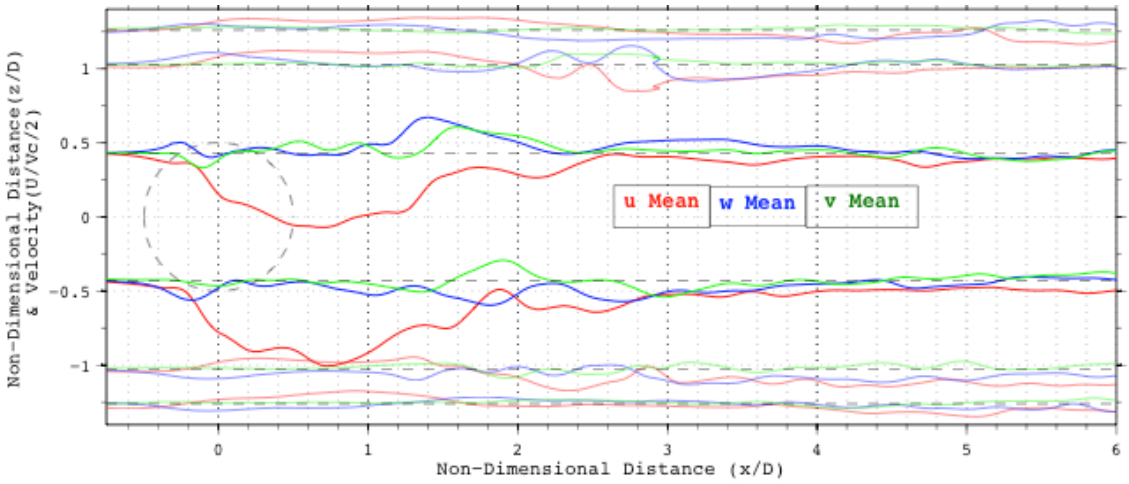

Figures 6.6 The three (u, w, v) mean velocity component of Reynolds decomposition for the high solidity turbine.

Similar features seen in the high solidity turbine is observed in the low solidity turbine's mean velocity components in Figure 6.7 and 6.8. The two turbines share similar flow recovery at the distance of 10 diameters downstream, approximately 10 to 15 percent of inflow speed in $\bar{U}$ (at all heights) remained while the velocity in the u remains below 5 percent. The remaining flow persisted for a long distance, and did not begin to dissipate until approximately 30 to 35 diameters away (not shown). However, one major difference is the low solidity turbine's wake is asymmetric compared to the high solidity. Unsteady flow pattern are seen through the different blade position where the velocity in front of the turbine dependent on the blade position.

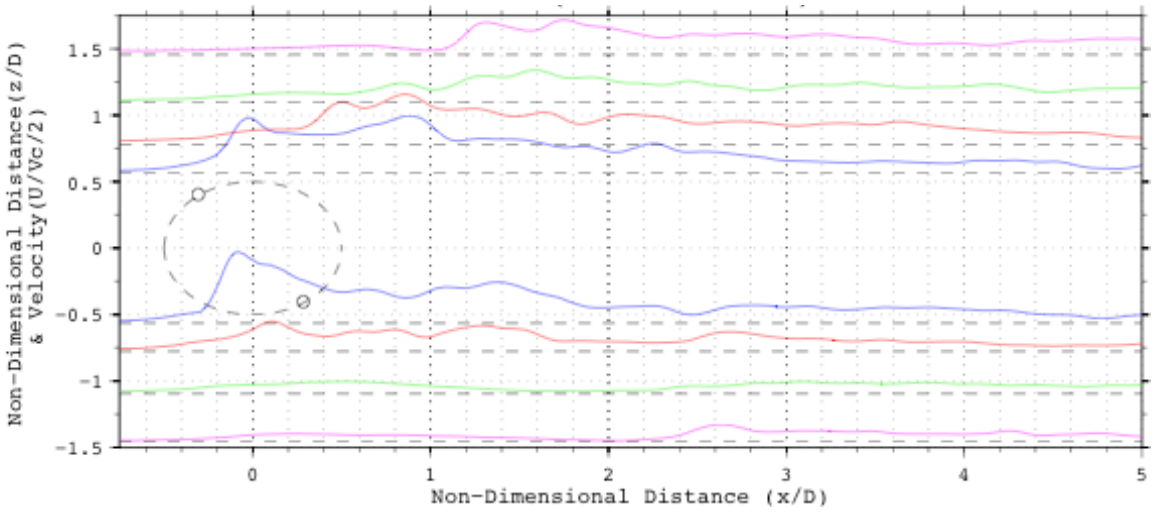

Figures 6.7. The velocity magnitude of Reynolds decomposition for the low solidity turbine for blade position 2.

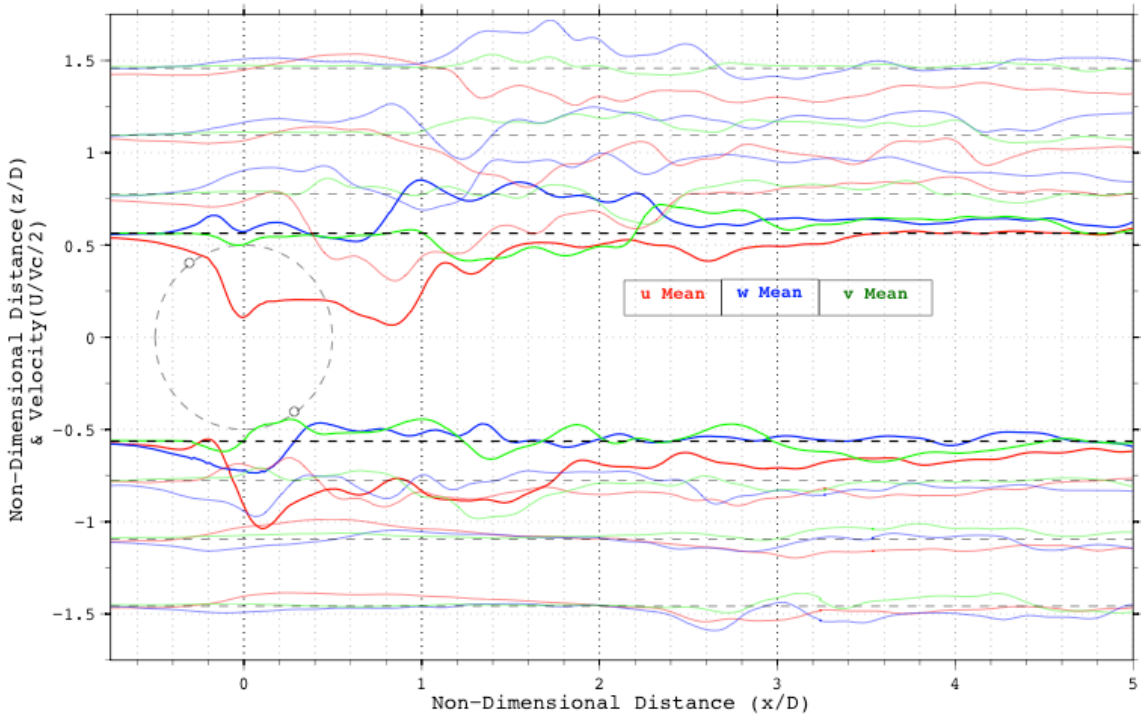

Figures 6.8. The three-dimensional mean velocity component (u w v) of Reynolds decomposition for the low solidity turbine for blade position 2.

- ACL at z/D = 0.5, $\overline{u}$ increases quickly to Vc; away from the turbine, the flow starts by moving towards left, but reverses immediately behind the turbine, then changes to leftward again when the first wave of upward spreading disturbance from the blade reaches the sampling height and the magnitude decreases as the distance from the centerline increases; the decay further downstream is slower and the decay rate decreases with the distance from the centerline.

- For $\overline{w}$: Water is pushed away from the centerline as the turbine approaches so that $\overline{w}$ is positive ACL and negative BCL. Conversely, the water rushes back towards the centerline immediately behind the turbine. However, the expanding wake is associated with upward motions ACL and downward motions BCL.

- $\overline{v}$ oscillates: A phase relationship exist between in the three mean velocity components in the flow recovery region one to two diameters downstream. As $\overline{u}$ recovers downstream generate a negative acceleration resulting in positive acceleration in $\overline{v}$ and $\overline{w}$ showing the velocity to be redirected into other direction. This phase relationship between the three velocity components are seen in best in Figure 6.8 and from the phase relationship between $\overline{v}$ and $\overline{w}$ being in phase with each other, it can be best described by an eddy. Furthermore, the final significant decrease in all velocity components is marked by sudden flash of fluctuation velocity.

6.3 Wavelet Spectrum

A time and frequency analysis was done on the velocity magnitude using a discrete time frequency spectra. Figure 6.9 shows the time and frequency response for the single sample volume adjacent to the top of the turbine ($z/D \approx 0.5$) at Blade Position 1. Figure 6.9 is the only figure that includes the second frequency axis from 0 to 32 Hz on a linear scale. Figure 6.9 also shows three distinct bands in the time demand associated with the turbine overpass collapse of the entrained flow, and the turbulence. The first band, located at zero distance, is associated with the turbine passing over the sensor, and exhibits the largest response over a large frequency range. The first band was followed by a brief period of low intensity fluctuations at 15Hz and above. Fluctuations at while the 15Hz and below does not occur until approximately two diameters past the turbine. The second band had only a few frequencies present over the frequency range due to the abrupt acceleration from the flow recovery. The third and other bands are typically observed at high frequencies near to the Nyquist frequency and are typical with large fluctuations over a brief period. These flucuations are the result of random turbulence and has no significant on this analysis.

Figure 6.10 shows two wavelets stacked together using the same visual arrangement with the x-axis of the wavelet located at the respective sample volume height. The stacked time-frequency spectra show the propagation of the fluctuation energy away from the turbine with a distinct shear front. In addition to the propagation outward, the decay of the energy fluctuation is also apparent. The scale chosen is log based 10 scale providing a wide amplitude range.

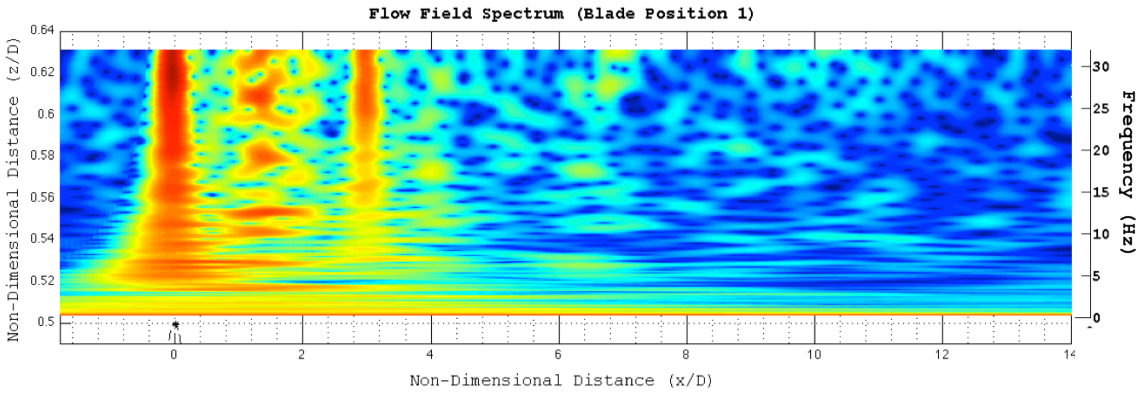

Figure 6.9 Time and frequency response for the sample volume adjacent to the top of turbine at blade position 1.

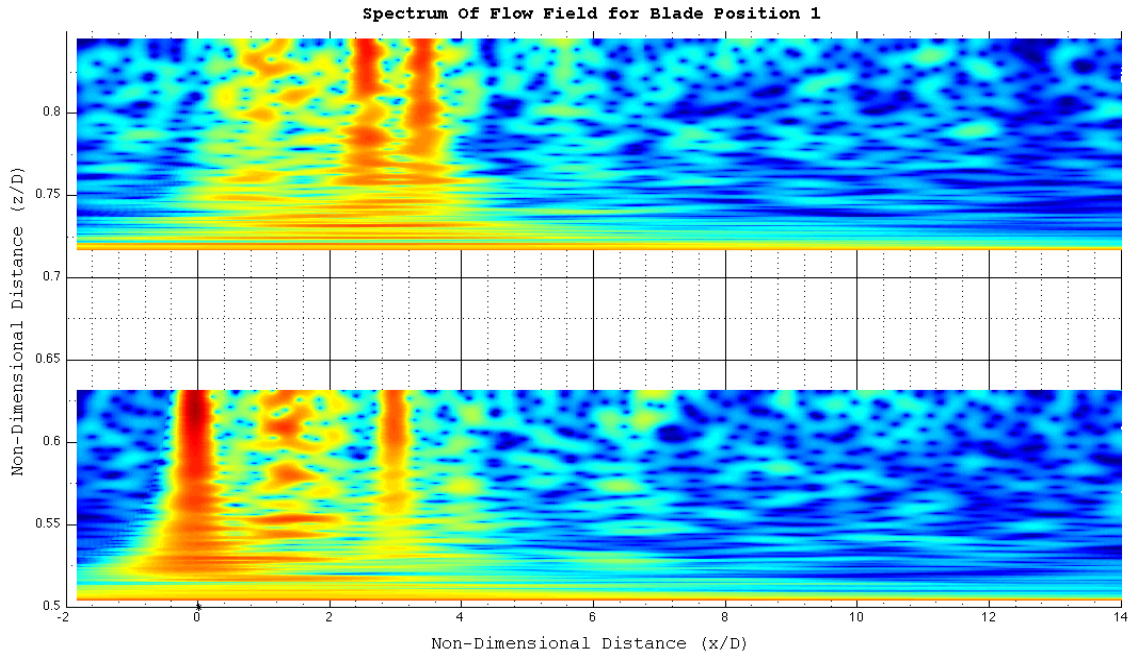

Figure 6.10 Two time and frequency responses stacked with the sample volumes on the top of turbine at blade position 1.

The wavelet spectra were placed together with respect to the sample heights. Although the visualization technique in Figure 6.11 sacrifices the resolution of each individual peak, it allows all the information to be viewed in a single reference frame. Figure 6.11 shows the spread of fluctuation from the centerline and the dissipation behind the turbine for the high solidity turbine operating at an optimal TSR.

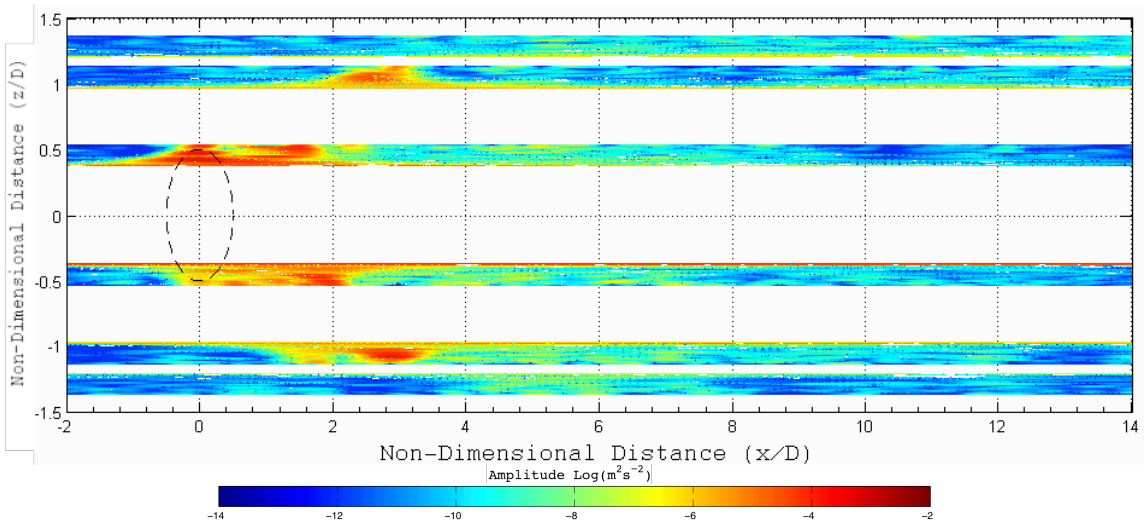

Figure 6.11 Time and frequency response from wavelet analysis for high solidity turbine operating on design.

For the low solidity turbine three time-frequency spectra are shown for each blade position in Figure 6.12. The figures also show constantly shifting behavior of the turbulent energy as the blades change position, resulting in different shear planes throughout the wake. For example, blade position 1 and 2 have the largest responses at zero distance to the turbine, as would be expected with the blade's proximity to the sample volume. On the other hand, blade position 3 has the largest area with high fluctuation. A real integration of the spectra shows that blade position 2 has the largest amount of energy, as seen in Table 6.1 below. As the table shows, there is a large variation in measured energy, further demonstrating a continuously changing wake.

Position	1	2	3
$\frac{\iint A(x,f,i)\,dxdf}{[\iint A(x,f,i)\,dxdf]_{Max\,(i)}}$	0.75	1.0	0.65

Table 6.1 Qualitative comparisons wake energy spectrum for the three different positions

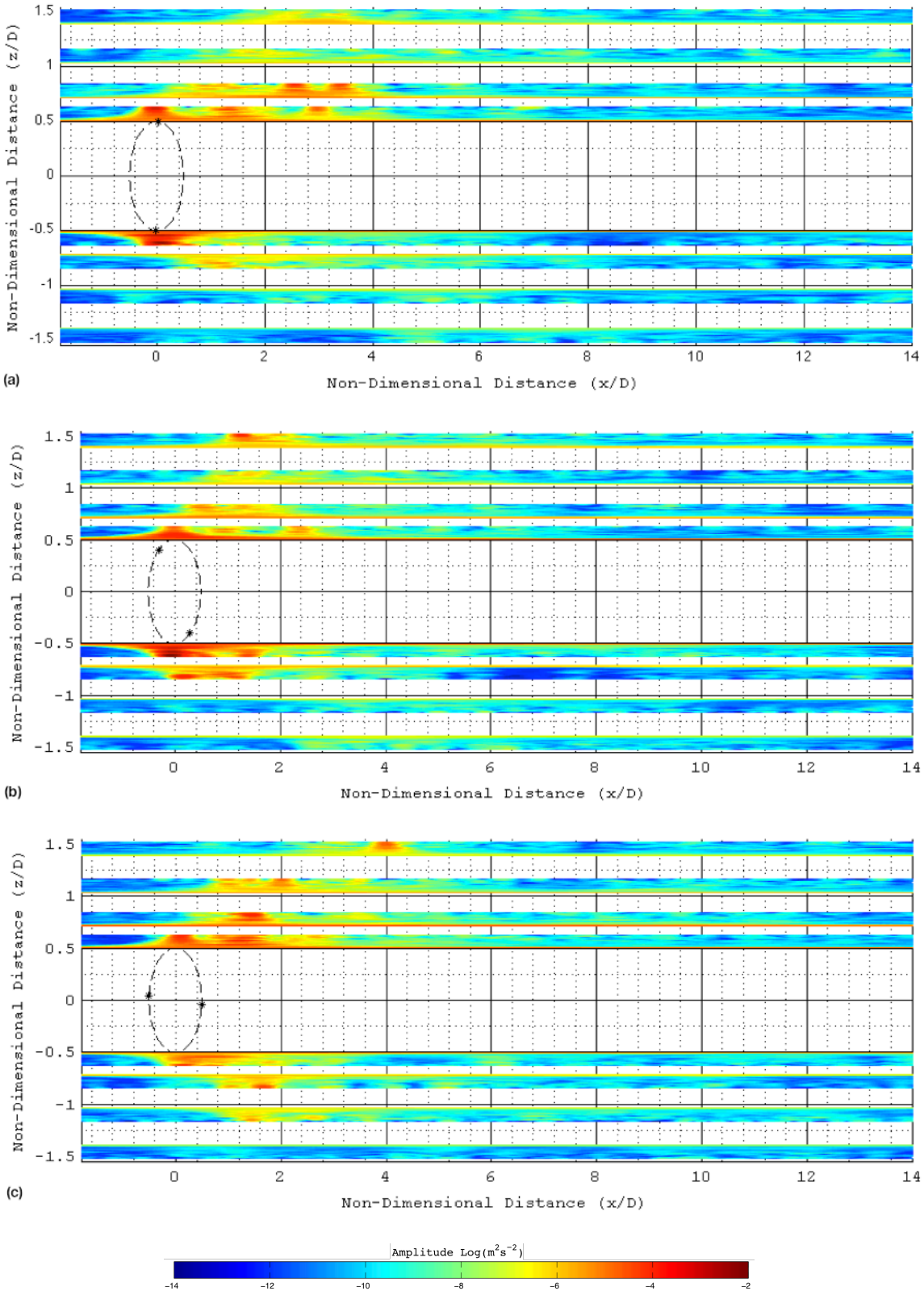

Figure 6.12 Wavelets for each height and blade position showing the fluctuation intensity as a function of frequency and distance to turbine. (a) Position 1 (b) Position 2 (c) Position 3

6.4 Turbulence Kinetic Energy and Reynolds Stress

Turbulence commonly contains coherent structures such as eddies, however, point measurements can only acquire fluctuations from the turbulence. The resolution of equipment and methodology used in this study will not show individual eddies instead focusing on the distribution of turbulence in a quasi two-dimensional regions. The measurements have shown localize regions near the turbine and the dispersion of the TKE outward. The results for the high and low solidity turbine show different behavior between each other but maintain a general simultaneity in size, intensity, and dispersion of the TKE. However, a notably difference was measured in the decay rate down stream of the turbine.

The high solidity turbine exhibited a highly organized and symmetrical TKE also seen above in the velocity results. The TKE showed a distinct connection to the flow recovery seen in Figure 6.6 where the flow recoveries in the same region as TKE go to zero. The high solidity turbine results in Figure 6.13 shows how the TKE is confined to a small region over three diameters in length with two well-defined peaks. The TKE for the inner layers are contained within a small region but are bounded by a rapid increase in energy at approximately zero as well as a rapid decrease between 1.5 and 2.5 diameters. The results also show the dispersion of the turbulent energy outward through the layers, exhibiting the shear front. As the TKE disperses to the outer layers the peak and boundaries are reduced.

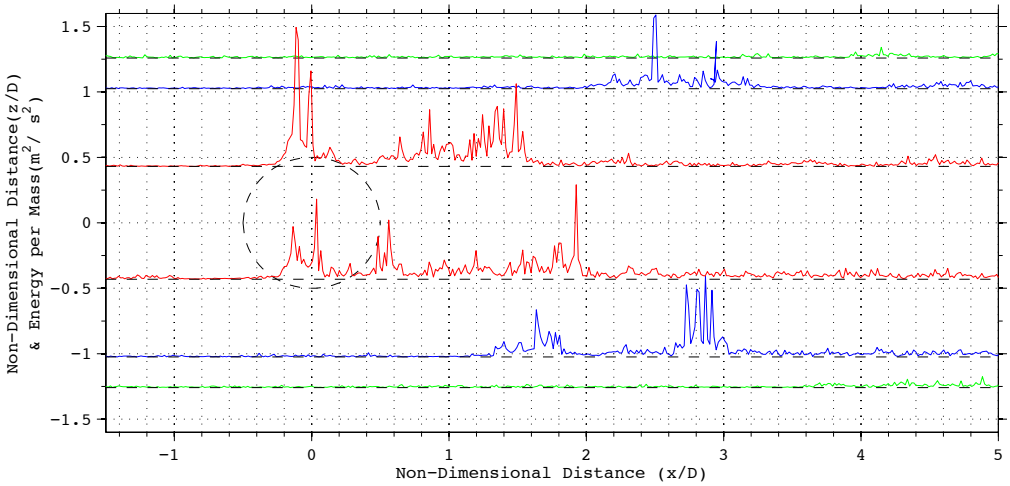

Figure 6.13 Turbulence kinetic energy terms for high solidity with optimum TSR

The TKE results for the low solidity turbine did not show a confined region of turbulent energy with a rapid decay as seen in the high solidity measurements. The TKE results demonstrate an asymmetrical feature of the wake favoring the ACL region. The low solidity turbine also showed little to no disturbance in the bottom two heights of the sensor. The different blade positions show that the fluctuation in magnitude at the strongest area of turbulence depended on the blade's position. The low solidity turbine's TKE shows similarities to the high solidity: the general structure of approximately two regions of high activity associated with the overpass and the flow recovery. However, unlike in Figure 6.13 where the TKE has a sharp decline near zero, Figure 6.14 shows a fluctuation in distance and magnitude at approximately two diameters, with addition regions of high activity. The results for the TKE show a slower approach to zero compared to the high solidity with approximately one diameter long required to reach a similar energy level.

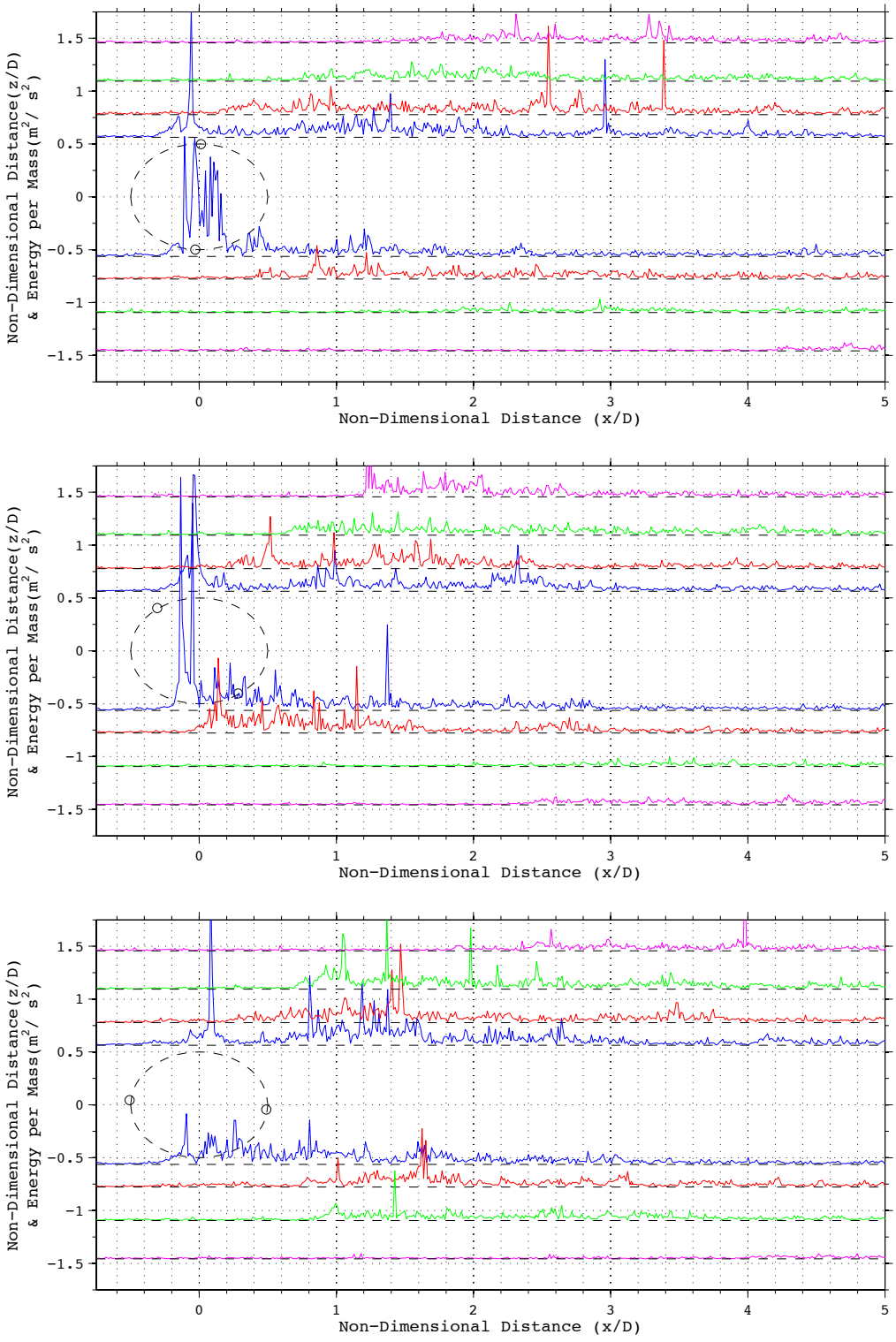

Figure 6.14 Turbulence kinetic energy for low solidity turbine over three blade positions. (a) Position 1 (b) Position 2 (c) Position 3

The transfer of turbulent energy can be seen with the Reynolds shear. Data from the ADV was well suited for measuring the turbulent shear by using its internal software and the procedure used for data collection. The results, seen in Figure 6.15, demonstrate the transfer of momentum from the turbulent motion across the three orthogonal panes in Cartesian coordinates for at each height. The Reynolds shear components are the dominant quantities responsible for momentum transfer in turbulent and transitional flow. The nature of the cross flow turbine operating over a range of angles of attaches that introduces dynamic stall over a rotation produces a turbulent wake.

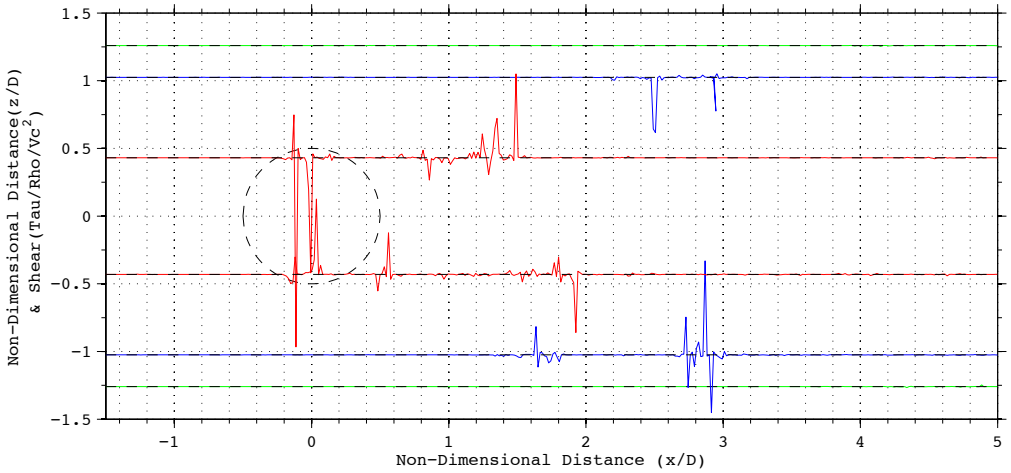

Figure 6.15 The u`w` Reynolds shear component for four blades with optimum TSR

The results for the low solidity turbine are seen in Figure 6.16 which constantly changed due to the changing rotation of the turbine. For instance, the distance between the peaks of both Reynolds shear and TKE changed as the turbine rotated, while the magnitude of both remained relatively constant.

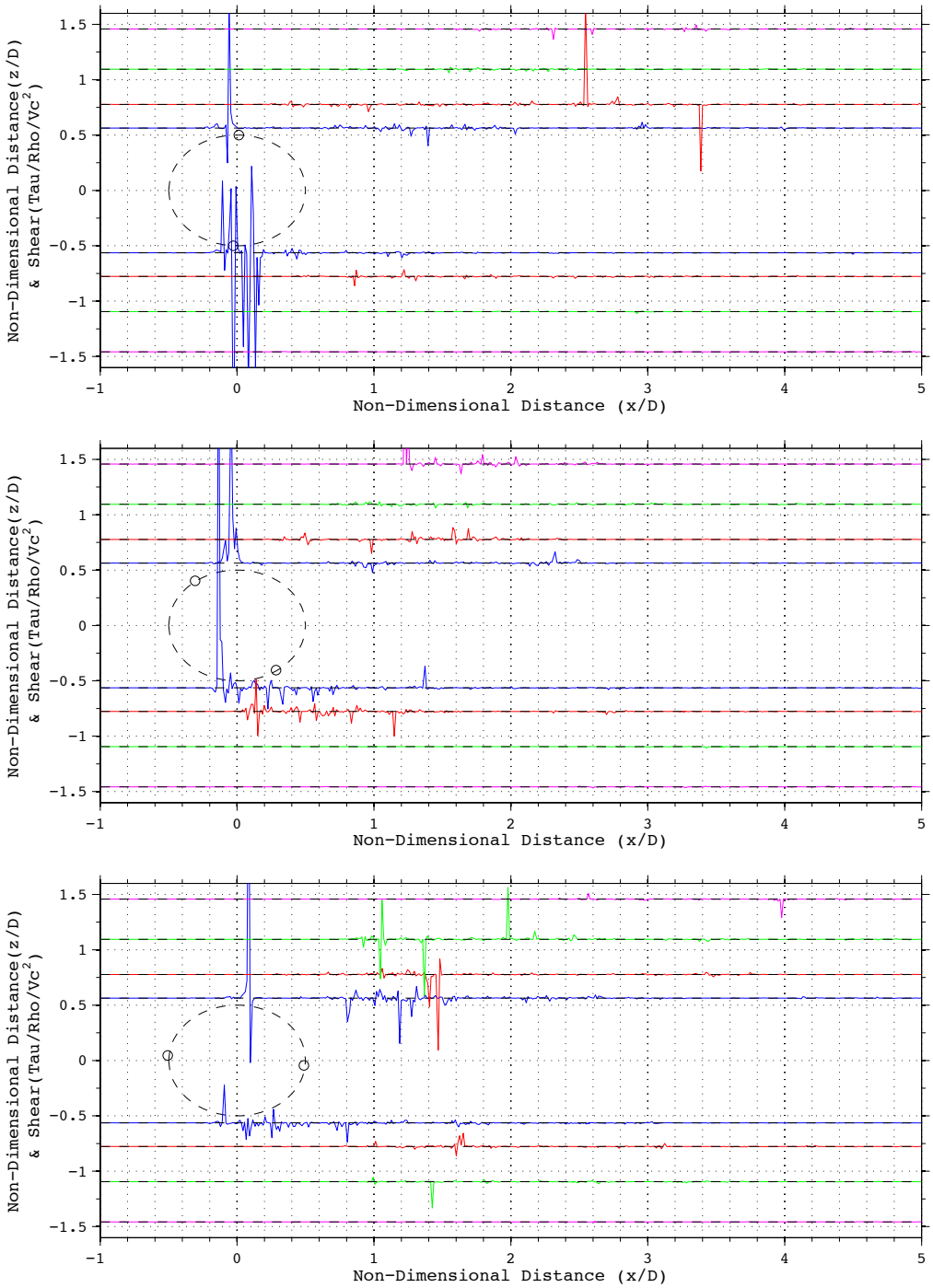

Figures 6.16 The three Reynolds shear terms for low solidity turbine over three blade positions. (a) Position 1 (b) Position 2 (c) Position 3

6.5 Surface Elevation

The surface elevation from the forward and reverse runs for the high solidity turbine displayed with the vector plot in Figure 6.19 show the relation ship of the flow field and the surface elevation. The changes in elevation are shown in non-dimensional units with respect to the turbine diameter, and the distance from the turbine centerline is proportional to the real measurement, however, in non-dimensional units of diameters.

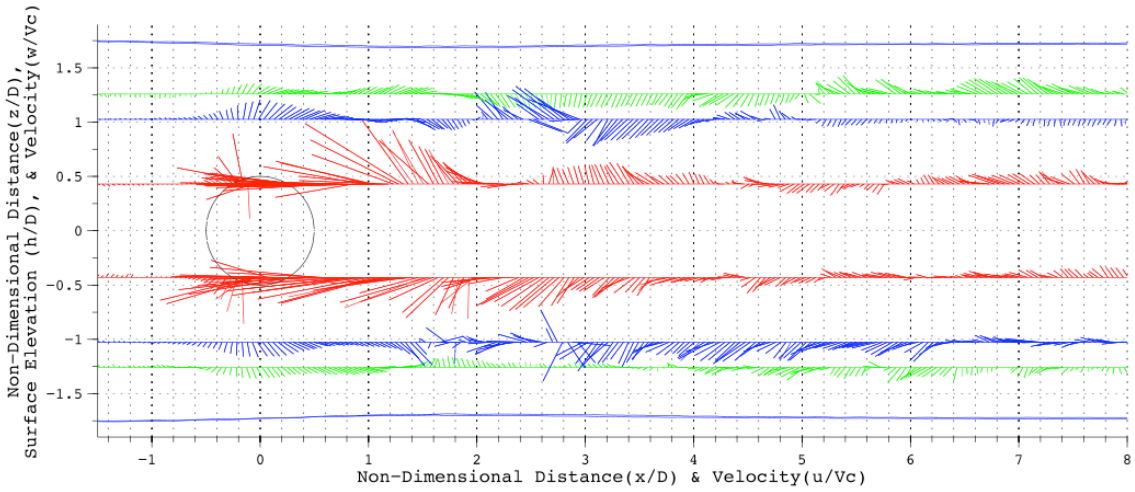

Figure 6.17 Vector plot with the upper and lower surface elevation for high solidity turbine.

Hydrodynamic testing in a semi-confined region with a large tank to turbine area ratio can amplify in the surface elevation as well as turbine performance. The effect is known as the blockage effect and has been discussed earlier in other papers, (Bahaja 2007, Whelan 2009). The amplified elevation change was observed by measuring a rise in surface elevation far up and down stream with the assumption that at large distances only the passing wave and the hydraulic pressure are present. The amplification of the elevation change was found in front of the turbine as well as behind the turbine with the larger drop downstream. The blockage effect is present in all tow tank and flume tests, particularly for devices with large drag and with large turbine to tank area ratio. A closer look at the surface elevation and blockage effect will be discussed in section 7.3.

7. DISCUSSION

The results from this study have shown four distinct stages in the flow field around a cross flow turbine. The stages are dependent on general viscous flow around any hydro-kinetics device in a uniform flow. Therefore, the stages will be present in either a lift dependent turbine or drag dependent turbine. However, the characteristics of each stage are strongly dependent on the type of turbine, solidity, TSR, and inflow velocity. The four stages are the up stream effects, the entrained flow behind the turbine, the connection between the entrainment to turbulence, and flow recovery. The stages are examined in this section as well as surface effects and the flipped reference frame of the tow tank.

7.1 Entrained Flow and Flow Recovery

One of the most important unanswered questions associated with marine hydrokinetics is the flow recovery behind the turbine. In this study the flow recovery is going to be analyzed using measurements of the mean velocity components, velocity magnitudes and velocity fluctuations for the different cross flow turbines. The high solidity case was analyzed first because of the uniform shape of the wake and simple flow patterns.

The recovery of the flow is divided into two regions of full and partial recovery. A partial recover is defined by flow within 80% of the initial velocity. A full recovery is more difficult to determine and is defined in this study as velocity within five percent of inflow velocity. The velocity magnitude for the high solidity turbine in Figure 7.1 demonstrates a partial recovery at ~3 diameters. The full recovery was measured at approximately 8 to 12 diameters downstream depending on the sample height for the high solidity turbine. A connection between the three velocity components was measured showing a phase relationship in accelerations. A rapid change in u-velocity is reflected by a large increase in w and v velocities. These changes are associated with the entrained flow seen in Figure 7.1 and 7.2 where the dominant velocity in the u-direction decays rapidly. A comparison of the velocity magnitude for the three components

shows conservation of energy until the occurrence of a spike in turbulence activity. The collapse of the entrained flow occurs at approximately 1.1 to 1.5 diameters. The flow recover is marked by a sudden increase in velocity fluctuation. The sudden increase in velocity fluctuation is seen as a second spike in TKE and Reynolds shear. The turbulent variables also show an abrupt end to the fluctuations as the large acceleration in the u-direction end. The second region of high velocity fluctuation appears to serve as a good indicator of transition between the entrained flow and a region of partial recovery.

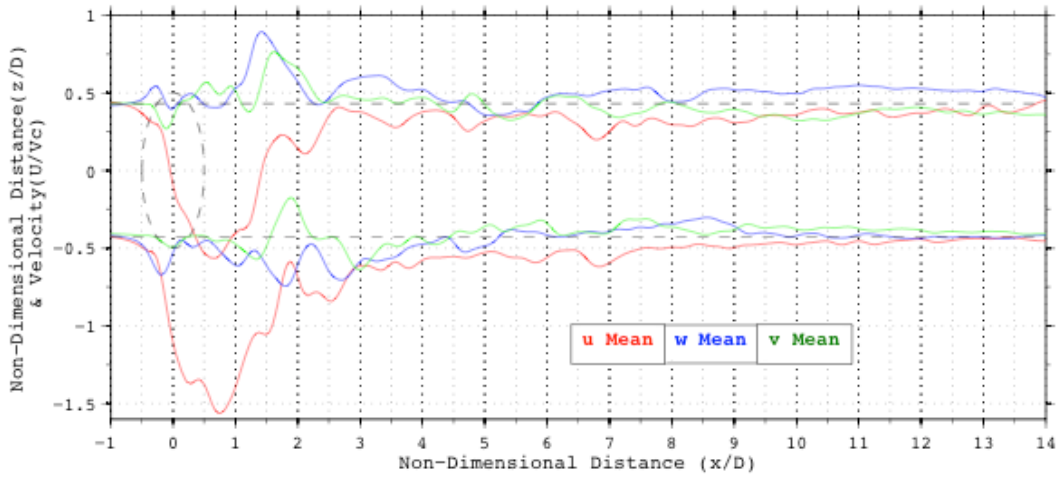

Figure 7.1 Mean velocity for each direction for high solidity turbine. The change momentum in x-direction shows equal change reflected into two orthogonal planes.

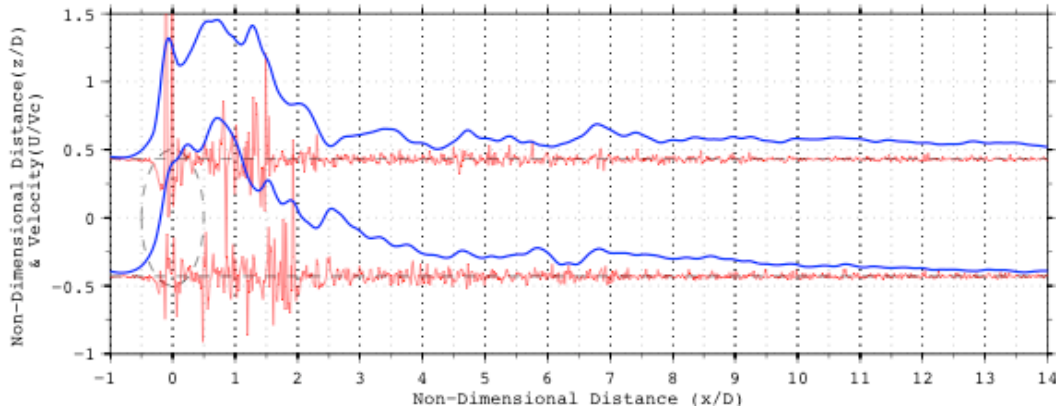

Figure 7.2 Mean velocity magnitude (red curves) and velocities fluctuation (blue curves) for high solidity turbine

The u-velocity fluctuations behavior down stream of the turbine show a consistent pattern through all acquired data. The velocity fluctuations have a brief period of high variability at

approximately zero distance followed by a sudden reduction seen in Figure 7.2. The decay rates of the two components are quite different: behind the turbine the fluctuations lasts only a short distance. In contrast to the slower decay of the mean component persists past ten diameters. The turbulent analysis shows the same trend measured for the high solidity turbine. A coupled behavior is thus demonstrated between flow recovery and turbulence. Where a connections between flow accelerations are associated with regions of high TKE and Reynolds shear are observed. Precise measurements of turbulent behavior are seen in the Reynolds shear and turbulence kinetic energy in Figure 6.13 and 6.15.

The entrained flow for the low solidity turbine appears uniform compared to the high solidity turbine. The u-mean velocity in Figure 7.3 shows that the entrained flow had different configuration through blade position as well as from ACL to BCL. Although the flow is unstable, the low solidity turbine entrained flow collapse can be determined from the data series using the turbulence variables. The second spike marks the vicinity of major velocity change as seen in the high solidity test. The full mean and turbulent variables are shown in Appendix A. For the low solidity turbine, the collapse occurs between 1.5 and 2.5 diameters downstream from the turbine, followed by the partial flow recovery between 2.5 and 10 diameters.

A relationship of the difference in flow recovery between the high and low solidity can be inferred from the measured blade forces. The flow variation of the low solidity turbine can be attributed to the oscillation of the blade forces because of the changing angle of attack. The forces for the low solidity case seen in Figure 3.8 show oscillations in all three degrees of freedom producing non-uniform flow. In comparison, the high solidity turbine has a more uniform wake and results in a less variable forces measured between the fluid and turbine demonstrating the relationship between the turbine and fluid has an effect on the overall flow field.

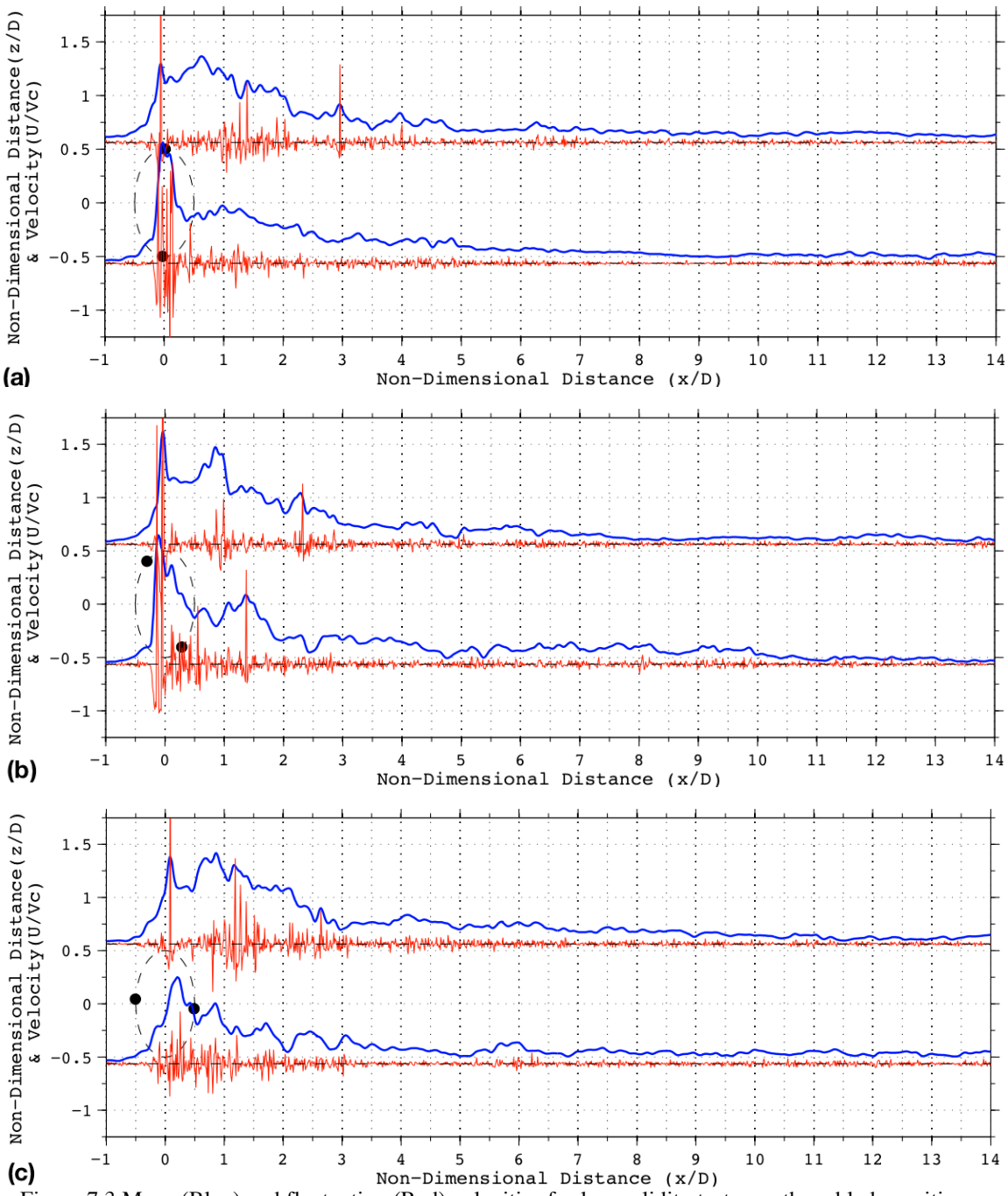

Figure 7.3 Mean (Blue) and fluctuation (Red) velocities for low solidity test over three blade positions

(a) Position 1 (b) Position 2 (c) Position 3

7.2. Upstream Effects

The approach of the turbine causes deceleration in the u-velocities while accelerating w-velocities away from the turbine. This upstream effect produces a flow around the turbine producing a bypass flow. The amount diverted from the turbine has significance relative to the environmental impact. The first environmental issue is that a turbine with high bypass will reduce the probability of fish strike. The amount of bypass flow determines the probability of wildlife will pass through or around forced around the swept area. Another environmental concern for developers is the effect of turbine scour on the seabed. Scour is a consequence of the turbine bypass flow increasing seafloor erosion. In addition to the impact on benthic ecology of the site scour can also compromise the turbine foundation.

Velocity measurements upstream of the turbine allow of the fraction of fluid forced away from the active area before the turbine arrives to be calculated. The bypass fraction is defined as the amount of flow diverted away from the turbine divided by the total flow. With no turbine, the ratio would be zero and a ratio of one if the turbine were solid. To convert the measurements into a non-dimensional bypass fraction the two volumetric flow rates are determined from the incoming flow (V_C) and measured vertical velocity (w) of the two inner sample heights. The distances between the two inner heights were included in the calculation as well as the distances between individual velocity sample volumes. The resulting quantity is the ratio representing the fraction of the fluid bypassing the turbine seen in Equation 12. Figure 7.3 depicts the physical principle.

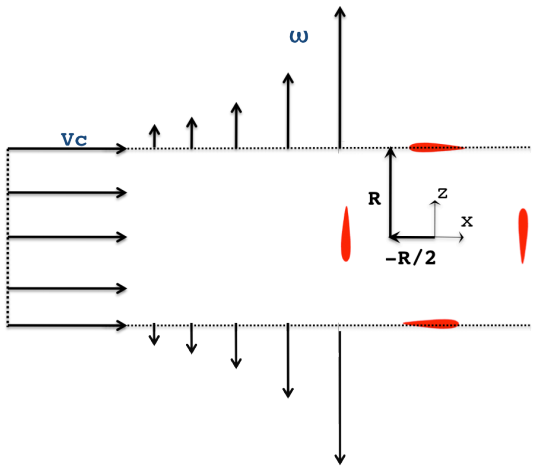

Figure 7.4 Visualization of the bypass flow and volumetric flow fraction

$$\dot{V}_{Bypass} = \int_{-\infty}^{-\frac{R}{2}} \omega \, dx$$

$$\dot{V}_{Ref} = \int_{-R}^{R} u \, dz = 2 \, R \, V_C$$

$$BPF = \frac{\dot{V}_{Bypass}}{\dot{V}_{Ref}} \tag{12}$$

Bypass faction for each side is presented and summed to obtain the total bypass fraction for both turbines. The bypass fraction results for the high solidity turbine are over three different TSR values are shown in Table 7.1. The results show a consistent increase of bypass with an increase in TSR. Due to the rotation of the turbine, both sides performed differently consistently showing a larger fraction ACL. For example, the topside for 0.9 and 1.4 TSR remained constant and the bottom side increases by an order of magnitude. If the turbine had no resistance to limit the rotational speed, then the turbine would free spin at the point near the zero performance at high TSR. The value for zero performance at a high TSR for the high solidity turbine is approximate 2.2 TSR. The bypass fraction for this point of operation was predicted using the assumption that the fraction is a function of the drag coefficient. The predicted bypass fraction for a free spin turbine is included in Table 7.1.

TSR	Bypass		
	Top	Bottom	**Total**
0.9	~0.033	~0.013	**~0.05**
1.4 (On Design)	~0.033	~0.10	**~0.13**
1.9	~0.223	~0.152	**~0.38**
2.2 (Free Spin)	*Predicted*		*~0.65 – 0.75*

Table 7.1 Flow Bypass for High Solidity for high solidity turbine over increasing TSR

The bypass fraction for low solidity turbine is shown in table 7.2 for each blade position. There is a measurable difference in bypass fraction for each blade position. A 20% shift on the mean was measured which clearly dominates the unsteady flow field for the low solidity wake. The mean bypass fraction is the average of the three positions and is remarkably similar to the high solidity turbine, with only 15% less bypass than the high solidity. In both cases, the bypass fractions are a relatively small portion of the overall volume.

TSR	Blade Position	Bypass Fraction		
		Top	Bottom	**Total**
2.25	**1**	~0.032	~0.052	**~0.08**
	2	~0.043	~0.091	**~0.13**
	3	~0.045	~0.068	**~0.11**
			Mean	**~0.11**

Table 7.2 Flow Bypass for Low Solidity for low solidity turbine

The two turbines of different solidity set to a TSR producing maximum performance divert approximately the same amount of fluid away from the active area. The two turbines have similar thrust coefficients (Table 3.6) when the two turbines were operating at optimal output. It thus can be concluded that the bypass factor is related to the drag coefficient even for the less conventional cross flow turbine.

Connection between the turbine forces and the flow field are present with the opportunity to simplify wake characterization. The two solidity turbines have solidity values of 0.16 and 0.32 and their measured drag coefficients are 0.30 and 0.32, respectfully. The bypass fraction only

changes slightly between the low and high solidity from 0.11 to 0.13 however the drag coefficient correlates well with the measured bypass fraction. This is further enforced by the measurements when TSR increases resulting in higher drag coefficients and the bypass flow.

7.3 Surface Elevation and Blockage Effect

An important factor to consider in hydrodynamic testing is that the turbine in the tow tank cannot be considered as an ideal infinite fluid. The ratio between the area of the turbine and the area of the tow tank is ~ 0.10 in the cross sectional y-z plane. The tank is relatively wide and shallow compared to the turbine, resulting in only 1.3 diameters of water above and below the turbine. The flow field is also influenced by the type of flow around the turbine. Flow in a restricted area can be ether supercritical or subcritical and is determined by the Froude number, Equation 13. The Froude-number is the ratio of the flow velocity over the speed of surface wave.

The behavior of the free surface depends on whether the approaching flow being subcritical or supercritical. A subcritical flow (Fr < 1) will cause the water level to decrease around an obstruction. Conversely, a supercritical flow (Fr > 1) will cause the water level to increase over a obstruction. For tow tank test the Fr number is below supercritical flow value. A depression in the water level over the turbine occurred as expected. The height from the top of the turbine to the water surface was 0.33m and the largest inflow speed of 1.0ms^{-1}. Supercritical flow will only occurs if the speed is increased to 1.8ms^{-1} with the same depth or the depth is reduced to 0.1m.

$$\mathrm{Fr} = \frac{V_C}{\sqrt{g\,h}} = 0.55 \tag{13}$$

However, depending on the test configuration a buildup of a hydraulic head can occur. The higher solidity turbine is more likely to produce a hydraulic head due to its higher number of blades and the low variability in turbine forces. The blockage effect was previously introduced in section 6.5. The tests in this study were performed at a relatively high TSR and carriage speed producing a measurable hydraulic head only for the high solidity turbine. The blockage effect

appeared in the surface data for the high solidity turbine as an elevated surface as soon as the carriage started to accelerate from rest. The blockage effect is also present down steam from the turbine where the effect is negative change in elevation. As the turbine neared the end of the tow tank, the elevation begins to recover due to the reduced tank volume ahead of the turbine. Due to the reduced blade area of the low solidity turbine the blockage effect is much smaller and is considered negligible.

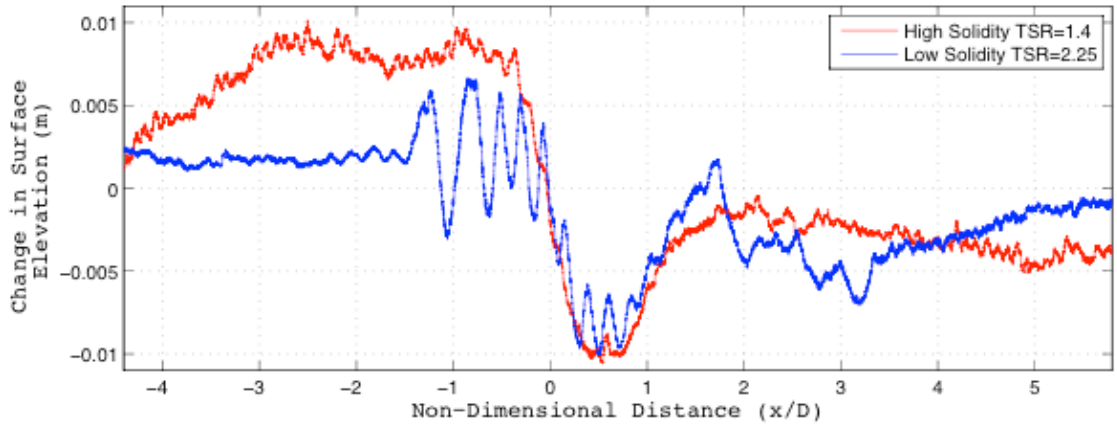

Figure 7.5 Change in surface elevations for two different solidities. Tests were done with the constant carriage speed at 0.8ms^{-1} for the high and low solidity at optimum TSR.

The surface effects from the low solidity turbine show a different response with a region dominated by gravity waves near the turbine. The fewer number of blades for the low solidity turbine allowed individual blade effects to be measured in the surface elevation. The waves occur 1.5 diameters in front and 1 diameter behind the turbine. The increase elevation at 1 to 1.5 diameters in Figure 7.5 is associated with the second hydraulic jump to return to the water level to equilibrium. The waves also occur at the same rate as the blade frequency. A Fourier transform on the surface elevation measurements (Figure 7.6) confirmed the blade frequency was equal to the surface wave frequency. Thus, the surface elevations differ according to TSR showing individual blade effects on the surface.

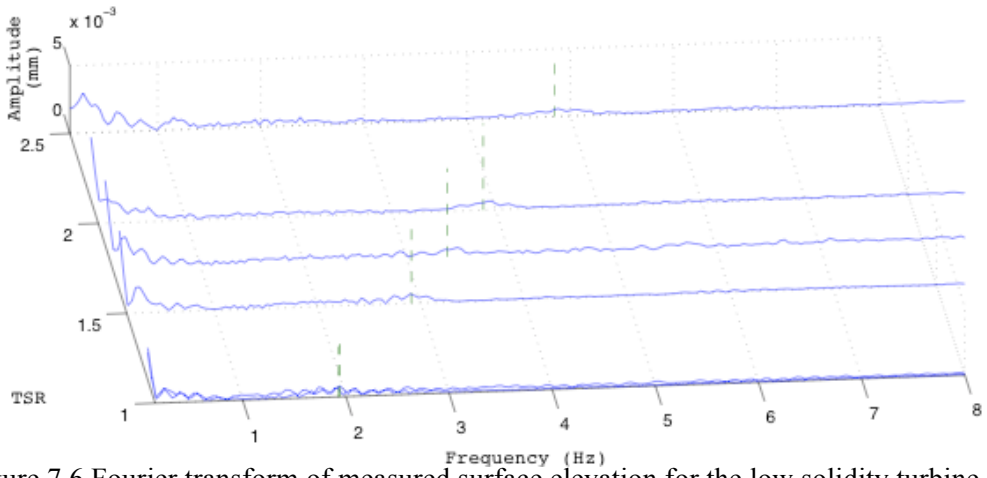

Figure 7.6 Fourier transform of measured surface elevation for the low solidity turbine over different TSR values. The blade frequency is marked by green dash line.

Surface elevation measurements were also collected for different TSR using the high solidity turbine. Three different TSR were used 0.9, 1.4, and 1.9. A 1.4 TSR yielded the maximum performance. The increase in TSR causes an increase in the drag coefficient affecting the hydraulic jump of the turbine. In Figure 7.7 and 7.8 the measurements of surface elevation three TSR are shown with the carriage traveling in opposite directions in the two figures. These measurements show the difference in the hydraulic jump as the TSR changes. As a result, a larger pressure drop occurs across the turbine, which is seen in the hydraulic jump.

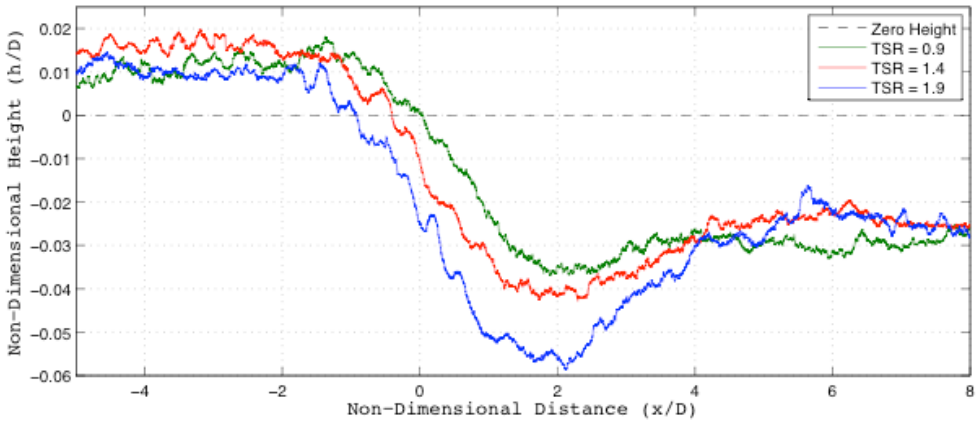

Figure 7.7 Surface elevation for high solidity test with three different TSR for power side on top

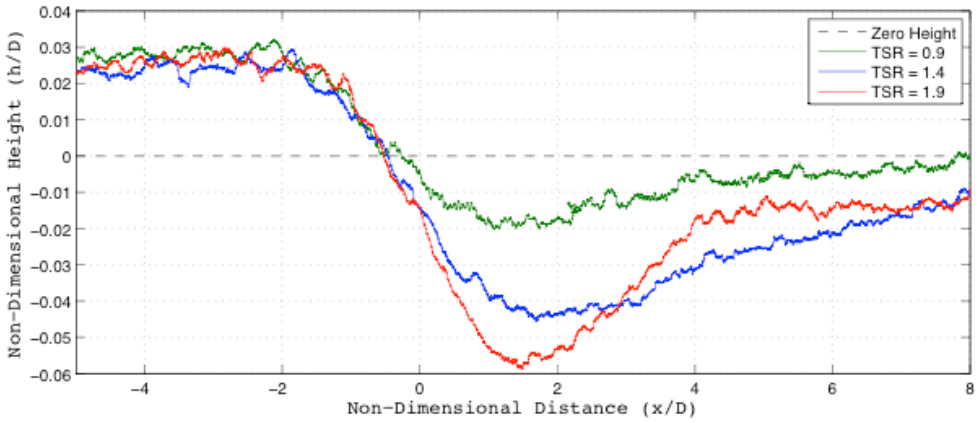

Figure 7.8 Surface elevation for high solidity test with three different TSR for return side on top

7.4. Flipped Reference Frame

In addition to the direction and blockage another effect is evident in the testing. A fundamental principle of a tow tanks the turbine move through a fluid at rest. For test of a turbine in a tow tank the result is a flipped reference frame. The fluid is at rest while work is done to move the turbine through the fluid. The flipped reference frame creates a discrepancy between the velocities in the wake and in the surrounding fluid. For a stationary turbine the flow decelerates relative to the surrounding unaffected flow, resulting in a pressure gradient which forces the wake to expand. The expansion of the wake is described by Bitz's momentum theory. In the Bitz theory a simplified analysis can predict the cross sectional area of the wake seen in the

flow diagram in Figure 7.6. However, the theory assumes steady inviscid laminar flow. The theory also ignores the blade section lifts and drag forces associated with wing theory. If the momentum theory is compared to the tow tank reference frame, differences appear both in wake and in the surrounding fluid. In contrast to the actual turbine, in the tow tank the flow is accelerated and moves with the turbine. The surrounding fluid is at rest and the result is that a pressure gradient develops in the opposite direction if Bernoulli's principle is considered.

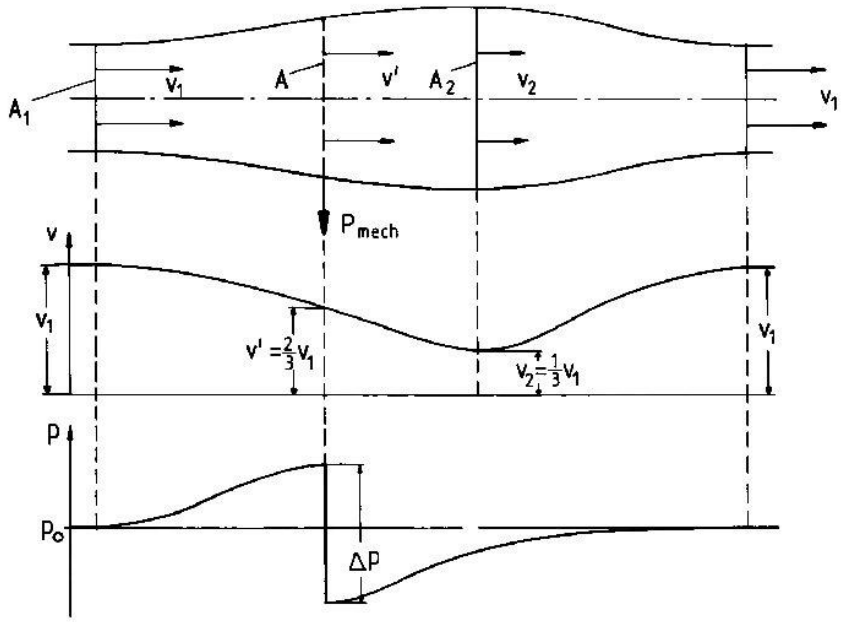

Figure 7.9 Actuator Disk principle from the Bitz momentum theory (Hau, E., 2006)

The validity of Bernoulli's principle to the understanding of the wake is dependent on the introduction of unsteady viscous turbulent flow. A derivation of Reynolds stress shows that the three turbulent components that cause momentum transfer across a boundary introduce an unsteady time-dependent term. Because of time-dependent term the turbulent momentum transfer dominates. Therefore, the tow tank may in fact be useful for wake measurements. Since turbulence is primarily responsible for the wake in both the actual application and the tow tank tests. The flipped reference frame is not a concern.

8. CONCLUSION

This study extends previous work on the flow recovery of marine hydrokinetic devices to cross flow turbines. This experimental work was performed using a reduced scaled cross-flow turbine to analyze the wake changes as the blade rotates for different blade solidities, tip speed ratios and blade mounting angles.

The results show four distinct regions of the flow field around a cross flow turbine. These regions are dependent on the general viscous flow around any hydro-kinetic device in a uniform flow. These flow in these regions are to be strongly dependent on the solidity, TSR, and inflow velocity of the cross-flow turbine. Since the regions are dependent on the turbine configuration, they may be an important factor to consider with regards to turbine designs and installations. In particular, the measurements of the location where the flow is fully recovered are particularly useful for turbine array design.

Major factors such as the bypass flow are also import characteristics to identify. The bypass flow for the low solidity and high solidity cases was measured since it is an important factor for calculating the probability of the turbines striking marine fauna. Results of the bypass flow in the terms of Reynolds shear and TKE are presented for consideration of future studies of bottom scour. Finally, the entrained flow is analyzed to provide information for future work on the impacts on marine fauna and on the sediment transport for the low and high velocity regions.

Overall, what has been demonstrated is the ability to characterize some of the most important features of the flow field around and behind a cross flow turbine. While this type of study is intended for provide information for turbine array design, the information presented is also a useful tool to understand the impact that a cross flow turbine will have on marine fauna. This study can also help to provide the basis for a statistical analysis to define the flow field regions around a cross-flow turbine.

REFERENCES

Bahaja, A. S., & Mollandb, A. F., Chaplin, J. R., Batten, W. M. (2007*). Power and thrust measurements of marine current turbines under various hydrodynamic flow conditions in a cavitation tunnel and a towing tank*. *Renewable energy*. 32, 407-426

Blanckaert, R. H., & Lemmin, U. (2006). Means of noise reduction in acoustic turbulence measurements. *Journal of Hydraulic Research*, *44*, 3-18.

Charlier, R. H. (2006). *Tidal energy*. New York: Van Nostrand Reinhold Company.

Dabiri, J. (2010). *Order-of-magnitude enhancement of wind farm power density via counter-rotating vertical-axis wind turbine arrays*. Informally published manuscript, Graduate Aeronautical Laboratories & Bioengineering, California Institute of Technology, Pasadena, CA.

deBree, G. S. (2012). *Testing and Modeling of High Solidity Cross-Flow Tidal Turbines.* Master's Thesis, University of Maine, Orono, ME.

Goring1 D., Nikora V. (2002). Desdepiking acoustic doppler velocimeter data. *Journal of Hydraulic Engineering*, 117-126.

Hau, E. (2006). *Wind turbines: Fundamentals, technologies, application, economics*. Berlin: Springer.

Harris, F. J. (1978). On the use of windows for harmonic analysis with the discrete fourier transform. *IEEE*, *66*(1), 51-83.

Li, L., Xu, C., & Zhang, Z. (1999). Measurement of mean burst period in wall turbulence by wavelet analysis. *Communications in Nonlinear Science & Numerical Simulation*, *4*(3), 200-206.

Lohrmann A., Cabrera R., Kraus N.C. (1994). Acoustic Doppler velocimeter (ADV) for laboratory use. *Proceedings of the Symposium on Fundamentals and Advancements in Hydraulic Measurements and Experimentation*. 351–365.

Lokocz, T., 2010, "Solid Mechanics of Cross Flow Tidal Turbine Blades," University of Maine.

Myers L., Bahaj A. (2009, March). Experimental analysis of the flow field around horizontal axis tidal turbines by use of scale mesh disk rotor simulators. *Ocean Engineering*, 219-227.

Polagye B., Cleve B.V., Copping A., Kirkendall K. (2011). Environmental Effects of Tidal Energy. U.S. Department of Commerce National Oceanic and Atmospheric Administration National Marine Fisheries Service

Rinoshika A., Zhou Y. (2007). Effects of initial conditions on wavelet-decomposed structures in a turbulent far-wake. *International Journal of Heat and Fluid Flow*, 948–962

Rusello, P.J., Lohrmann, A., Siegel, E., Maddux, T. (2006). Improvements in acoustic doppler velocimetry. *Proceedings of the Seventh International Conference on Hydroscience and Engineering*, Sept.

Shiono, M., Suzuki, K., and Kiho, S. (2000). An Experimental Study of the Characteristics of a Darrieus Turbine for Tidal Power Generation, *Electrical Engineering in Japan*. 132(3) 38-47

Thorpe, S., (2007). *An Introduction to Ocean Turbulence*. Cambridge MA: Cambridge Press.

Tropea C., Yarin A. L., Foss J.F., (Eds.), (2007) *Springer Handbook Experimental Fluid Mechanics,* Berlin Heidelberg: Springer-Verlag

Urbina, R., Peterson, M.L., Kimball, R.W., DeBree, G.S., and Cameron, M.P., (2011), Modeling and Validation of a Cross Flow Turbine Using Free Vortex Model and a Modified Dynamic Stall Model, Submitted to: *Renewable Energy.*

Voulgaris G., Trowbridge H., (1997). Evaluation of the Acoustic Doppler Velocimeter (ADV) for Turbulence Measurements. *Journal of Atmospheric and Oceanic Technology*. 272-289

Whelan J. I., Graham J. M. R., Peiro J. (2009) A free-surface and blockage correction for tidal turbines. Journal of Fluid Mechanics. 624, 281–291

APPENDICES

Appendix A: Reynolds Decomposition

Complete set of Reynolds decomposition for all tested turbine arrangements. The low solidity turbine Reynolds decomposition is shown in Figure B.1 through B.3 for the three blade positions. Figure B.4 through B.6 show the components for the high solidity turbine.

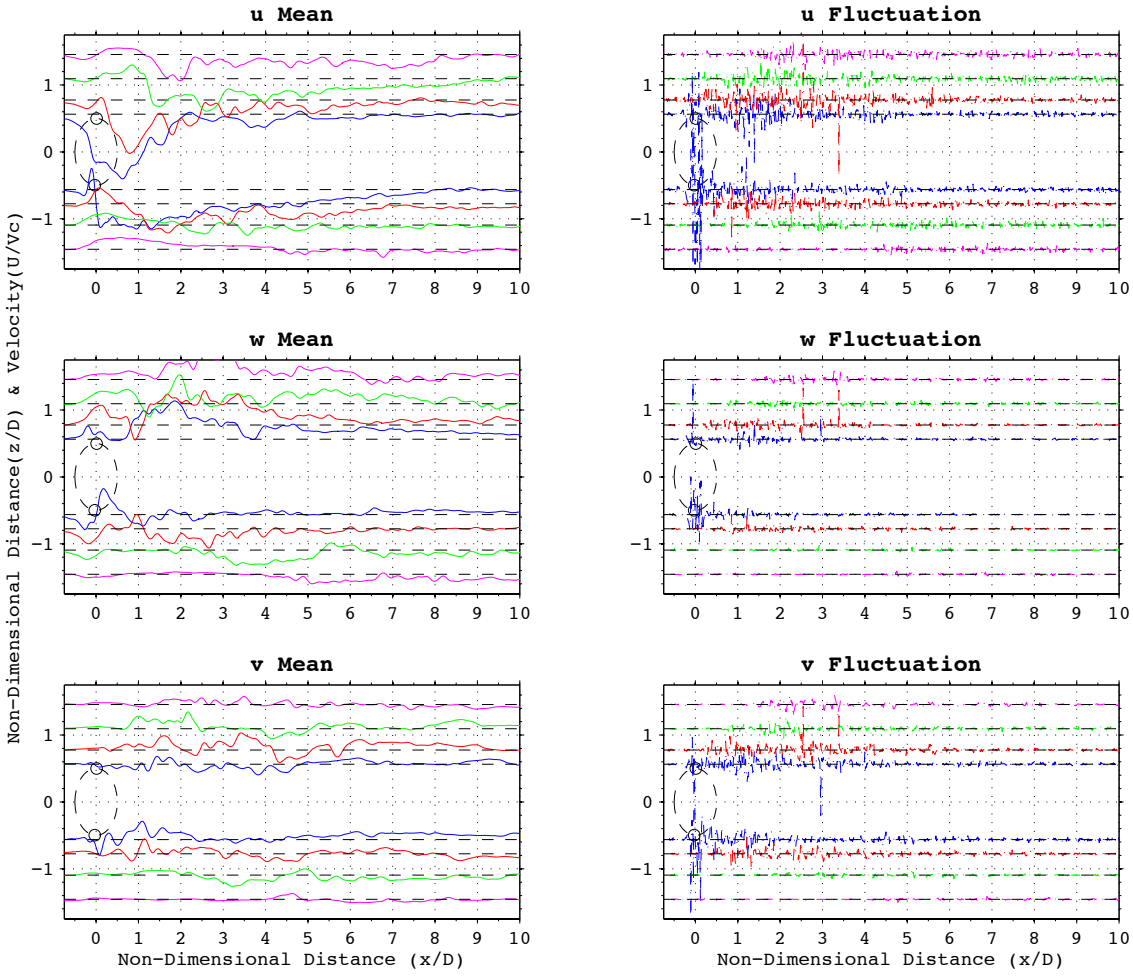

Figure A.1 Reynolds decomposition for each velocity component for low solidity at blade position 1

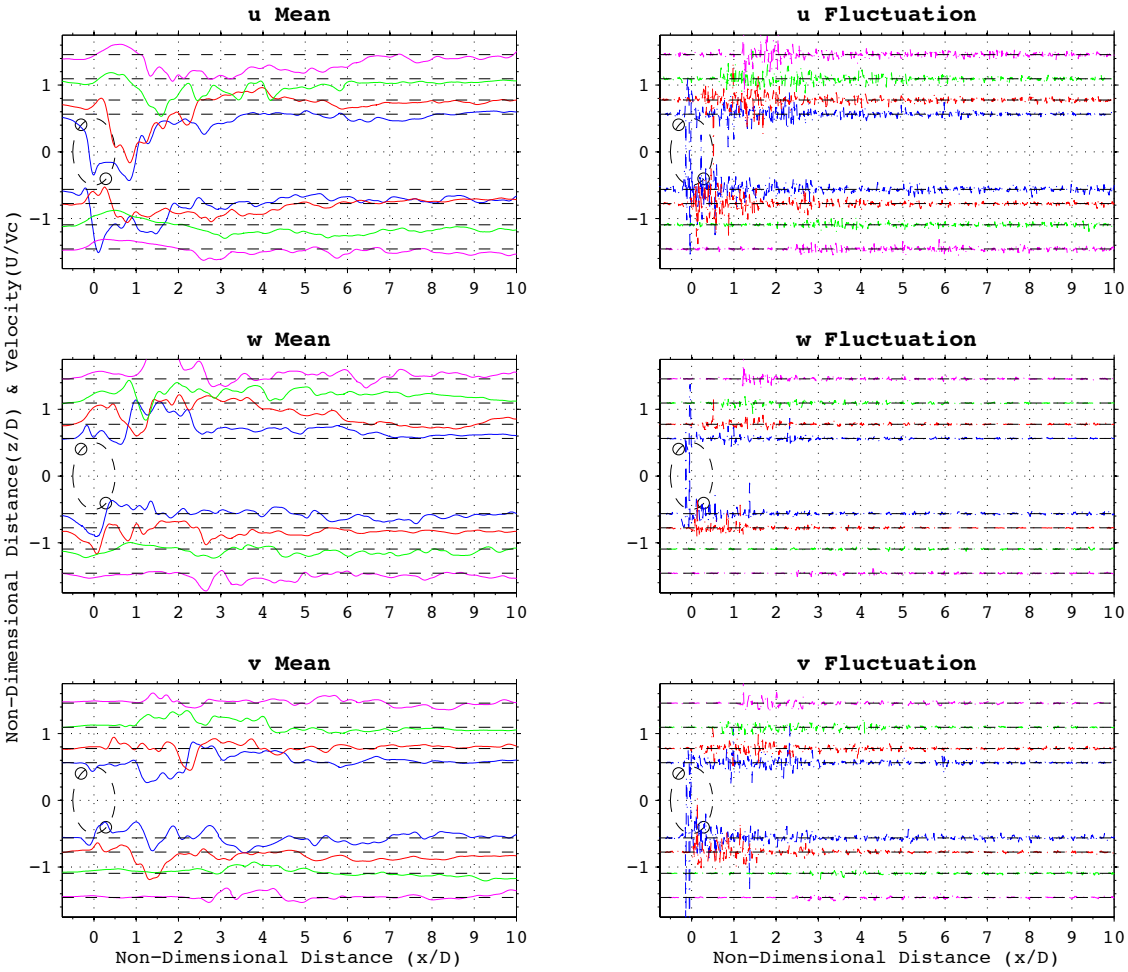

Figure A.2 Reynolds decomposition for each velocity component for low solidity at blade position 2

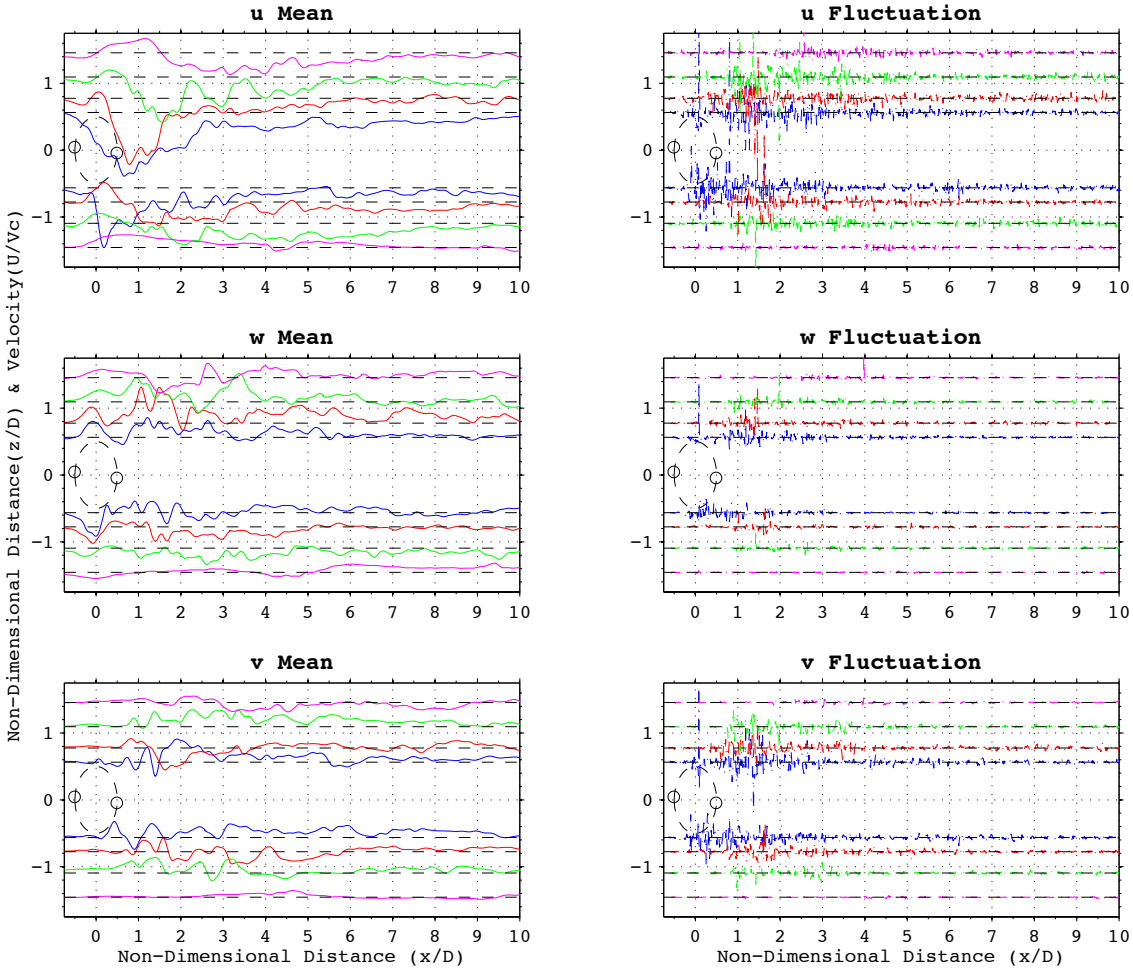

Figure A.3 Reynolds decomposition for each velocity component for low solidity at blade position 3

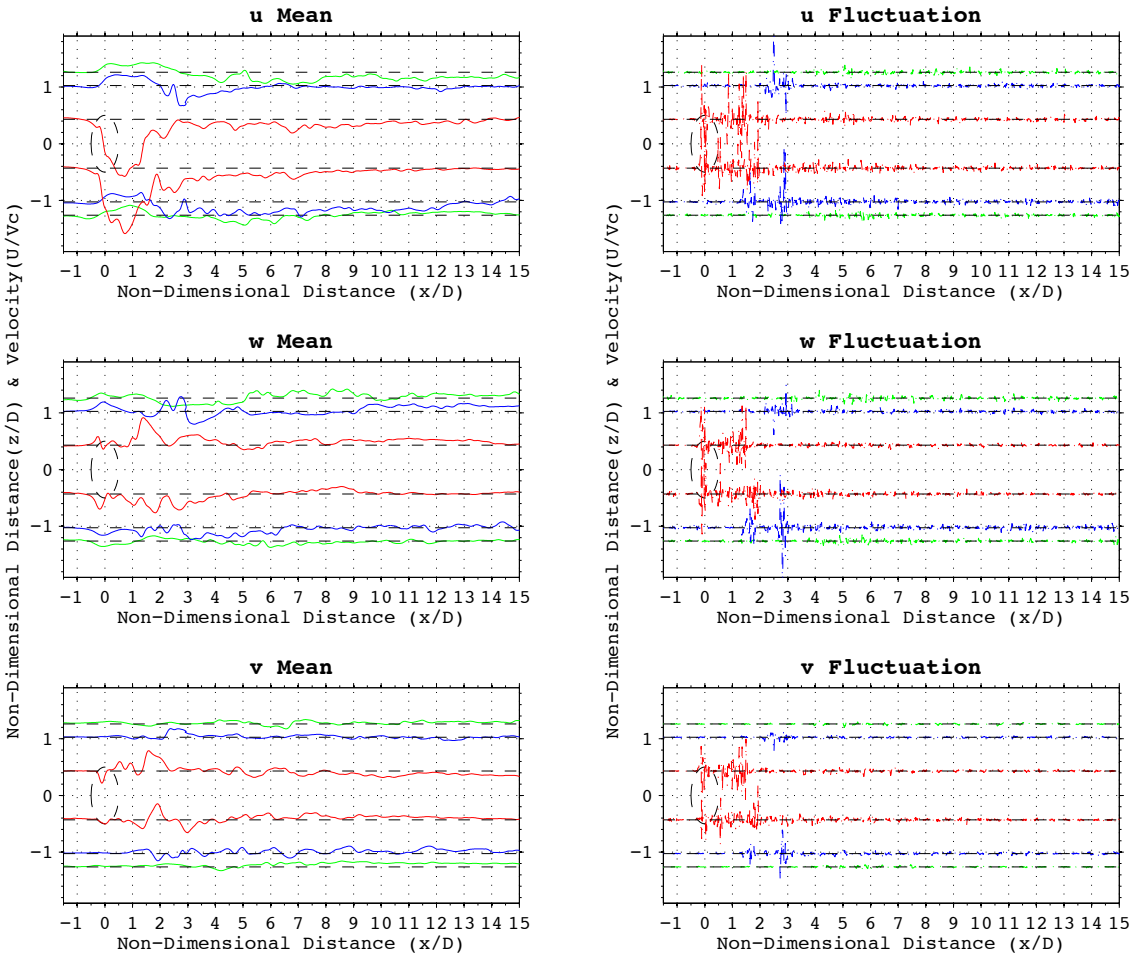

Figure A.4 Reynolds decomposition for each velocity component for high solidity at 1.4 TSR

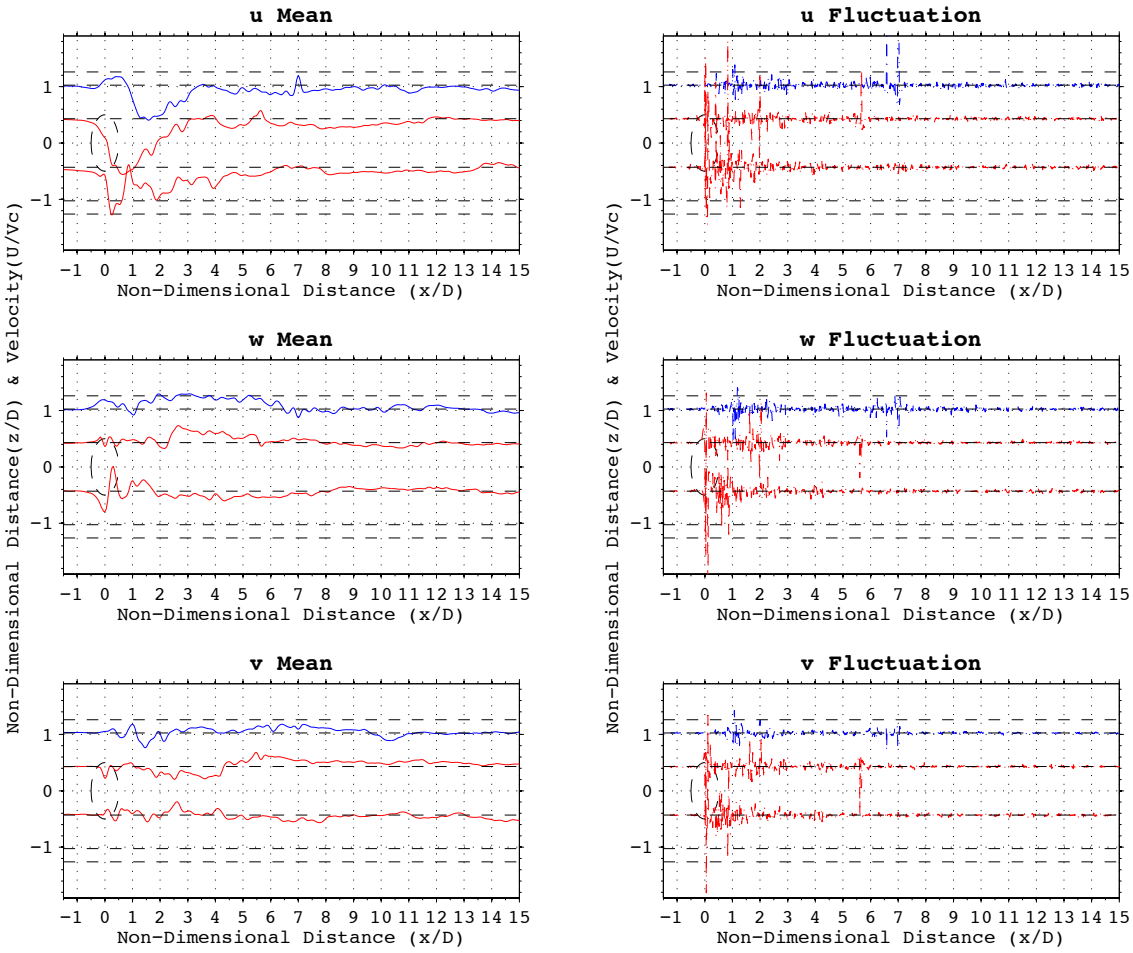

Figure A.5 Reynolds decomposition for each velocity component for high solidity at 0.9 TSR

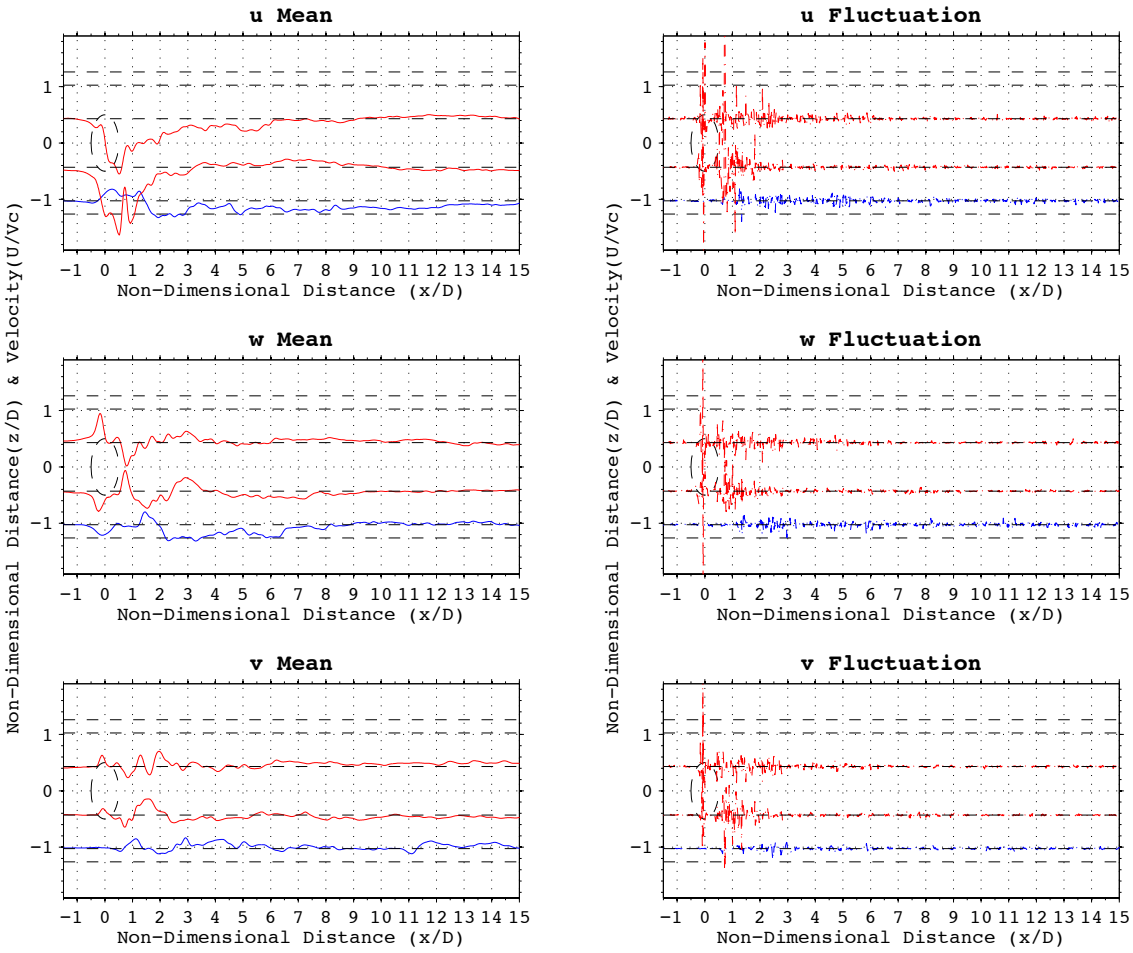

Figure A.6 Reynolds decomposition for each velocity component for high solidity at 1.9 TSR

Appendix B: High Solidity Wake Characteristics at different TSR

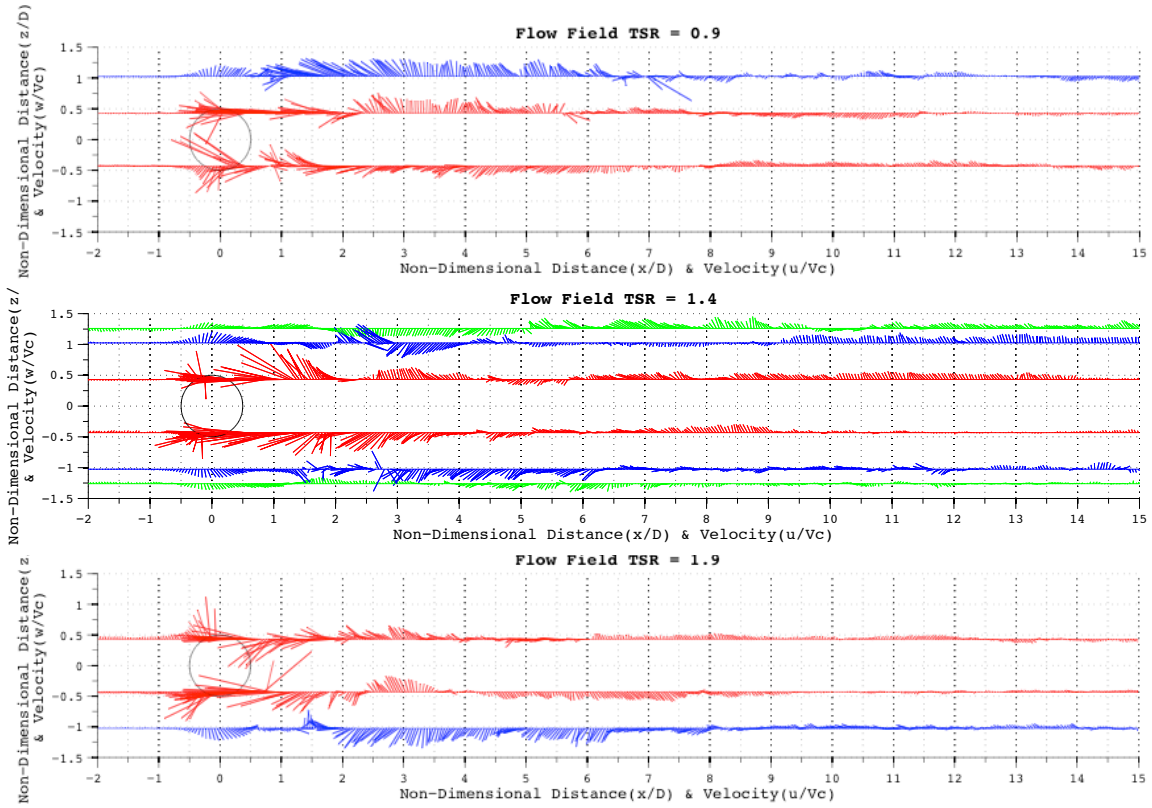

Figure B.1 Flow Field for high solidity turbine operating at different TSR..
0.9 TSR Top, 1.4 TSR middle, and 1.9 TSR bottom

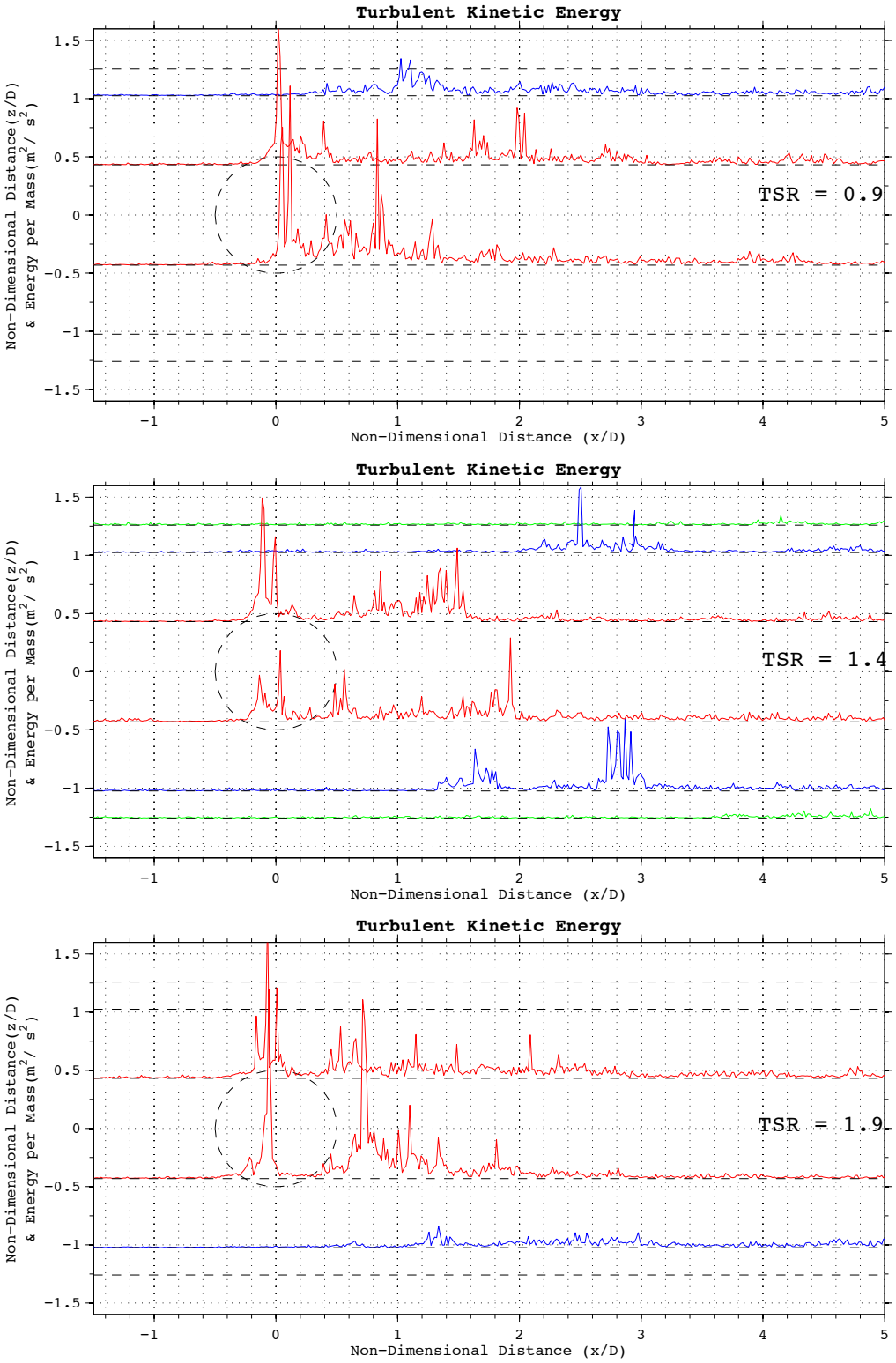

Figure B.2 Turbulent kinetic energy for high solidity turbine operating at different TSR. 0.9 TSR Top, 1.4 TSR middle, and 1.9 (Bottom) TSR

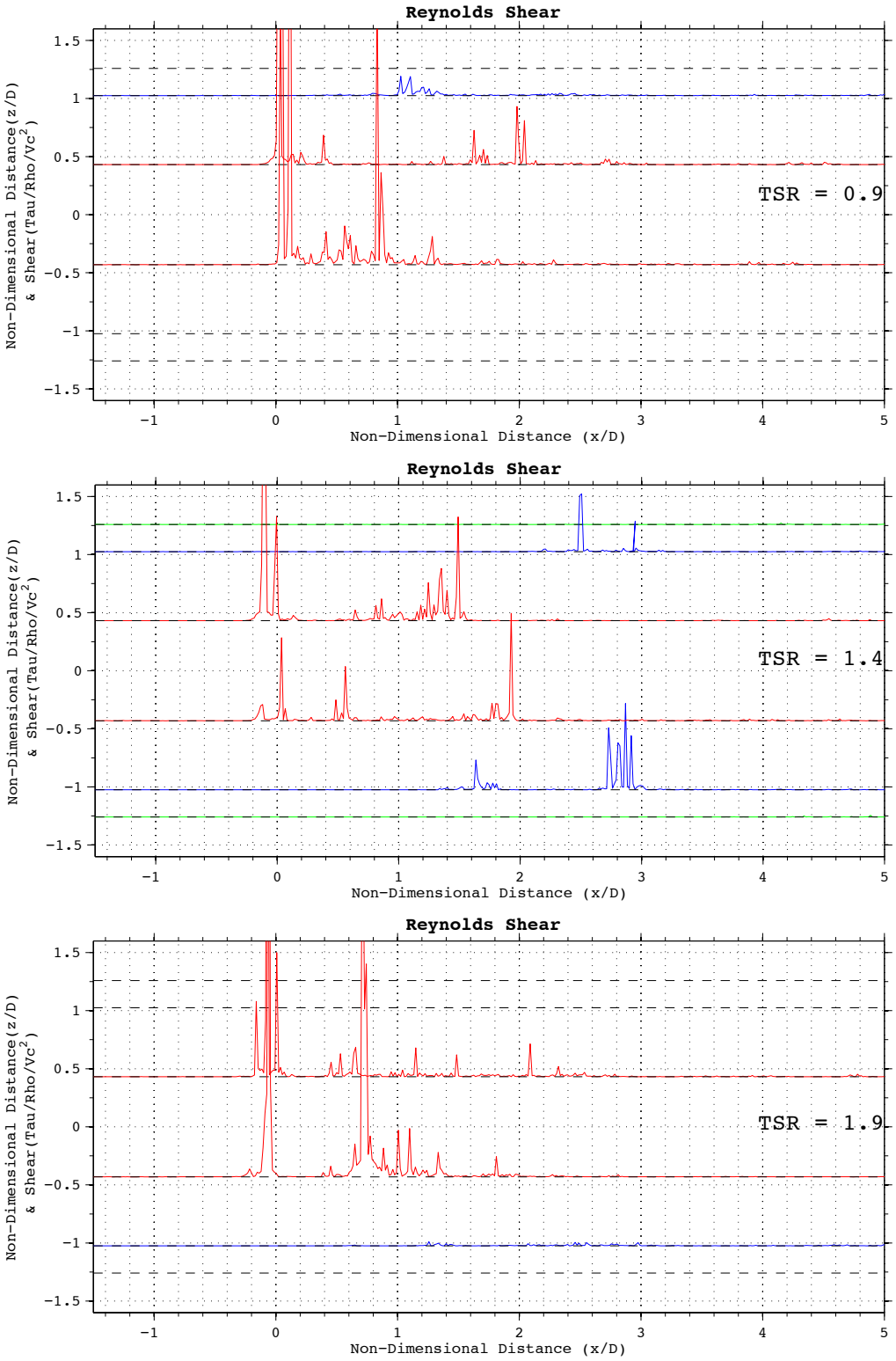

Figure B.3 Reynolds shear for high solidity turbine operating at different TSR. 0.9 TSR Top, 1.4 TSR middle, and 1.9 (Bottom) TSR

Appendix C: Low Solidity Turbine Wake Characteristics

Full velocity results for low solidity turbine for different blade positions. The results shown below are velocity magnitude and the three velocity components.

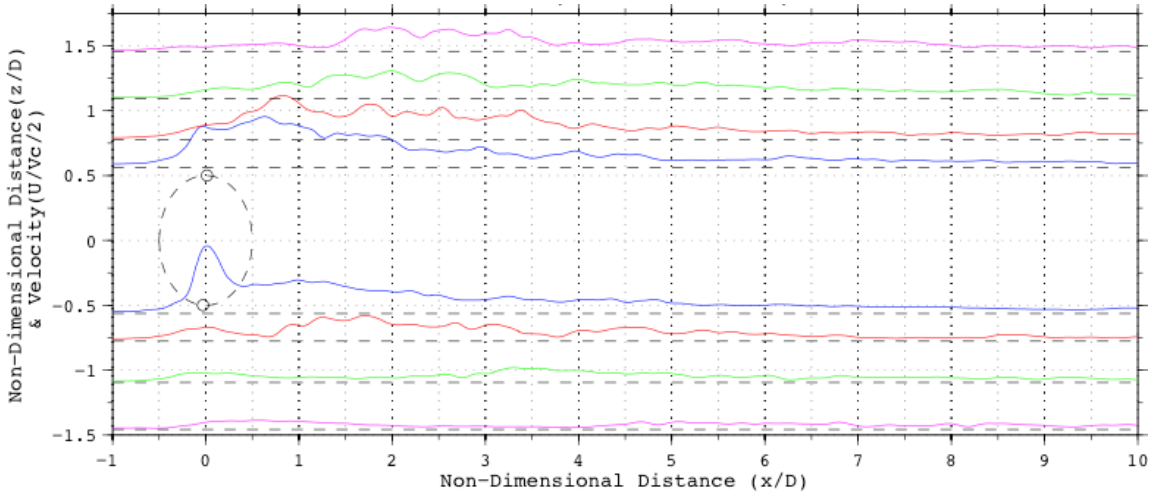

Figure C.1 Velocity magnitude for blade position 1

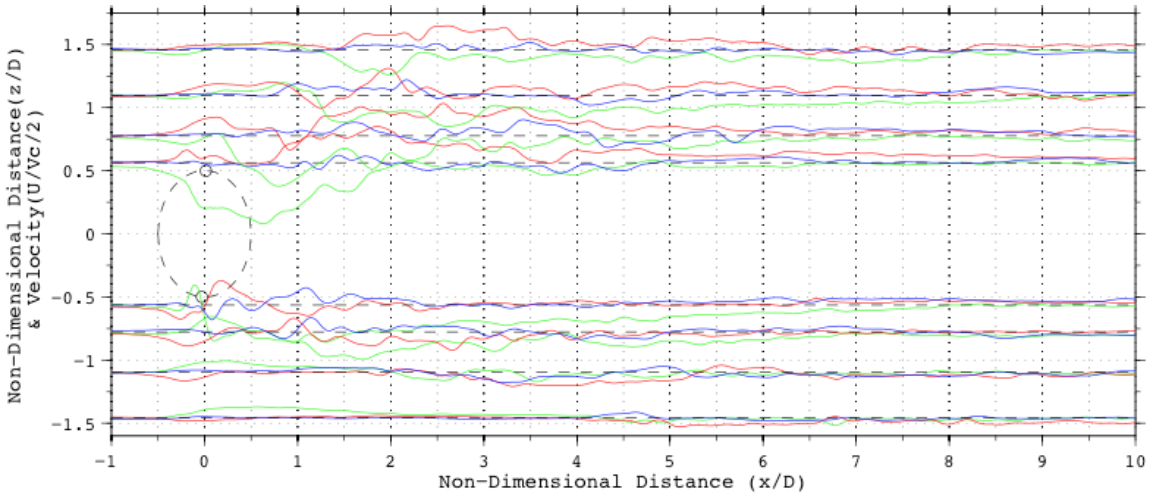

Figure C.2 Velocity components for blade position 1

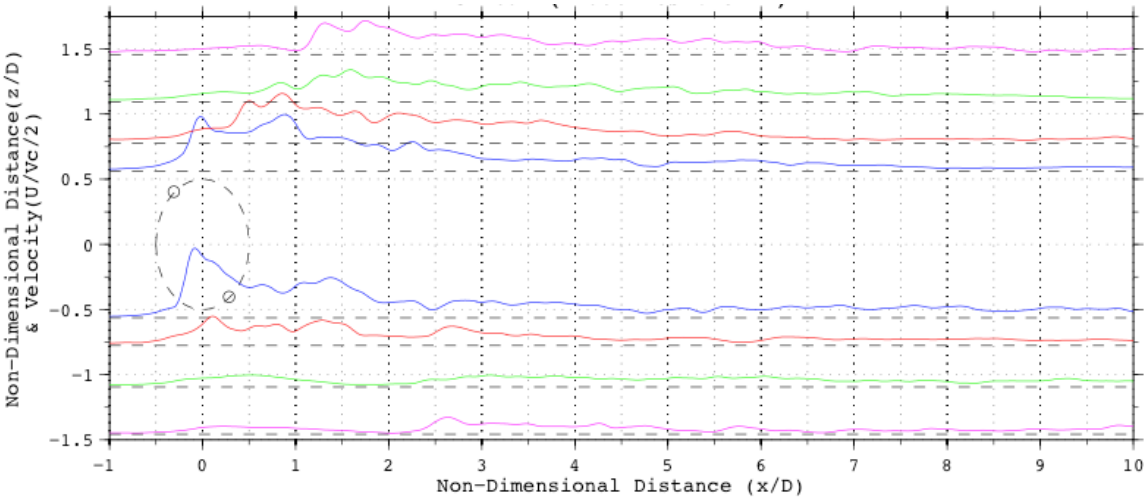

Figure C.3 Velocity magnitude for blade position 2

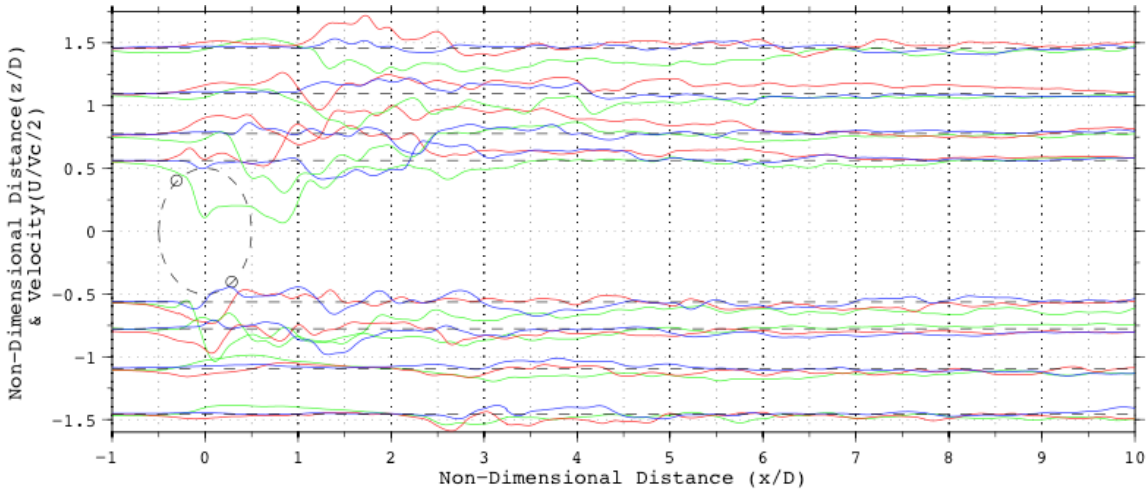

Figure C.4 Velocity components for blade position 2

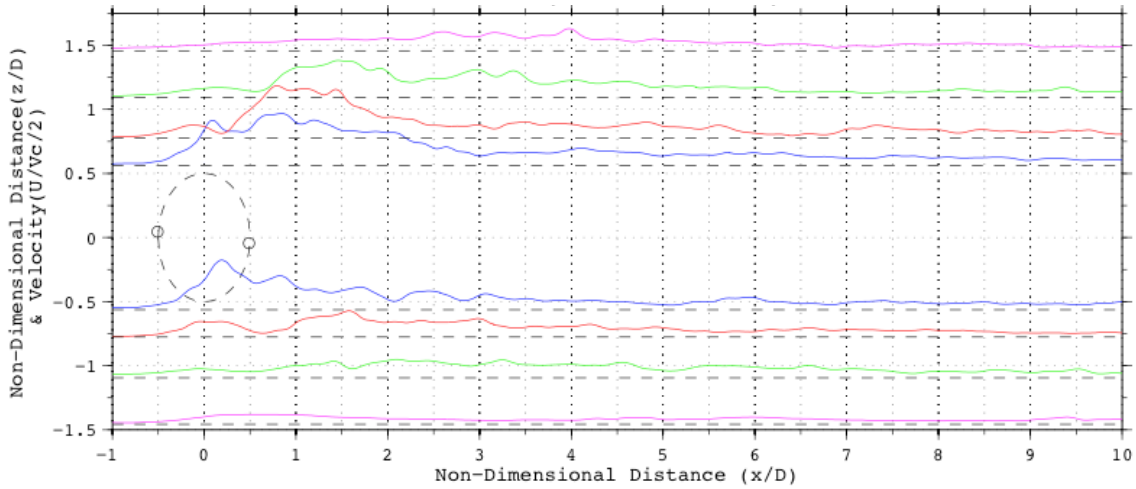

Figure C.5 Velocity magnitude for blade position 3

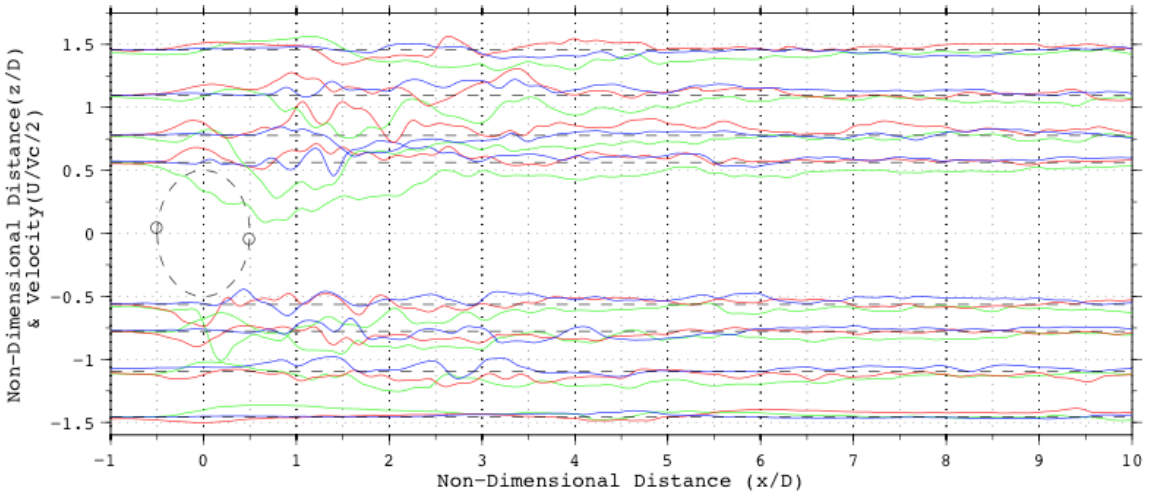

Figure C.6 Velocity components for blade position 3

BIOGRAPHY OF THE AUTHOR

Matthew Cameron attended the University of Maine, Orono, as an undergraduate from 2005 to 2009, whereupon he graduated with a Bachelor's degree in Mechanical Engineering. He decided to further his education and entered the Mechanical Engineering graduate program at The University of Maine in the fall of 2010. After receiving his degree, Matthew intends to pursue a career of invention and innovation. Matthew is a candidate for the Master of Science degree in Mechanical Engineering from The University of Maine in August, 2012.